VTRC
Virginia Transportation
Research Council

We Bring Innovation to Transportation

The Effects of Surface Condition and Long-Term Environmental Exposure on the Bond Between CFRP and Steel

https://vtrc.virginia.gov/media/vtrc/vtrc-pdf/vtrc-pdf/27-R04.pdf

ABRIL YU-SHAN, Ph.D., Engineer
Thornton Tomasetti

BERNARD L. KASSNER, Ph.D., P.E., Research Scientist
Virginia Transportation Research Council

AUDREY MORUZA, Senior Research Scientist
Virginia Transportation Research Council

MATTHEW HEBDON, Ph.D., P.E., Associate Professor
Department of Civil, Architectural and Environmental Engineering
The University of Texas at Austin

MARYAM SHAKIBA, Ph.D., Assistant Professor
Ann and H.J. Smead Aerospace Engineering Sciences
University of Colorado Boulder

BERNARDO CARRERA, Associate Project Consultant
Simpson Gumpertz & Heger

PREET JIWANI, Graduate Engineer
Walter P Moore

Final Report VTRC 27-R04

VIRGINIA TRANSPORTATION RESEARCH COUNCIL
530 Edgemont Road, Charlottesville, VA 22903-2454
vtrc.virginia.gov

Standard Title Page - Report on Federally Funded Project

1. Report No.: FHWA/VTRC 27-R04	2. Government Accession No.:	3. Recipient's Catalog No.:
4. Title and Subtitle: The Effects of Surface Condition and Long-Term Environmental Exposure on the Bond Between CFRP and Steel		5. Report Date: August 2026 6. Performing Organization Code:
7. Author(s): Abril Yu-Shan, Ph.D.; Bernard L. Kassner, Ph.D., P.E.; Audrey Moruza; Matthew Hebdon, Ph.D., P.E.; Maryam Shakiba, Ph.D.; Bernardo Carrera; and Preet Jiwani		8. Performing Organization Report No.: VTRC 27-R04
9. Performing Organization and Address: Virginia Transportation Research Council 530 Edgemont Road Charlottesville, VA 22903		10. Work Unit No. (TRAIS): 11. Contract or Grant No.: 115768
12. Sponsoring Agencies' Name and Address: Virginia Department of Transportation 1221 E. Broad Street Richmond, VA 23219	Federal Highway Administration 400 North 8th Street, Room 750 Richmond, VA 23219-4825	13. Type of Report and Period Covered: Final 14. Sponsoring Agency Code:
15. Supplementary Notes: This is an SPR-B report.		

16. Abstract:

As the existing steel infrastructure inevitably continues to age and deteriorate, engineers are increasingly looking for innovative and effective methods for repairing and maintaining existing steel bridges, which are susceptible to corrosion damage when exposed to aggressive environments and deicing salts. Conventional methods for repairing steel bridges can be labor intensive and time consuming and add considerable weight to the existing structure. One alternative is to utilize carbon fiber reinforced polymers (CFRPs). Many studies have documented CFRP's ability to enhance the strength of existing structures while having a high strength-to-weight ratio and the added benefit of being noncorrosive. However, most of these studies have focused on the bond behavior between CFRP and steels having a smooth surface condition, which is not representative of deteriorated structures in need of retrofitting. Further research has examined the durability of CFRP-steel bonds but under conditions that do not reflect the service life conditions for typical bridge applications.

This study examined the effects of the surface condition and environmental exposure on the bond between steel and two different CFRP materials, one having a normal modulus and the other an ultra-high modulus. The researchers evaluated the influence of corrosion and simulated corrosion pitting to determine whether structures with non-uniform surfaces are viable candidates for CFRP retrofits. In addition, the durability of CFRP-steel bonded, double-strap jointed specimens was investigated through laboratory hygrothermal aging and chloride exposure, as well as *in situ* environmental conditioning to multiple environments in Virginia. The study also included a small subset of fatigue-tested specimens, as well as a hypothetical *in situ* cost comparison to assess the economics of strengthening steel structures using the CFRP materials used in this project.

The results showed that although a corroded steel surface does require a longer bond length compared with a smooth surface, a pitted surface due to corrosion has no negative effect on the bond strength between CFRP and steel. Furthermore, exposure to chlorides does not appear to affect that bond strength. However, strength reduction factors for hygrothermal and environmental aging should be included in the design to account for exposure to given conditions. Nevertheless, CFRP is a cost-effective method for strengthening corrosion-damaged steel members with moderate levels of surface pitting. The research can be useful in the development of guidelines that will assist engineers determine if a CFRP retrofit solution is applicable in a given environmental setting and appropriate for the level of deterioration of the structure.

17. Key Words: carbon fiber-reinforced polymers, steel, bond, durability, hygrothermal, corrosion, corroded surface, environmental exposure, economic comparison, fatigue	18. Distribution Statement: No restrictions. This document is available to the public through NTIS, Springfield, VA 22161.		
19. Security Classif. (of this report): Unclassified	20. Security Classif. (of this page): Unclassified	21. No. of Pages: 74	22. Price:

Form DOT F 1700.7 (8-72) Reproduction of completed page authorized

FINAL REPORT

THE EFFECTS OF SURFACE CONDITION AND LONG-TERM ENVIRONMENTAL EXPOSURE ON THE BOND BETWEEN CFRP AND STEEL

Abril Yu-Shan, Ph.D.
Engineer
Thornton Tomasetti

Bernard L. Kassner, Ph.D., P.E.
Research Scientist
Virginia Transportation Research Council

Audrey Moruza
Senior Research Scientist
Virginia Transportation Research Council

Matthew Hebdon, Ph.D., P.E.
Associate Professor
Department of Civil, Architectural and Environmental Engineering
The University of Texas at Austin

Maryam Shakiba, Ph.D.
Assistant Professor
Ann and H.J. Smead Aerospace Engineering Sciences
University of Colorado Boulder

Bernardo Carrera
Associate Project Consultant
Simpson Gumpertz & Heger

Preet Jiwani
Graduate Engineer
Walter P Moore

Virginia Transportation Research Council
(A partnership between the Virginia Department of Transportation
and the University of Virginia since 1948)

Charlottesville, Virginia

August 2026
VTRC 27-R04

DISCLAIMER

The contents of this report reflect the views of the authors, who are responsible for the facts and the accuracy of the data presented herein. The contents do not necessarily reflect the official views or policies of the Virginia Department of Transportation, the Commonwealth Transportation Board, or the Federal Highway Administration. This report does not constitute a standard, specification, or regulation. Any inclusion of manufacturer names, trade names, or trademarks is for identification purposes only and is not to be considered an endorsement.

ABSTRACT

As the existing steel infrastructure inevitably continues to age and deteriorate, engineers are increasingly looking for innovative and effective methods for repairing and maintaining existing steel bridges, which are susceptible to corrosion damage when exposed to aggressive environments and deicing salts. Conventional methods for repairing steel bridges can be labor intensive and time consuming and add considerable weight to the existing structure. One alternative is to utilize carbon fiber reinforced polymers (CFRPs). Many studies have documented CFRP's ability to enhance the strength of existing structures while having a high strength-to-weight ratio and the added benefit of being noncorrosive. However, most of these studies have focused on the bond behavior between CFRP and steels having a smooth surface condition, which is not representative of deteriorated structures in need of retrofitting. Further research has examined the durability of CFRP-steel bonds but under conditions that do not reflect the service life conditions for typical bridge applications.

This study examined the effects of the surface condition and environmental exposure on the bond between steel and two different CFRP materials, one having a normal modulus and the other an ultra-high modulus. The researchers evaluated the influence of corrosion and simulated corrosion pitting to determine whether structures with non-uniform surfaces are viable candidates for CFRP retrofits. In addition, the durability of CFRP-steel bonded, double-strap jointed specimens was investigated through laboratory hygrothermal aging and chloride exposure, as well as *in situ* environmental conditioning to multiple environments in Virginia. The study also included a small subset of fatigue-tested specimens, as well as a hypothetical *in situ* cost comparison to assess the economics of strengthening steel structures using the CFRP materials used in this project.

The results showed that although a corroded steel surface does require a longer bond length compared with a smooth surface, a pitted surface due to corrosion has no negative effect on the bond strength between CFRP and steel. Furthermore, exposure to chlorides does not appear to affect that bond strength. However, strength reduction factors for hygrothermal and environmental aging should be included in the design to account for exposure to given conditions. Nevertheless, CFRP is a cost-effective method for strengthening corrosion-damaged steel members with moderate levels of surface pitting. The research can be useful in the development of guidelines that will assist engineers determine if a CFRP retrofit solution is applicable in a given environmental setting and appropriate for the level of deterioration of the structure.

FINAL REPORT

THE EFFECTS OF SURFACE CONDITION AND LONG-TERM ENVIRONMENTAL EXPOSURE ON THE BOND BETWEEN CFRP AND STEEL

Abril Yu-Shan, Ph.D.
Engineer
Thornton Tomasetti

Bernard L. Kassner, Ph.D., P.E.
Virginia Transportation Research Council

Audrey K. Moruza
Senior Research Scientist
Virginia Transportation Research Council

Matthew Hebdon, Ph.D., P.E.
Associate Professor
Department of Civil, Architectural and Environmental Engineering
The University of Texas at Austin

Maryam Shakiba, Ph.D.
Assistant Professor
Ann and H.J. Smead Aerospace Engineering Sciences
University of Colorado Boulder

Bernardo Carrera
Associate Project Consultant
Simpson Gumpertz & Heger

Preet Jiwani
Graduate Engineer
Walter P Moore

INTRODUCTION

As the bridge inventory in the United States continues to age and deteriorate, engineers are increasingly looking for innovative and effective methods for repairing and maintaining existing structures, which are susceptible to corrosion damage when exposed to aggressive environments and deicing salts. The Federal Highway Administration (FHWA) reports that, as of 2022, more than 12% (21,345 bridges) of the steel bridges in operation in the National Bridge Inventory are in poor condition (FHWA, 2022a). During the past 30 years, the number of steel bridges in fair condition increased by 32.7%, and the number of steel bridges in good condition decreased by 28.1%. The conventional method for repairing corroded steel structures consists of attaching steel plates to the members through bolting, riveting, or welding (Hollaway and Cadei, 2002). However, these retrofit methods can be labor intensive and time consuming and add weight to the existing structure. One alternative for enhancing the strength of deteriorated steel structures is utilizing carbon fiber reinforced polymers (CFRPs).

Studies have extensively documented CFRP's ability to enhance the strength and fatigue life of existing structures (Kamruzzaman et al., 2014; Zhao and Zhang, 2007). Furthermore, CFRP offers the benefits of being noncorrosive and having a high strength-to-weight ratio, thus minimizing additional dead load on the existing structure. However, most research on steel strengthening has focused on the bond behavior of CFRP to steels having a smooth surface condition, which does not represent deteriorated structures in greater need of strengthening (Bocciarelli et al., 2007; Fawzia et al., 2010; Fernando, 2010; Pang et al., 2021; Wang et al., 2016b; Wu et al., 2012; Xia and Teng, 2005). Other research has examined the durability of CFRP-steel bonds relative to moisture, elevated temperatures, and chlorides (Agarwal et al., 2015; Bai et al., 2014; Dawood and Rizkalla, 2010; Hartanto et al., 2018; Heshmati et al., 2017a, 2017b; Liu et al., 2016; Nguyen et al., 2012; Pang et al., 2020; Yang et al., 2019a; Yang et al., 2019b; Yu et al., 2018). The results from these studies are not consistent, leaving little consensus on the long-term weatherability factors for CFRP. Moreover, there have been relatively few studies on the effects of the surface condition of weathered steel on the strength and durability of the CFRP-steel bonded systems. Therefore, any potential for rehabilitating and strengthening members with severe corrosion pitting or section loss requires further investigation.

Mechanisms that can degrade the bond between the two adherends include moisture absorption or transport, temperature cycles, deterioration of secondary bond forces, chloride exposure, galvanic corrosion, cracking, adhesive swelling and plasticization, and fatigue. Some of these mechanisms have been explored using intensive conditioning in a laboratory setting. However, such short-term but intense exposure conditions may not accurately reflect the physical environment that a steel structure is subjected to during its lifespan. Consequently, further investigations are required to assess the durability of the bond between CFRP and steel, as well as the effects of substrate surface roughness in actual environments for in-service structures. Without this assessment, engineers may be reluctant to adopt CFRP as a means of strengthening deteriorated structures.

PURPOSE AND SCOPE

The overall purpose of this study was to determine where and when the use of CFRP is an appropriate retrofit for deteriorated steel structures. The research assessed both the long-term durability and bond behavior of CFRP attached to steel with significant section loss, considering different environmental conditions that are representative across Virginia. The test results led to an economic comparison with alternative repair methods, culminating in the recommendations that will help engineers determine if this retrofit solution is (1) applicable in a given environmental setting, (2) appropriate for the level of deterioration of the structure, and (3) cost effective.

METHODS

Overview

To achieve these goals, the durability of the bond was investigated through *in situ* testing of a CFRP system bonded to steel and subjected to environmental conditions at several locations in Virginia. In addition, severe laboratory conditioning enhanced the effects of deterioration on CFRP attached to varied surface profiles resulting from corrosion section loss. More specifically, this study involved:

1. Design and fabrication of small-scale specimens
2. Effect of surface roughness on bond behavior
3. Laboratory environmental aging using:
    a. Hygrothermal cycles
    b. Chloride exposure cycles
4. *In situ* environmental exposure to a:
    a. Rural environment
    b. Marine environment
    c. Heavy deicing salts environment
5. Specimen testing, including:
    a. Surface roughness specimens
    b. Laboratory environmentally aged specimens
    c. *In situ* environmentally aged specimens
    d. Fatigue behavior
6. Economic analysis.

Design and Fabrication of Small-Scale Specimens

Specimen Design

To assess the effects of the surface condition and environmental aging on the behavior of CFRP-steel bonded interfaces, the researchers fabricated double-strap joint specimens and subjected them to uniaxial tensile testing. Figure 1 illustrates a schematic of a typical specimen. One end of the bond length, l_1 (3 in), was shorter than l_2 ($1.5l_1$, or 4.5 in) to ensure failure on the shorter end. The value of l_1 was chosen to be greater than the effective bond length, L_{eff}, so that the full strength of the bond between the steel and CFRP could develop. L_{eff} is the length required to achieve 97% of the maximum transferable load (Yuan et al., 2004), beyond which any increases to the bond length do not yield an increase in the ultimate load. Sherry (2021) calculated L_{eff} for the two composite materials in this study using existing bond strength models (Hart-Smith, 1973; Xia and Teng, 2005).

Materials

This study focused on two materials, A36 steel and carbon fiber reinforced polymers, which included two materials with different moduli of elasticity.

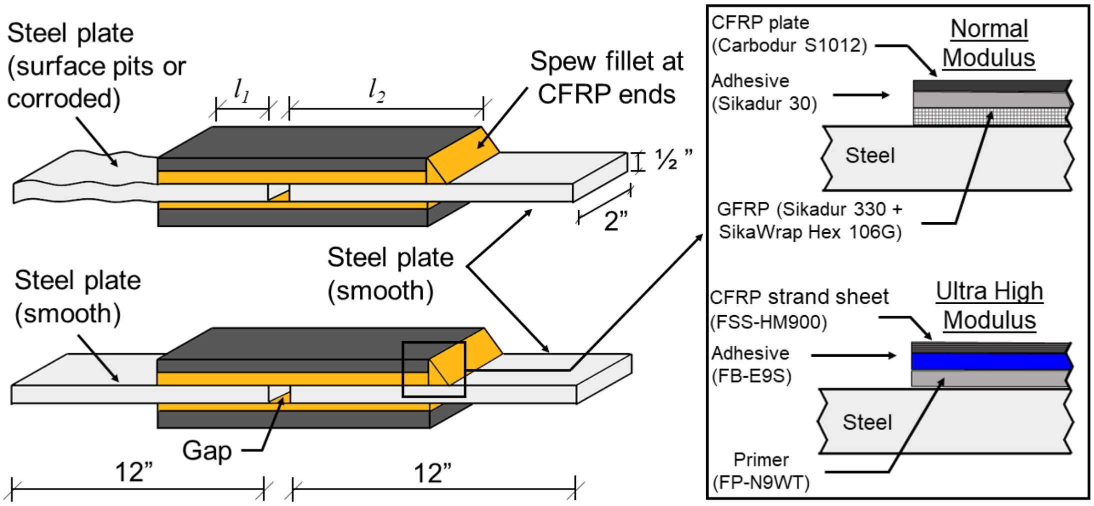

Figure 1. Schematic of Double-Strap Joint Specimen. CFRP = carbon fiber reinforced polymer; GFRP = glass fiber reinforced polymer.

Steel

The two ASTM A36 steel plates in the joints measured 12 by 2 by 0.5 inches and had a specified yield strength of 36 ksi. The modulus of elasticity was assumed to be 29,000 ksi.

Carbon Fiber Reinforced Polymer Materials and Adhesives

The double-strap joints were fabricated using two CFRP systems with different moduli of elasticity. The first was a normal modulus (NM) carbon fiber laminate (Sika Carbodur S1012); the second was an ultra-high modulus (UHM) CFRP strand sheet (Nippon FSS-HM900). These two strengthening elements had their own proprietary adhesive components, as indicated in Table 1, based on information provided by the manufacturers. Note that the NM system included a glass fiber reinforced polymer (GFRP) insulating layer to prevent galvanic corrosion between the steel and CFRP. Also note that, although no universally accepted classification system currently exists for CFRPs, this research adopted the categorization that Peiris and Harik (2015) proposed.

Table 1. Material Properties of Strengthening Materials

System Type	System Component	Tensile Strength (ksi)	Modulus of Elasticity (ksi)	Elongation at Break (%)
Normal Modulus	Carbodur S1012[a]	536	26,930	2.11
	Sikadur 30 [a]	3.2	1,643	0.23
	SikaWrap Hex 106G[b]	65.6	4,240	1.45
	Sikadur 330[c]	4.9	700	1.2
Ultra-High Modulus	FSS-HM900[d]	451	101,960	—
	FB-E9S[e]	4.45	580	—
	FP-N9WT [d]	7.70	—	—

[a] Sherry (2021). [b] Sika (2018). [c] Sika (2022). [d] Phan et al. (2015). [e] Nippon Steel Chemical and Material Co., Ltd. (2020). — = information not available.

Specimen Fabrication

Prior to bonding, the researchers sandblasted the bonding area of the steel plates and cleaned both the CFRP and steel surfaces with acetone. After aligning the two steel bars, the researchers applied the priming adhesive, which cured for 24 hours. Any surface irregularities were smoothed out using corresponding smoothing agents (e.g., Sikadur 330 and FB-E9S), which were cured for an additional 24 hours. The researchers then applied the adhesive uniformly to the steel surface and firmly pressed the CFRP into the adhesive, squeezing out any excess adhesive. To ensure the uniform adhesive thickness recommended by the manufacturer, the adhesive thickness was measured with a depth gauge during fabrication. Lastly, the researchers created spew fillets using the respective adhesive at the ends of the CFRP, gradually decreasing the thickness of the adhesive down to the steel in order to minimize stress concentrations and reduce the magnitude of shear and peeling stresses (Adams and Peppiatt, 1974; Hart-Smith, 1981). Once one face of the specimen was fully cured, the researchers repeated this procedure on the other face. All samples were prepared and cured at room temperature conditions, and the curing time was 7 and 10 days for the NM and UHM specimens, respectively.

Effects of Surface Roughness on Bond Behavior

Simulated Corrosion Pitting

To simulate pits on the substrate surface, fabricators machined a consistent pattern of surface pits on both faces of the steel bar with the shorter bond length for the purposes of minimizing fluctuations in the surface topography that typically occur in a naturally corrosive environment. The surface pits varied in width to represent a range of surface roughness. The patterns applied to the specimens consisted of a series of pits measuring 1⁄16, ⅛, ¼, and ½-inch in diameter, each approximately ⅛-inch deep. The pits were spaced as detailed in Figure 2. Specimens with no pits served as a baseline value for comparison. The specimens were identified according to a three-part nomenclature consisting of the CFRP material, surface pit size, and specimen number. The CFRP material was represented by the letters N (for Nippon) or S (for Sika); the surface pit size was designated by SP followed by the pit diameter size (0, 1⁄16, ⅛, ¼, and ½ in); and the last part denoted the test repetition. A total of 20 specimens were in this comparison.

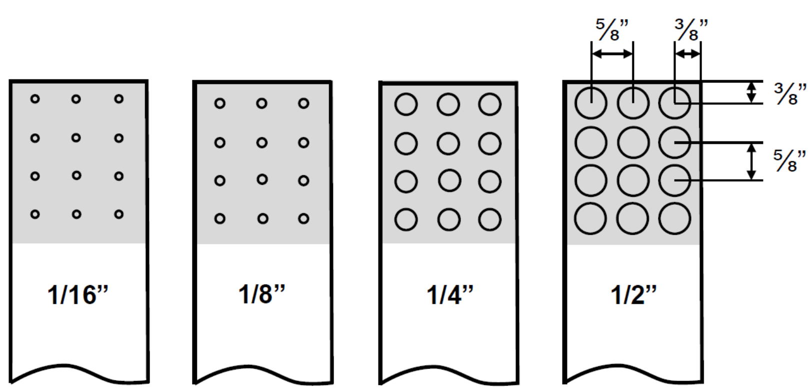

Figure 2. Geometry of Surface Pit Patterns

Surface Roughness Parameters

The primary mechanisms in adhesive bonding are physical and chemical bonding and mechanical interlocking (Baldan, 2004). Physical and chemical bonding are related to the material interfaces, whereas mechanical interlocking is dependent on the topography of the interface. Numerous surface roughness parameters exist to characterize the texture of a surface (International Standards Organization [ISO], 2021a). To assess the effects of roughness on the bonding behavior of CFRP-steel adhesively bonded joints, the researchers identified the roughness average, R_a, the root-mean-square roughness, R_q, and the average maximum height, R_z, expressed as:

$$R_a = \frac{1}{n} \sum_{i=1}^{n} |Z_i| \qquad \text{(Equation 1)}$$

$$R_q = \sqrt{\frac{1}{n} \sum_{i=1}^{n} Z_i^2} \qquad \text{(Equation 2)}$$

$$R_z = \frac{1}{n} \sum_{i=1}^{n} |R_{ti}| \qquad \text{(Equation 3)}$$

Where:
Z_i = the vertical distance from the mean line of the surface profile.
R_{ti} = the maximum height of the profile within a sampling segment i.
n = is the number of points.

The surface topography of the steel substrate was measured using the digital image correlation (DIC) method, which captured an image of the bonding area. The DIC software detected any surface irregularities or local defects by comparing the depth of those defects (that is, the machined pits) to a nominal depth value. The given roughness parameter was an average of 10 surface profile measurements taken along the width of the bonded area of each of the pit patterns in Figure 2.

Nonlinear Bond-Slip Behavior

The bond-slip model is a stress-deformation relationship that describes the relation between the interfacial shear stress and the relative slip. The deformation of the interface is the relative slip (displacement) between the CFRP laminate and the substrate. Bond-slip models are critical for understanding the debonding process and predicting the behavior of CFRP-strengthened steel components.

Optical measurements, such as the DIC method, can provide full-field measurements based on image processing. Continuous strain and displacement data can be obtained directly from DIC by analyzing a path along the bond length. The relative slip between the CFRP plate and the steel substrate can be calculated by subtracting the average steel displacement from the

CFRP displacement at the same position. Processing the data is necessary because noise due to the strain resolution of the DIC system, ambient noise, or non-uniform illumination can affect the accuracy of the bond-slip relationship. A fitting procedure is an effective method for reducing fluctuation in the strain data and determining the bond-slip curve of CFRP-steel interfaces (Shi et al., 2013; Wang et al., 2016a). Consequently, the nonlinear bond-slip curve can be determined from the fitting Equations 4 through 7:

$$\varepsilon_f(x)=\frac{\frac{a}{b}}{1+e^{\frac{x-x_0}{b}}} \qquad \text{(Equation 4)}$$

$$s(x)=a\ln\left(1+e^{\frac{x-x_0}{b}}\right) \qquad \text{(Equation 5)}$$

$$\tau(x)=\frac{a}{b^2}\ \frac{E_f t_f e^{\frac{x-x_0}{b}}}{\left(1+e^{\frac{x-x_0}{b}}\right)^2} \qquad \text{(Equation 6)}$$

$$\tau(s)=E_f t_f\frac{\alpha}{\beta^2}\ \left(1-e^{-\frac{s}{a}}\right) \qquad \text{(Equation 7)}$$

Where:
x = the distance from the joint.
$\varepsilon_f(x)$ = the CFRP strain.
$s(x)$ = the relative slip.
$\tau(x)$ = the interfacial shear stress at a given load, as a function of the distance from the joint.
$\tau(s)$ = the average interfacial shear stress, as a function of slip, and a, b, x_0, α, and β are fitting coefficients that are unique for each bond-slip curve. Equations 5 and 6 are calculated by integrating and differentiating Equation 4, respectively. A well-known fact is that the bond-slip behavior is similar at different stages during loading. To reflect the average performance along the CFRP interface, the fitting coefficients are reduced to a single set of fitting parameters, α and β, through a best-fit analysis of bond-slip curves at various loading stages using Equation 7.

Figure 3 shows the fitting procedure for calculating the bond-slip relationship. The DIC strain data at a given load during testing were fitted using Equation 7. Figure 3a exemplifies the results of this process. The same fitting coefficients obtained from Equation 4 were then used in Equations 5 and 6. Figure 3b and Figure 3c show the typical relative slip and interfacial shear stress distributions, respectively, obtained via the fitting procedure. Lastly, the interfacial shear stress (Equation 6) was plotted against the respective relative slip (Equation 5) to obtain the bond-slip curve. This process was repeated for different stages during loading. It can be seen from Figure 3d that the bond-slip curves are similar at different loading stages. However, the

fitting coefficients a, b, and x_0 are unique for each bond-slip curve. To reflect the average performance
along the CFRP interface, the fitting coefficients were reduced to a single set of fitting parameters α and β through a best-fit analysis of the 10 bond-slip curves at different loading stages using Equation 7, as the solid line in Figure 3d presents.

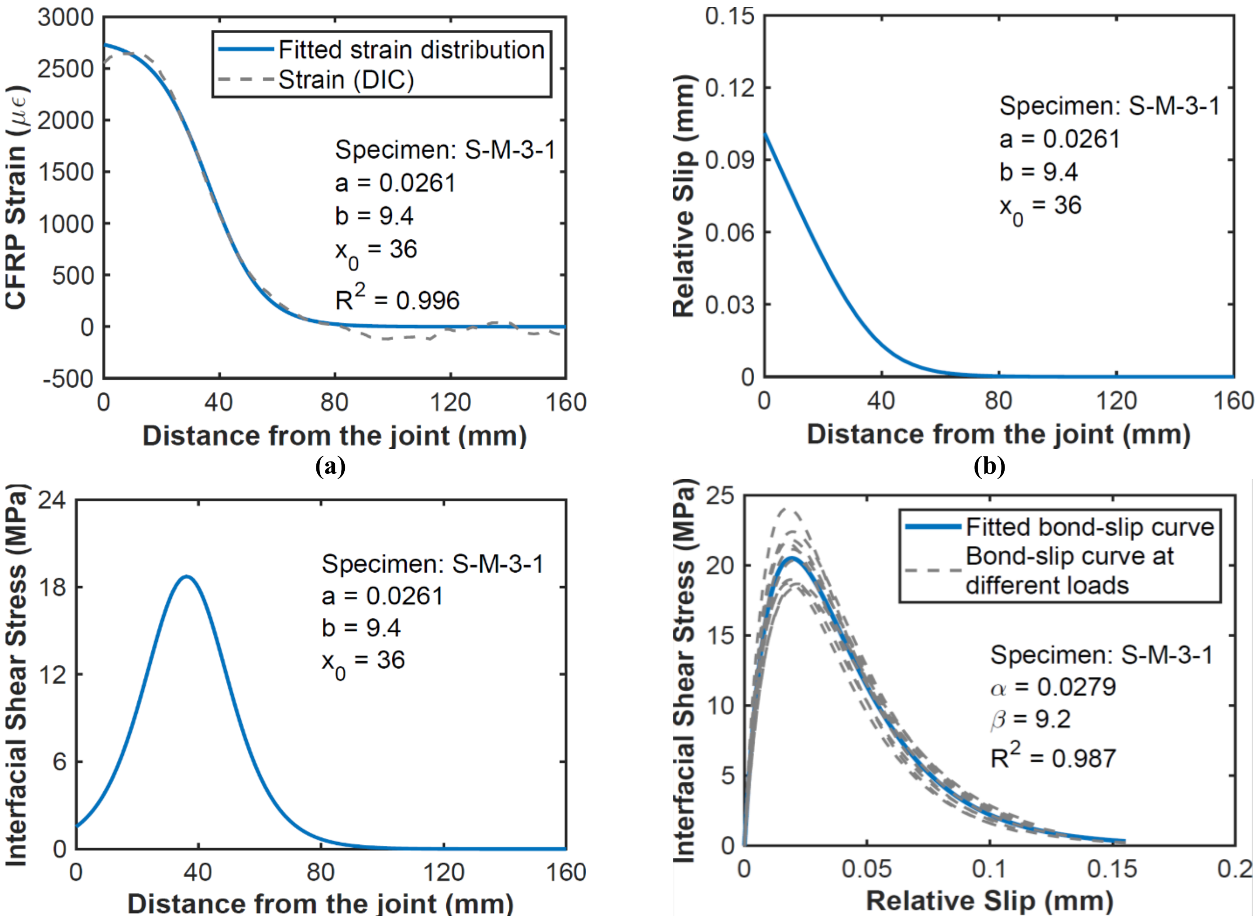

(a) (b) (c) (d)

Figure 3. Fitting method for calculating the bond-slip relationship: (a) relative slip, (b) CFRP strain, (c) interfacial shear stress, and (d) bond-slip relationship. CFRP = carbon fiber reinforced polymer; DIC = digital image correlation.

This fitted bond-slip analysis results in a nonlinear curve that can be simplified into a bilinear curve defined by three key parameters: the maximum interfacial shear stress, τ_{max}; the elastic slip that corresponds to the maximum shear stress, s_1; and the maximum relative slip, s_f, which is calculated as:

$$s_f = \frac{2G_f}{\tau_{max}} \qquad \text{(Equation 8)}$$

G_f, the interfacial fracture energy, is equal to the area under the bond-slip curve and is defined as the energy required to debond a local bond element (Wu et al., 2002). Therefore, G_f equals the integration of Equation 7, such that:

$$G_f = \int_0^\infty \tau(s)ds = \frac{1}{2}E_f t_f \left(\frac{\alpha}{\beta}\right)^2 \quad \text{(Equation 9)}$$

Furthermore, the maximum interfacial shear stress, τ_{max}, and the slip corresponding to τ_{max}, s_{max}, can be expressed as:

$$\tau_{max} = \frac{1}{4}E_f t_f \left(\frac{\alpha}{\beta^2}\right) \quad \text{(Equation 10)}$$

$$s_{max} = \frac{\alpha \ln(2)}{\alpha_1} \quad \text{(Equation 11)}$$

Where the set of fitting parameters α and β are obtained through a best-fit analysis of bond-slip curves at various loading stages (Equation 7), and α_1 is a corrective coefficient that adjusts the value of maximum aged bond stress according to the bond stress for the unaged condition.

However, the bond-slip model approach is only applicable to cohesive failures because the equilibrium considerations in which it is based do not capture other failure mechanisms (Wu et al., 2012; Yuan et al., 2004). For this reason, specimens that failed exclusively because of CFRP rupture are excluded from this analysis.

Comparison of Theoretical Versus Experimental Failure Loads

The experimental results were compared with three existing analytical models for predicting the bond strength of adhesively bonded joints:

$$P_u = N \cdot b_f \sqrt{2G_f E_f t_f} \quad \text{(Equation 12)}$$

$$P_u = N \cdot b_f \sqrt{2G_f E_f t_f \left(1+\frac{1}{\delta}\right)} \quad \text{(Equation 13)}$$

$$P_u = b_f \sqrt{2\tau_f t_a \left(\frac{1}{2}\gamma_e + \gamma_p\right) 4E_f t_f \left(1+\frac{2E_f t_f}{E_s t_s}\right)} \quad \text{(Equation 14)}$$

Where:
N = number of interfaces working in parallel (2 for double-strap joints).
δ = stiffness ratio of the joint, defined as:

$$\delta = \frac{E_s t_s b_s}{N E_f t_f b_f}$$

Where:
E_s = elastic modulus of the steel plate.
t_s = thickness of the steel plate.
b_s = width of steel plate.
E_f = elastic modulus of the CFRP laminate.
t_f = thickness of the CFRP laminate.
b_f = width of the CFRP laminate.
γ_e = elastic shear strain of the adhesive, defined as $\gamma_e = \tau_f/G_a$.
γ_p = plastic shear strain of the adhesive, defined as $\gamma_p = 3\gamma_e$ for normal-modulus CFRP and $5\gamma_e$ for high-modulus CFRP.

Wu et al. (2002) proposed Equation 12 for pull-pull joints with a linear bond-slip relationship that suddenly dropped to zero after fracture and Equation 13 for joints that exhibited a small degree of softening before the bond strength reduced to zero. Both equations were extended for the case of double-strap joints by pre-multiplying the predictive ultimate load by the number of interfaces (Bocciarelli et al., 2007). The main distinction between Equations 12 and 13 is the presence of the stiffness ratio, δ, which has been found to influence the behavior of CFRP-steel joints with two interfaces, such as double-strap joints (Wu et al., 2002). For this reason, Equation 11 is commonly used for joints with one working interface, such as single-lap joints. However, the researchers considered Equation 13 in this study for the purposes of comparison. Moreover, Equation 14 is Hart-Smith's (1973) solution for the failure loads of adhesively bonded double-lap joints when $E_s t_s \geq 2E_f t_f$. In this work, Equation 14 is only applicable to the NM strengthening system.

Corrosion

The researchers tested an additional 20 double-strap joint specimens to study the effects of a naturally corroded surface on the bond behavior of CFRP steel joints. The corroded steel plates were cut from steel members that had once been in service in an actual bridge. Four specimens for each of the four different levels of corrosion severity were obtained, along with a smooth surface with no corrosion serving as a reference for comparison (Figure 4). Similarly, the shorter end of the bond corresponded to the corroded steel plate.

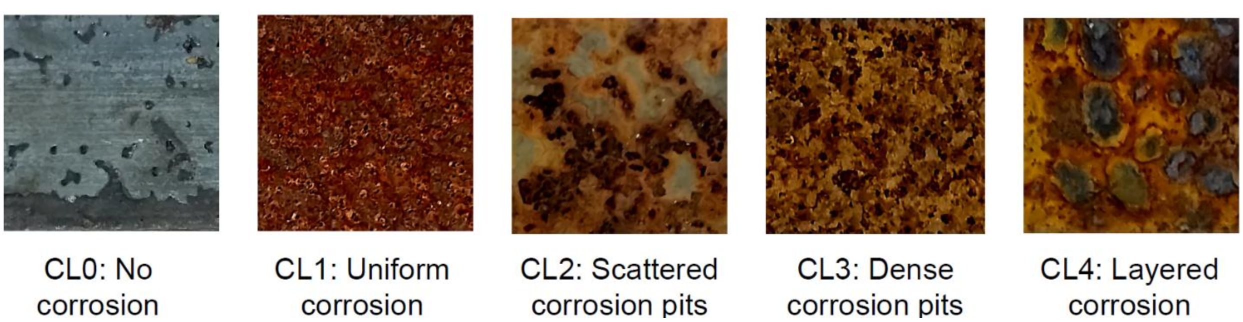

Figure 4. Surface Condition of Corroded Steel Plates. CL = corrosion level.

The specimens were labeled according to a three-part nomenclature: the CFRP material, represented by the letters N (for Nippon) or S (for Sika); the corrosion level, designated by CL followed by the level of corrosion (0, 1, 2, 3, 4); and the specimen number.

Surface Characteristics: Roughness Parameters

The standardized statistical parameters specified in ISO (2021b) can describe the areal characteristics of a surface. Although numerous areal surface texture parameters exist, the researchers considered two categories of these parameters: amplitude, which describes the height of the surface roughness, and hybrid, which combines both height and spacing characteristics of the surface. Therefore, to assess the effects of corrosion on the behavior of CFRP-steel adhesively bonded joints, the researchers selected the average surface height, S_a, and the maximum surface height, S_z, as amplitude parameters, and designated the developed interfacial area ratio, S_{dr}, as a hybrid parameter. These area parameters are expressed as:

$$S_a = \frac{1}{\eta_x \eta_y} \sum_{j=1}^{\eta_y} \sum_{i=1}^{\eta_x} \left| \eta \left(x_i, y_j \right) \right| \qquad \text{(Equation 15)}$$

$$S_z = S_p - S_v \qquad \text{(Equation 16)}$$

$$S_{dr} = \frac{1}{A} \left(\sum_{j=1}^{\eta_y} \sum_{i=1}^{\eta_x} A_{ij} - A \right) \qquad \text{(Equation 17)}$$

Where:
S_p = the maximum peak amplitude.
S_v = minimum valley amplitude.
$\eta(x_i, y_j)$ = the roughness data matrix of size η_x by η_y.
A = the nominal area.
A_{ij} = the incremented surface area due to roughness.

Similarly, the surface topography of the corroded steel plates was measured using the DIC system as previously described. The parameters were calculated for both faces of the corroded steel plates, and the average value of the two surfaces was taken as the surface roughness parameter.

Bond-Strength Model Development

A fracture energy-based model is a suitable approach for predicting the debonding strength of CFRP-to-steel bonded interfaces. The fracture mechanics-based model relies on the interfacial fracture energy, G_f, associated with the propagation of a crack in the adhesive layer, at the interface between adherends, or a combination of the two. If G_f is known, Equations 12 and 13 can predict the failure load of single- and double-shear joints, respectively. Previous research has found G_f to be related to the adhesive thickness, t_a, and the mechanical properties of the adhesive, such as the tensile strain energy, R (defined as the area under the uniaxial tensile stress-strain curve), the tensile strength, $f_{t,a}$, and the shear modulus, G_a (Bocciarelli et al., 2007; Fernando, 2010; Xia and Teng, 2005). As a result, Equation 18 was proposed to determine the interfacial fracture energy:

$$G_f = A(t_a R)^B K_f^C \quad \text{(Equation 18)}$$

Where:
K_f = the axial stiffness of the CFRP laminate and is defined as: $K_f = A_f E_f$.
A_f = the cross-sectional area of the CFRP composite.
A, B, and C are unknown coefficients.

In order to have a higher number of experimental results to determine the coefficients of the proposed analytical model, the test results of 82 CFRP-steel bonded joints from existing studies (Chotickai, 2018; Li et al., 2019; Phan et al., 2015; Xu et al., 2020) and the present research were compiled to build a database. The database consists of both double-strap joints and single-shear specimens, as well as a variety of CFRP materials and adhesives. Given that G_f was not provided for every test in the literature, the interfacial fracture energy was back-calculated in the database from the ultimate load using either Equation 12 or 13. Ultimately, the coefficients A, B, and C in Equation 18 were optimized to minimize the error between the theoretical predictions and the experimental results.

Laboratory Environmental Aging

Hygrothermal Cycles

Although a wide range of studies have examined bond behavior under various environmental conditions, ranging from elevated cases (high temperature and humidity) to freeze-thaw cycles (freezing temperatures and low humidity), most research has focused on constant conditions, be that temperature (often exceeding the glass transition temperature) or saturated wet or very arid cycles. Although valuable insight can be obtained from such conditions, these scenarios do not reflect the actual environmental conditions bridges are in. To provide a proper assessment of the moisture and temperature effects on the bond durability of CFRP-steel joints, cyclic temperature, appropriate relative humidity, and reasonable exposure times need to be considered. For this reason, 10-year weather data from three locations in Virginia (National Climatic Data Center [NCDC], 2021) were analyzed to derive the 24-hour cyclic temperature protocols, as Figure 5 shows.

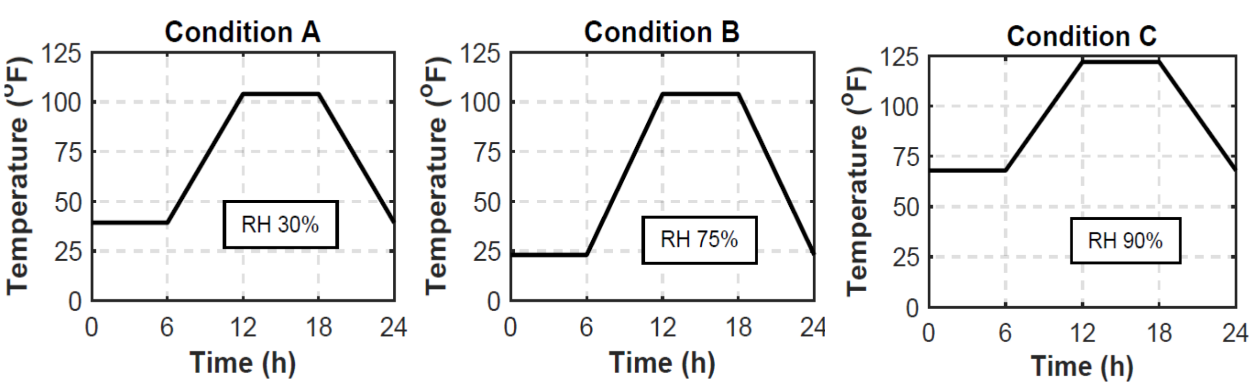

Figure 5. 24-Hour Hygrothermal Cycles. RH = relative humidity.

Environmental conditioning was achieved using a Cincinnati Sub-Zero ZP-16 environmental chamber, which precisely controlled the temperature and relative humidity. The total exposure time for 60 double-strap joints with smooth (that is, no simulated corrosion pitting) steel bars (Figure 1) was up to 1,344 hours (56 days). Also, two unexposed samples for each CFRP material served as a reference. To monitor the residual strength of the bond throughout the aging period, NM and UHM specimens were removed from the chamber and tested every 28 and 7 cycles, respectively.

The combined effects of hygrothermal aging and surface condition were also investigated using 48 specimens with the UHM composite material. Surface roughness consisted of ½-inch diameter, $^{1}/_{64}$-inch deep machined pits on both faces of the steel bar with the shorter bond length. The spacing of the pits remained the same, as Figure 2 illustrates. The researchers tested two specimens every seven cycles to track the effect of the hygrothermal aging on specimens with roughened surfaces over time.

Chloride Exposure Cycles

For the purposes of this study, the researchers based a "high" concentration of chlorides on the work done by Groshek (2017), who followed a modified version of SAE International's (2016) testing standard, J2334, *Laboratory Cyclic Corrosion Test*. Although the J2334 standard calls for 0.5% (by mass) sodium chloride (NaCl), Groshek used a 5% solution because that concentration resulted in laboratory corrosion products containing 2% chlorides, which was what was found on in-service steel bridges. The concentrations of calcium chloride and sodium bicarbonate remained unchanged from the original J2334 standard.

In Virginia, the application rate of deicing chemicals during snow events varies from county to county, primarily depending on geography and population density (Balakumaran and Weyers, 2019). For the purposes of this study, the "high" concentration in the modified J2334 standard was equated to the highest average chloride application rate amongst the nine Virginia Department of Transportation (VDOT) districts, or 7.41 tons of chloride per lane-mile (tCl^-/l-m), determined by Balakumaran and Weyers (2019). Accordingly, a "low" district average application rate of 1.29 tCl^-/l-m equated to 0.87% NaCl. Lastly, the researchers conditioned a third batch of specimens using 3.5% NaCl to simulate ambient exposure in a marine environment.

The researchers conditioned each of three batches of specimens in Auto Technology Company's Cyclic Corrosion Chamber, Model CCT-NC-40, using the spray option with one of the three aforementioned NaCl concentrations. Chloride solutions were mixed as needed and stored in a solution tank connected to the chamber. The researchers tested and recorded the conductivity and pH of each batch of solution.

Polyvinyl chloride angles supported the specimens upright on their sides, with approximately 0.5 in between adjacent faces of the CFRP components of these specimens. The spray nozzles were in position to evenly apply chloride solution to both faces of all specimens

(Figure 6). Every seven 24-hour cycles, the researchers removed two specimens to test the effects of chloride exposure over time.

Figure 6. Chloride Exposure Specimens Positioned in the Corrosion Chamber for Conditioning

Data analysis included comparisons within the different chloride exposure levels and surface condition types. In cases with unequal numbers of samples for statistical analysis, the researchers randomly removed one of the two test results for the affected exposure duration when such equality was required (e.g., two-factor analysis of variance tests with replication).

In Situ **Environmental Exposure**

To assess the bond durability of CFRP-steel systems, 48 CFRP-steel double-strap joints with smooth steel bars (Figure 1) were exposed to *in situ* field conditions at three locations: underneath Virginia Structure No. 080-6055, representing a rural condition with low deicing salt usage; at the Temperanceville Area Headquarters, representing a marine setting; and underneath Virginia Structure No. 029-2162 and adjacent to Interstate 95, which is exposed to heavy deicing salts during the winter. Deicing salts tend to have a significant influence on the corrosion of steel (Balakumaran and Weyers, 2019), which, in turn, can have long-term implications on the bond durability between CFRP and steel. These *in situ* specimens were conditioned for up to 1 year and tested every 3 months to examine any potential environmental degradation.

The combined effects of environmental aging and surface condition were also investigated only for the UHM material using 24 specimens that were similar to those for the laboratory-conditioned specimens with roughened surfaces. The researchers gathered these specimens from each of the three *in situ* locations and tested them every 3 months for up to 1 year.

Figure 7 presents the specimen placements in the studied environments. Specimens exposed to rural and heavy deicing salt conditions were placed on racks located on the ground directly below the beams of a steel bridge. Therefore, samples were bound to be exposed to similar conditions experienced by the bridge members. Because of the inaccessibility to a bridge in a coastal area, the rack containing the specimens exposed to a marine environment was not placed below a bridge. The selection of a site with heavy deicing salt usage and the placement of the rack were based on chloride application levels (Balakumaran and Weyers, 2019) and vehicle salt-spray dispersion (Lottes and Bojanowski, 2013; Williams and Stensland, 2006).

Figure 7. Environments Investigated for *In Situ* Environmental Exposure (base map retrieved from Google Maps)

Exposure Conditions

Because the specimens were aged throughout a period of 1 year, the temperature and relative humidity conditions were anticipated to vary daily and as the seasons changed. Figure 8 depicts the hourly temperature and relative humidity conditions, collected from nearby weather stations (NCDC, 2021), for each of the studied environments. In Figure 8, a T followed by the test number denotes the test identification. The weather data revealed that the temperature varied from -6–92°F, 9–100°F, and 13–96°F, and the relative humidity ranged from 14–100%, 16–100%, and 21–100% for the rural, heavy deicing salts, and marine environments, respectively.

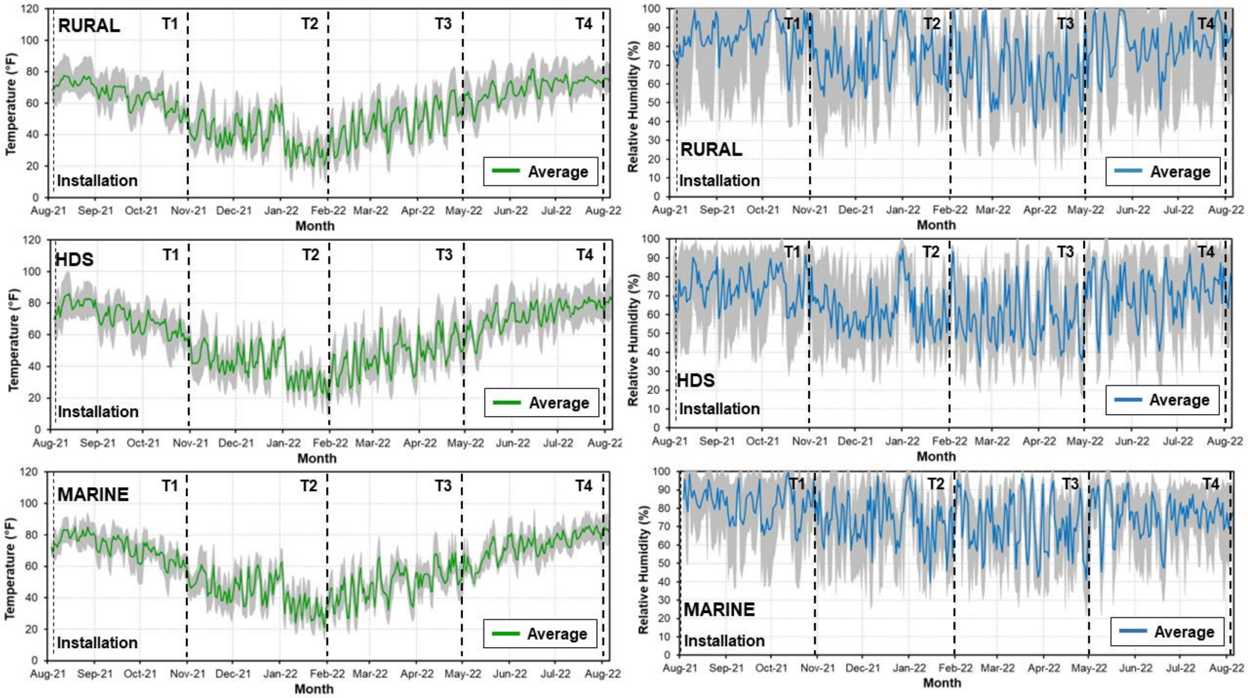

Figure 8. Hourly Temperature and Relative Humidity Data for the Studied Environments. HDS = heavy deicing salts.

Specimen Testing

Surface Roughness Specimens

The specimens designed to study the effects of surface roughness on bond behavior were tested using either an MTS Insight Electromechanical universal testing machine with a 34-kip capacity at a rate of 0.001 in/s or on an MTS Landmark 370.50 universal testing machine with a 110-kip capacity at a rate of 0.004 in/min.

Conditioned Specimens

The hygrothermal and *in situ* specimens were tested in uniaxial tension on an MTS Insight Electromechanical universal testing machine with a 34-kip capacity at a rate of 0.001 in/s, and the chloride exposure specimens were tested in a 55-kip capacity MTS 319.25 testing machine at a rate of 0.004 in/min.

Strain Data Acquisition

For both the surface roughness and the conditioned specimens, a DIC non-contact measurement system was utilized to record full-field strain measurements of the front face of the specimens. The surface of the specimens was prepared before testing with a high-contrast stochastic pattern created with a white background using white matte paint, followed by a distribution of black dots produced with matte spray paint. The DIC system consisted of a pair of 12 Megapixel CMOS sensors on an 800-mm adjustable base manufactured by GOM. Images were captured at a rate of 12 Hz but were stored using a "ring buffer" element such that images were stored every 4 seconds prior to failure and every 0.083 second shortly before and after failure, for a total of 6 seconds. The DIC analysis was performed using the Aramis Professional 2019 software, in which the strain distribution was calculated based on undeformed and deformed images.

Fatigue Specimens

A two-part experimental program was conducted to investigate the bond behavior of CFRP-to-steel joints under fatigue loading using two different surface conditions: a smooth surface and a surface with simulated corrosion pitting. The simulated corrosion pitting consisted of ½-inch diameter, $^{1}/_{64}$-inch deep machined pits on both faces of the steel bar with the shorter bond length. The spacing of the pits is the same as depicted in Figure 2. The specimens were fabricated using UHM composite materials with the same geometry shown in Figure 1. In the first part of the experiment, the researchers subjected 34 double-strap joints to three different amplitudes of tensile cyclic loading until failure.

When studying total life approaches, stress, strain, or any form of amplitude is plotted as a function of the number of cycles until failure, N_f. Typical stress analyses of bonded joints have shown that no unique relation exists between an easily measured shear stress and the maximum stress (Shenoy et al., 2009). For this reason, an applied force amplitude is often used instead of a conventional stress amplitude to generate the alternative F-N curves.

To determine the three aforementioned amplitudes, the researchers initially determined the maximum static tensile capacity (F_u) by testing 12 control specimens under a quasi-static tensile load at a displacement-controlled rate of 0.004 in/min until failure. The three force amplitudes with maximum fatigue load (F_{max}) values then became $0.6F_u$, $0.5F_u$, and $0.4F_u$. Note that the researchers selected the fractions of F_u to achieve a relationship within the load-versus-number-of-cycles curve. F_{min} was then selected to achieve a *de minimis* tensile load without reaching zero force. Prior to fatigue cycling, each specimen was initially loaded quasi-statically up to the mean force level and held for 15 seconds. The fatigue protocol was a load-controlled, constant force amplitude test with a sinusoidal shape at a frequency of 6 Hz, as recommended by Vassilopoulo (2020). The frequency was based on the performance of the pump and the MTS frame. All the tests were performed under a load ratio, R, of 0.1 because similar experiments have shown that the load ratio has only a marginal influence on the fatigue life of double-strap joints (Colombi and Fava, 2012). These data helped to develop the F-N curves.

In addition, the researchers developed a nonlinear strength wear-out model to predict the residual strength of fatigued double-strap joints using 18 additional specimens with the same geometry and materials as before, as well as the force amplitudes. However, these specimens were tested up to a certain number of cycles and then statically until failure to establish an empirical relationship between the number of cycles and the residual strength, F_r:

$$F_r(N)=F_u-\alpha(F_u\text{-}F_{max})N^{\mu} \qquad \text{(Equation 19)}$$

where N is the number of cycles, and μ and α are strength degradation parameters obtained through experimental data. In this model, the initial strength of the joint had to be equal to the quasi-static strength of the specimens, F_u, and failure occurred at a strength equal to the maximum fatigue load in the amplitude, F_{max}.

Both static and fatigue tests were performed with a 110-kip capacity MTS servo-hydraulic testing frame and using the MTS Model 793.10 MultiPurpose TestWare application for the loading protocols and for acquiring the test data.

Economic Analysis

As an alternative to conventional steel plate repairs, CFRP systems could be determined to be cost-competitive if three factors favor CFRP: current cost trends and the outlook for future costs, rules affecting federally funded transportation construction projects, and a hypothetical *in situ* cost comparison.

Recent and Current Cost Trends and Short-Term Outlooks

Under the definition used by the U.S. Bureau of Labor Statistics (BLS), "[t]he Producer Price Index (PPI) program measures the average change over time in the selling prices received by domestic producers for their output" (BLS, 2022a). The research team compared the Producer Price Index for both steel and CFRP strengthening systems used in this study.

Rules Affecting Federally Funded Transportation Construction Projects

The 2021 Infrastructure Investment and Jobs Act (IIJA; P.L. 117-58) extends coverage of the Buy America U.S. content preference law beyond the former limits of iron, steel, and specific manufactured goods in federal-aid projects and now includes nonferrous metals, plastic and polymer-based products, glass, lumber, drywall, and other products (including protective coatings) if permanently incorporated in any project funded under Title 23 of U.S. code (Congressional Research Service, 2021). Although some uncertainty still exists regarding the application of this law, the assumption in this study was that CFRP strengthening products would be judged to be ineligible for a waiver of P.L. 117. This study will examine the potential for legal impediments to strengthening steel structures with CFRP systems.

Hypothetical *In Situ* Cost Comparison

A 2018 VDOT Regular Advertisement and Award Process project for several steel bridges included strengthening webs and flanges with conventional steel plates as standalone repairs, separate from other bridge members (Figure 99). The researchers advanced the actual construction costs to 2022 dollars using the National Highway Construction Cost Index (FHWA, 2022b).

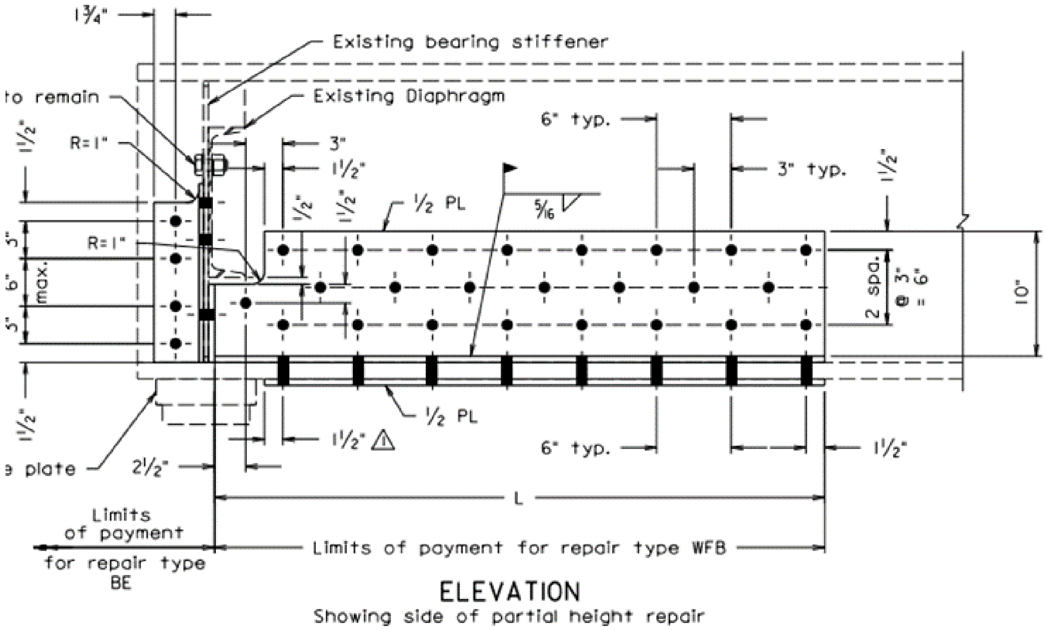

Figure 9. Example Partial-Height Web-Flange Repair of a Steel Beam, Taken from a VDOT Regular Advertisement and Award Process Project

Thus, hypothetically performing the same web and flange repairs with both the Sika and the Nippon strengthening systems was a relatively straightforward task, given the following assumptions:

1. The relative costs of steel plate and CFRP repairs, including installation costs, can be compared on a square foot basis.
2. The cost of CFRP installation (labor and equipment costs) per square foot can be estimated as equivalent to that of steel plate installation per square foot. This particular Regular Advertisement and Award Process did not require any special machinery other than a snooper platform to access below the bridge. Although steel plate repairs include welding, it is assumed that unspecified CFRP installation costs may be equivalent to the cost of welding.
   The base installation cost per square foot of steel plate in 2022 dollars was determined from the construction inspectors' Daily Work Records in the Site Manager electronic construction database. Mean hourly wage rates for welders, construction carpenters, and first-line supervisors of construction workers were taken from 2022 Virginia Employment Commission data (Virginia Employment Commission, 2022a, 2022b, 2022c), and a trailer-mounted under-bridge inspection unit was prorated at the 2022 weekly rate quoted by a Central Virginia regional rental facility.
3. Steel repair plates throughout this contract were specified as coated ASTM A709 Grade 36 steel. Contractual repair costs for steel plates include items or tasks for which the CFRP systems have equivalents: plate edge smoothing and squaring are analogous to cutting and fitting CFRP products to flanges and webs, bolting and welding are analogous to adhesive layer applications, and preparation of steel surfaces is common to all strengthening systems. However, the costs of magnetic particle testing, new fastener sets, weld testing, and weld inspection are not applicable to CFRP systems.

4. Bridge plans provided the length and height or width of the repair plate (of steel or CFRP) for webs and top flanges. However, when not otherwise specified, and given bolt spacings and end margins in bridge plans, the bottom plates of the flange repairs were calculated to be 4.2 inches shorter than the lengths of web plates or top plates of the flange repairs as a rule.

The research team developed Excel spreadsheets for calculating the costs of three different CFRP strengthening designs in place of steel plates for the repairs stipulated in the bridge plans:

1. The Sika strengthening system (the NM system) included Sika CarboDur plate, which was available in three widths. The spreadsheet "fit" these widths to the specified widths and heights of the steel repair plates to optimize using the widest plate, which had the lowest unit cost, and to minimize the amount of trimming or waste. The spreadsheet calculated the square foot of Sika system products required and applied vendor-provided layer prices to calculate the final cost of a given repair.
2. The Nippon system (the UHM system) included Nippon strand sheets that came in a single width. Although cutting the material to fit girder flanges and webs tends to be unavoidable, cutting down to the appropriate width is relatively easy, and the dimensions can be nearly identical to the steel repair plates.
3. A previous study employed an enhanced UHM strengthening system in which a second layer of primer for the elastic putty was added, and the Nippon strand sheet adhesive layer was applied in two additional layers (Sherry and Hebdon, unpublished report, 2021). To account for the application of three extra layers of primer and adhesive, the unit installation cost was 50% greater than the four-layer Nippon system.

Manufacturers' application rates for putty, resin, and adhesive layers were used for all calculations.

RESULTS AND DISCUSSION

Effects of Surface Roughness on Bond Behavior

Both simulated and natural corrosion specimens had variable degrees of surface roughness. The different surfaces yielded distinct curves for roughness parameters but mixed results in the failure mode and strength capacity, depending on the modulus of the CFRP. These results led to an improved empirical bond strength model.

Simulated Corrosion Pitting

Both the failure mode and the load for the simulated corrosion specimens with NM CFRP remained relatively constant regardless of the degree of pitting. However, the opposite was true for the UHM tests.

Surface Roughness Parameters

Figure 90 shows the variation of surface roughness with increasing pit diameter. Surface roughness characteristics consistently increased with pit diameter for all three parameters. The amplitude average parameters R_a and R_q reached a maximum value of 0.045 inch and 0.061 inch, respectively, and the amplitude parameter R_z attained a maximum value of 0.11 inch.

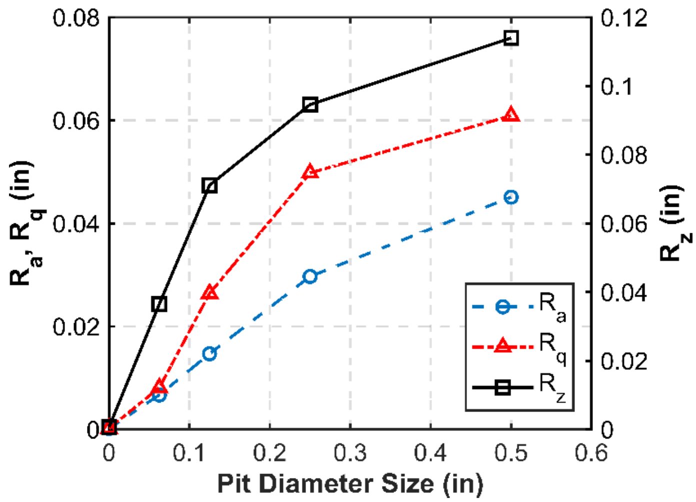

Figure 90. Variation of Surface Roughness Parameters with Increasing Pit Diameter. R_a = average roughness parameter; R_q = root-mean-square roughness parameter; R_z = average maximum height parameter.

Failure Modes

Table 2 presents the ultimate tensile load and corresponding failure modes for all the simulated corrosion specimens used for studying the effect of surface roughness. Note that failure typically started on one face of the joint, not on both faces simultaneously, and propagated from the joint to the ends of the CFRP laminate. Also, note that "Side A" is the face of the specimen with the DIC patterning, versus "Side B," which had no patterning. Figure 101 shows the typical failure modes for NM double-strap joints. The failure mode did not change substantively as the pit diameter increased from 0 to 0.5 inch, with the most common failure being a combination of cohesion failure and delamination, where the bond between the adhesive and the adherends was much stronger than the bond between the fibers and the resin matrix (Xia and Teng, 2005). For those specimens that failed in this combination, the delamination occurred predominantly near the end of the CFRP plate, where peel stresses are higher. The adhesion failures in Table 2 are an indication of poor steel surface preparation prior to bonding (Fernando, 2010). The NM specimens had similar failure loads regardless of the presence of surface pits or the failure mode.

Table 2. Experimental Results of Double-Strap Joints with Surface Pits

Specimen	P_u (kip)	G_f (lb/in)	Failure Mode	
			Side A	Side B
S-SP0-1	15.6	4.18	C/D	C/D
S-SP0-2	14.7	4.11	C/D	C
S-SP0.0625-1	15.7	4.42	A	C
S-SP0.0625-2	15.2	4.21	C	A

Specimen	P_u (kip)	G_f (lb/in)	Failure Mode	
			Side A	Side B
S-SP0.125-1[a]	15.6	5.07	C	C/D
S-SP0.25-1 [a]	17.1	5.55	C/D	A
S-SP0.5-1	13.5	3.57	C/D	A
S-SP0.5-2	17.0	5.02	C/D	C
N-SP0-1	19.8	2.97	C/R	A/C/R
N-SP0-2	19.1	—	R	R
N-SP0.0625-1	21.5	—	R	R
N-SP0.0625-2	21.5	—	R	R
N-SP0.125-1	17.4	2.32	C	C
N-SP0.125-2	16.7	2.10	C	C
N-SP0.25-1	17.0	2.02	C	C
N-SP0.25-2	14.9	1.48	C	C
N-SP0.5-1	17.3	1.91	C	C
N-SP0.5-2	17.9	2.07	C	R

[a] Second specimen was damaged during fabrication. A = adhesion failure between steel and adhesive; C = cohesive failure; D = carbon fiber reinforced polymer delamination; R = carbon fiber reinforced polymer rupture; — indicates no value because failure was exclusively rupture.

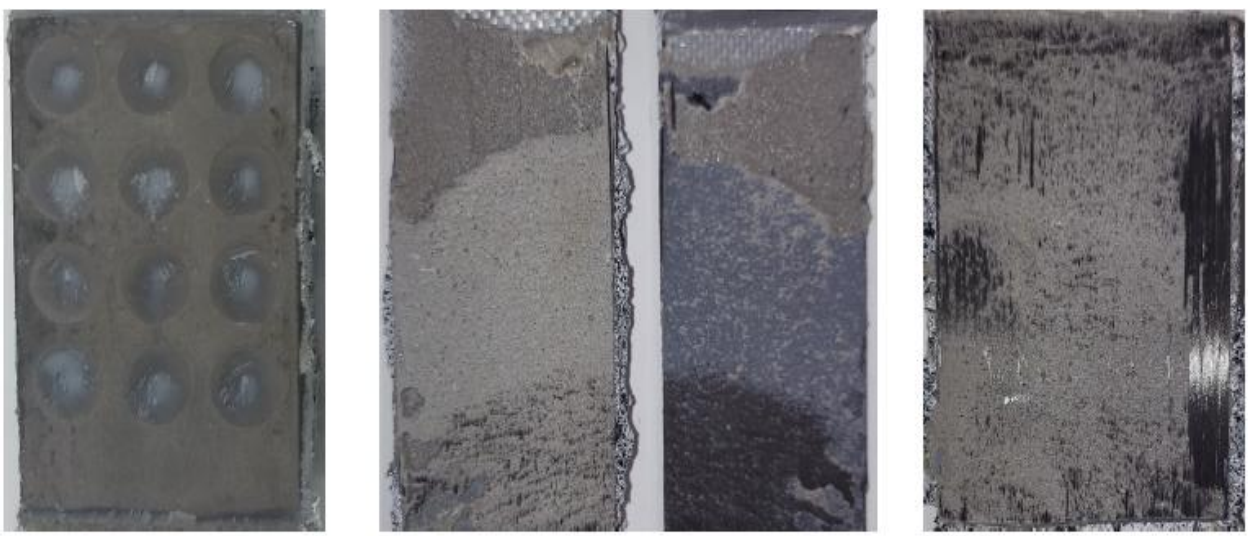

(a) (b) (c)

Figure 101. Typical Failure Modes of Specimens Fabricated with the Normal Modulus Carbon Fiber Reinforced Polymer Plate: (a) Adhesion Failure between Steel and Adhesive; (b) Cohesive Failure; (c) Combination of Cohesive Failure and Delamination

Figure 12 shows the failure modes for joints strengthened with a UHM strand sheet. For specimens with machined pits up to $\frac{1}{16}$ inch in diameter, the failure mode was primarily rupture, which is a common failure mode for UHM CFRP laminates (Zhao and Zhang, 2007). Specimens with larger-diameter pits failed predominantly cohesively in nature, as Table 2 shows. Thus, the presence of larger-sized surface pits on the steel plate appears to moderately affect the failure mode and, ultimately, the failure load.

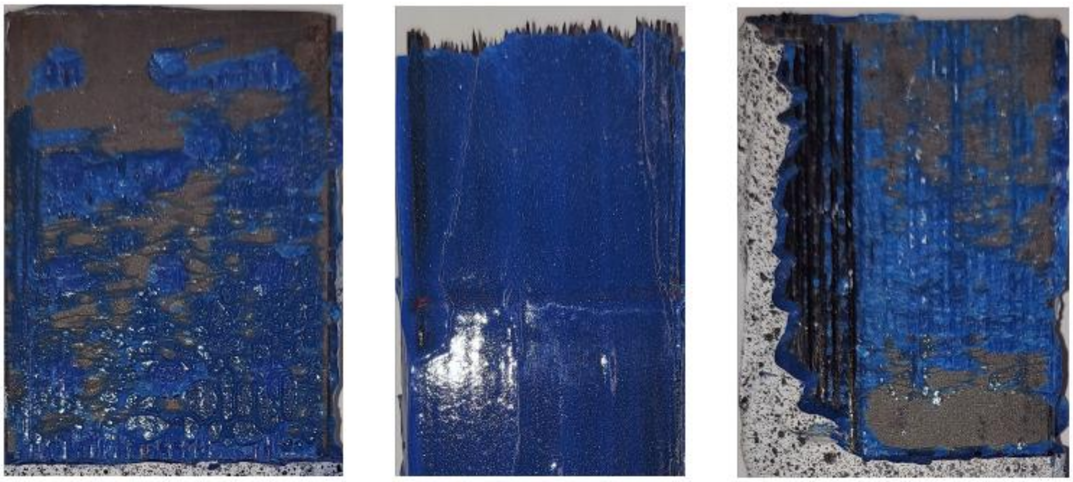

(a) (b) (c)

Figure 112. Typical Failure Modes of Specimens Fabricated with Ultra-High Modulus Strengthening Materials: (a) Cohesive Failure; (b) CFRP Rupture; (c) Combination of Adhesion Failure—Cohesive Failure and CFRP Rupture. CFRP = carbon fiber reinforced polymer.

Effect of Surface Pits on the Ultimate Load

Figure 123a shows the influence of surface roughness on the average ultimate tensile load of NM joints, normalized against the strength of smooth specimens. All the tested specimens, except for one, reported greater capacity than the reference smooth specimens. Figure 123 indicated that at lower surface roughness levels, the ultimate load remained relatively constant as R_a, R_q, and R_z increased. As the roughness continued to increase, the tensile capacity reached a peak value at a pit diameter of 0.25 inch and then decreased. The maximum load attained corresponded to a 13% increase in tensile capacity over the control specimens. These results indicate no adverse effect on the tensile capacity due to increased surface roughness and that a certain degree of surface irregularity may provide the maximum reinforcement to the bond capacity.

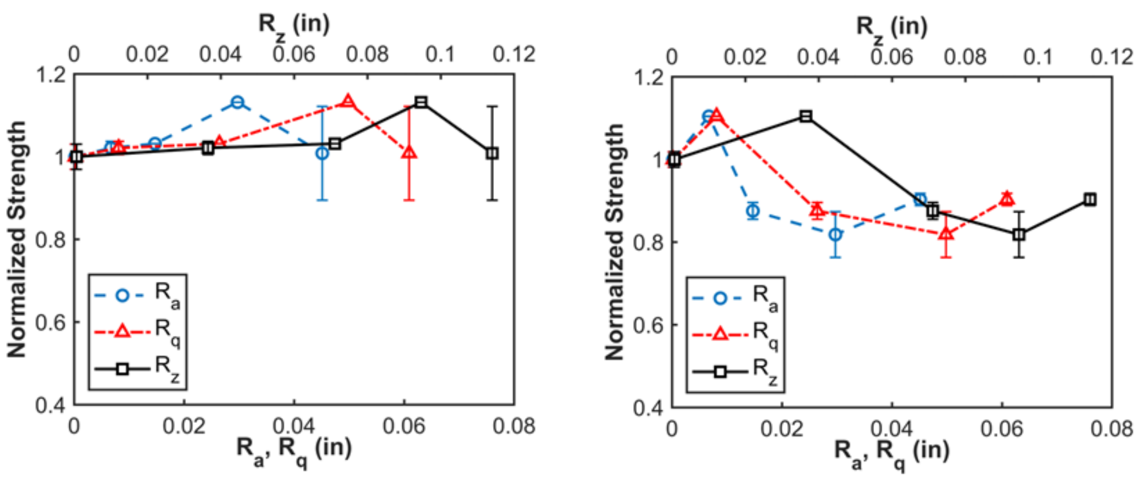

(a) (b)

Figure 123. Influence of the Roughness Parameters on the Tensile Capacity of (a) Normal Modulus Double-Strap Joints and (b) Ultra-High Modulus Double-Strap Joints. R_a = average roughness parameter; R_q = root-mean-square roughness parameter; R_z = average maximum height parameter.

Comparison of Theoretical Versus Experimental Failure Loads

An engineer can predict the ultimate load by substituting into Equations 12 through 14 the respective material properties and the calculated G_f. Tables 3 and 4 list the ratio of the predicted load, $P_{u,pred}$, versus experimental ultimate load, $P_{u,exp}$, for the NM and UHM CFRP strengthening systems, respectively. **Error! Reference source not found.**4 also illustrates these results, indicating that Equations 12 through 14 predicted the capacity of double-strap specimens strengthened with NM materials within 12%, 7%, and 25%, respectively, of their actual capacity. Note that Hart-Smith's (1973) strength-based approach (Equation 14) consistently underpredicted the load by a larger margin because that equation assumed the ultimate bond strength was reached when the adhesive first cracked, which did not reflect the complete debonding of CFRP-steel joints (Teng et al., 2012). Equation 12 also underpredicted the failure load because the stiffness ratio, δ, was not considered. On the other hand, Wu et al.'s (2002) Equation 13 slightly overestimated the strength of the UHM joint. Thus, taking the stiffness ratio into consideration can lead to overestimating the load capacity of UHM-strengthened joints by 33% on average. While still having the potential of being unconservative, Wu et al.'s (2002) Equation 12 provided the most accurate predictions for UHM joints, with a mean ratio between the predicted and experimental ultimate strength being 1.01.

Corrosion

Both types of CFRP in this study exhibited good bond properties with the corroded specimens, with cohesion being the predominant failure mode. On the other hand, the degree of corrosion had opposite effects in terms of bond strength for the two different materials.

Table 3. Ratio of Theoretical ($P_{u,Pre}$) Versus Experimental ($P_{u,Exp}$) Ultimate Load for the Normal Modulus Specimens

Specimen	Eq. (12)	Eq. (13)	Eq. (14)
S-SP0-1	0.89	0.98	1.12
S-SP0-2	0.94	1.03	1.04
S-SP0.0625-1	0.91	1.00	0.80
S-SP0.0625-2	0.92	1.00	0.90
S-SP0.125-1	0.98	1.07	0.86
S-SP0.125-2	—	—	—
S-SP0.25-1	0.94	1.03	0.83
S-SP0.25-2	—	—	—
S-SP0.5-1	0.95	1.04	0.82
S-SP0.5-2	0.90	0.98	0.81
Mean	0.93	1.02	0.90
Standard Deviation	0.030	0.032	0.120
Coefficient of Variation (%)	3.19	3.19	13.4
Minimum	0.89	0.98	0.80
Maximum	0.98	1.07	1.12

— indicates specimen was damaged during fabrication.

Table 4. Ratio of Theoretical ($P_{u,Pre}$) Versus Experimental ($P_{u,Exp}$) Ultimate Load for the Ultra-High Modulus Specimens

Specimen	Eq. (12)	Eq. (13)
N-SP0-1	1.05	1.38
N-SP0-2	—	—
N-SP0.0625-1	—	—
N-SP0.0625-2	—	—
N-SP0.125-1	1.05	1.39
N-SP0.125-2	1.05	1.38
N-SP0.25-1	1.01	1.33
N-SP0.25-2	0.99	1.30
N-SP0.5-1	0.96	1.27
N-SP0.5-2	0.97	1.28
Mean	1.01	1.33
Standard Deviation	0.039	0.051
Coefficient of Variation (%)	3.82	3.82
Minimum	0.96	1.27
Maximum	1.05	1.39

— indicates no calculation of $P_{u,Pre}$ because of rupture failure.

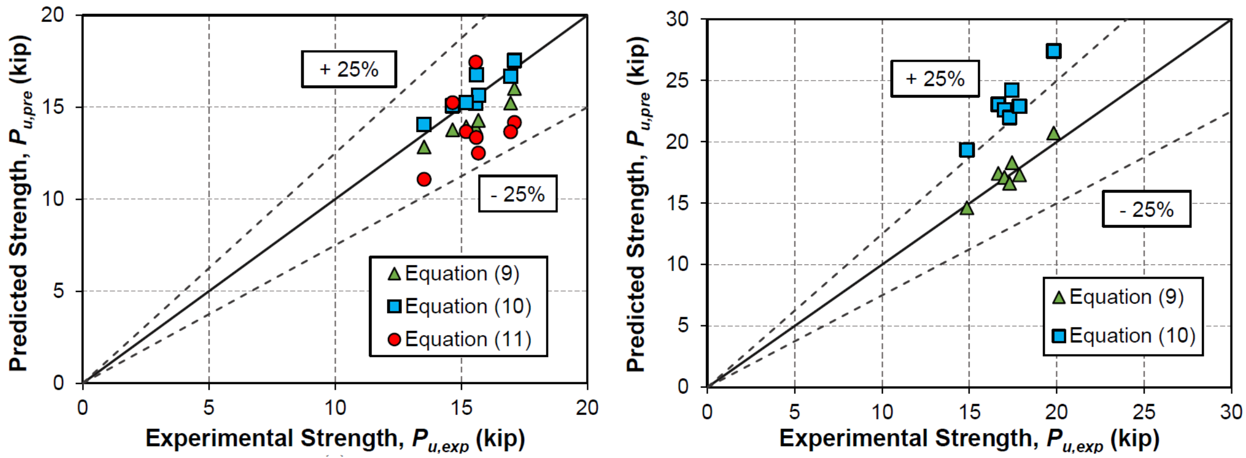

(a) (b)

Figure 134. Comparison Between Analytical and Experimental Results for Double-Strap Joints Strengthened with (a) Normal Modulus and (b) Ultra-High Modulus Strengthening Materials

Surface Characteristics: Roughness Parameters

For all the corrosion specimens, one face of the corroded bars was rougher in texture than the other. This observation was particularly true for corrosion level 4. Figure 145 shows thevariation of surface roughness with increasing corrosion severity. The error bars in the plot indicate the variation of the results for four corroded bars with the same level of deterioration. As anticipated, the surface roughness characteristics increased with corrosion severity. The amplitude parameters S_a and S_z reached a maximum value of 0.0144 inch and 0.106 inch, respectively, and the hybrid parameter S_{dr} attained a maximum value of 0.569%.

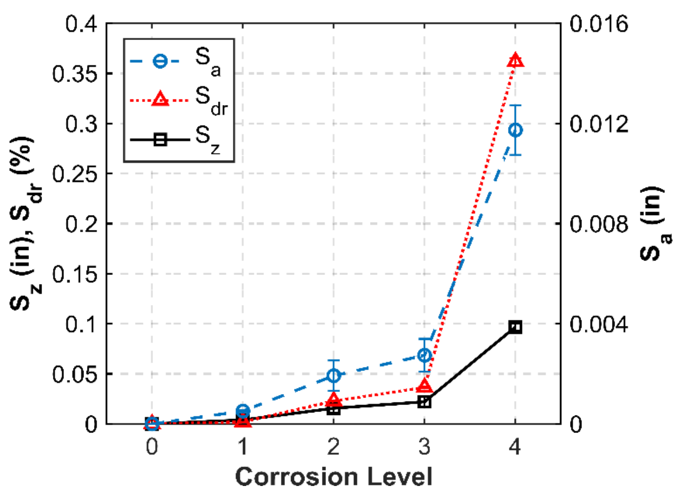

Figure 145. Variation of Surface Roughness Parameters with Increasing Corrosion Severity. S_a = average surface height; S_z = maximum surface height; S_{dr} = interfacial area ratio.

Failure Modes

Table 5 presents the ultimate tensile load and corresponding failure modes of all corrosion specimens. In addition, Figure 156 presents the failure modes for NM double-strap specimens. As Table 5 indicates, the additional roughness due to corrosion did not change the failure mode, with the predominant mode being a combination of cohesion failure and delamination.

Table 5. Experimental Results of Double-Strap Joints Fabricated with Corroded Bars

Specimen	P_u (kip)	G_f (lb/in)	τ_{max} (ksi)	Failure Mode	
				Side A	Side B
S-CL0-1	15.6	4.18	2.73	C/D	C/D
S-CL0-2	14.7	4.11	2.38	C/D	C
S-CL1-1	15.4	4.01	1.93	C/D	A
S-CL1-2	14.2	3.42	1.90	A	C/D
S-CL2-1	17.0	5.14	2.39	C/D	C/D
S-CL2-2	18.5	5.48	2.96	C/D	C/D
S-CL3-1	16.7	5.14	2.45	C/D	C/D
S-CL3-2	15.8	4.66	2.12	C/D	D
S-CL4-1	9.3	1.69	1.39	C/D	A
S-CL4-2	14.2	3.41	2.06	C/D	A
N-CL0-1	19.8	2.97	6.29	C/R	C/R
N-CL0-2	19.1	—	—	R	R
N-CL1-1	11.3	0.96	2.76	C	C
N-CL1-2	17.6	2.21	4.48	C	C
N-CL2-1	14.7	1.74	3.50	C/R	C
N-CL2-2	10.8	0.95	2.86	C	C
N-CL3-1	15.8	1.79	4.31	C	C
N-CL3-2	14.4	1.42	3.19	C/R	C
N-CL4-1	15.6	1.67	5.24	R	C
N-CL4-2	12.1	1.01	3.54	C	C

A = adhesion failure between steel and adhesive; C = cohesive failure; D = delamination of carbon fiber reinforced polymer; R = rupture of carbon fiber reinforced polymer. — indicates no value because failure was exclusively rupture.

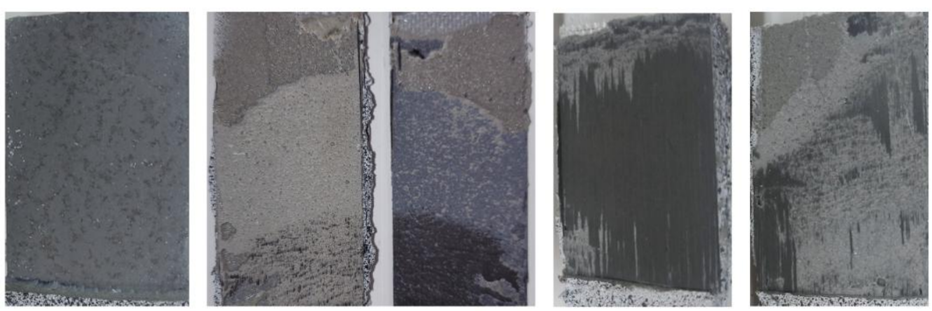

(a) (b) (c) (d)

Figure 156. Failure Modes of Normal Modulus Specimens: (a) Adhesion Failure between Steel and Adhesive; (b) Cohesive Failure; (c) Plate Delamination; (d) Combination of Cohesive Failure and Delamination

A few cases of adhesion failure occurred between the steel plate and the adhesive, which indicated insufficient surface preparation. Nonetheless, inadequate adhesion did not significantly affect the tensile strength of the joints, except for specimen S-CL4-1, which retained only 62% of the capacity of specimens with a smooth surface condition. This poor result was associated with heavy deterioration from substantial layered corrosion, which was more difficult to remove.

The failure modes for joints strengthened with a UHM strand sheet were the same as those in Figure 112. It is evident from Table 5 that the recurrent failure mode was cohesive failure, with occasional instances of CFRP rupture or a combination of cohesive failure and

CFRP rupture. The asymmetry of failure modes noted in specimens N-CL2-1, N-CL3-2, and N-CL4-1 may be attributed to the corrosion-induced higher surface roughness on side A. Contrary to the simulated corrosion pitting results in Table 2, Table 5 does not suggest that the failure mode affected the joint strength. Note that no adhesion failures occurred for the UHM corrosion specimens. This observation signifies the adhesive's strong capacity to bond with corroded steel and CFRP strand sheet surfaces.

Corrosion Effects on Ultimate Load

7a demonstrates the influence of the surface roughness parameters on the ultimate tensile load, normalized with respect to the strength of smooth specimens. Scatter in the data is due to uneven corrosion texture on the interface and differences in surface topography among the two faces of the corroded bars. In general, the roughness due to corrosion provided a positive effect on the tensile capacity of the joint (up to 22% increase in strength). Three specimens reported lower strengths, two of which had a strength that was only 6% less than the control specimen. Note that the ultimate load of the Level 4 corrosion specimens is less than the strength of the smooth specimens. Furthermore, the specimen with greatest surface roughness caused by corrosion led to a 37% reduction in tensile strength.

7b presents the influence of the surface texture parameters on the ultimate load for specimens fabricated with a UHM strand sheet. The ultimate load of uncorroded specimens was greater than that of any corroded specimen, indicating a negative effect of corrosion on the ultimate tensile strength for steel bonded to this type of CFRP system. Similarly, scatter in the tensile capacity is a consequence of the uneven corrosion texture on the interface and the difference in surface topography, where no two bars were identical. Although no obvious relationship was determined between the ultimate load and an increase in surface roughness, the findings highlight the importance of considering the behavior of different CFRP materials for the implantation of bridge retrofits.

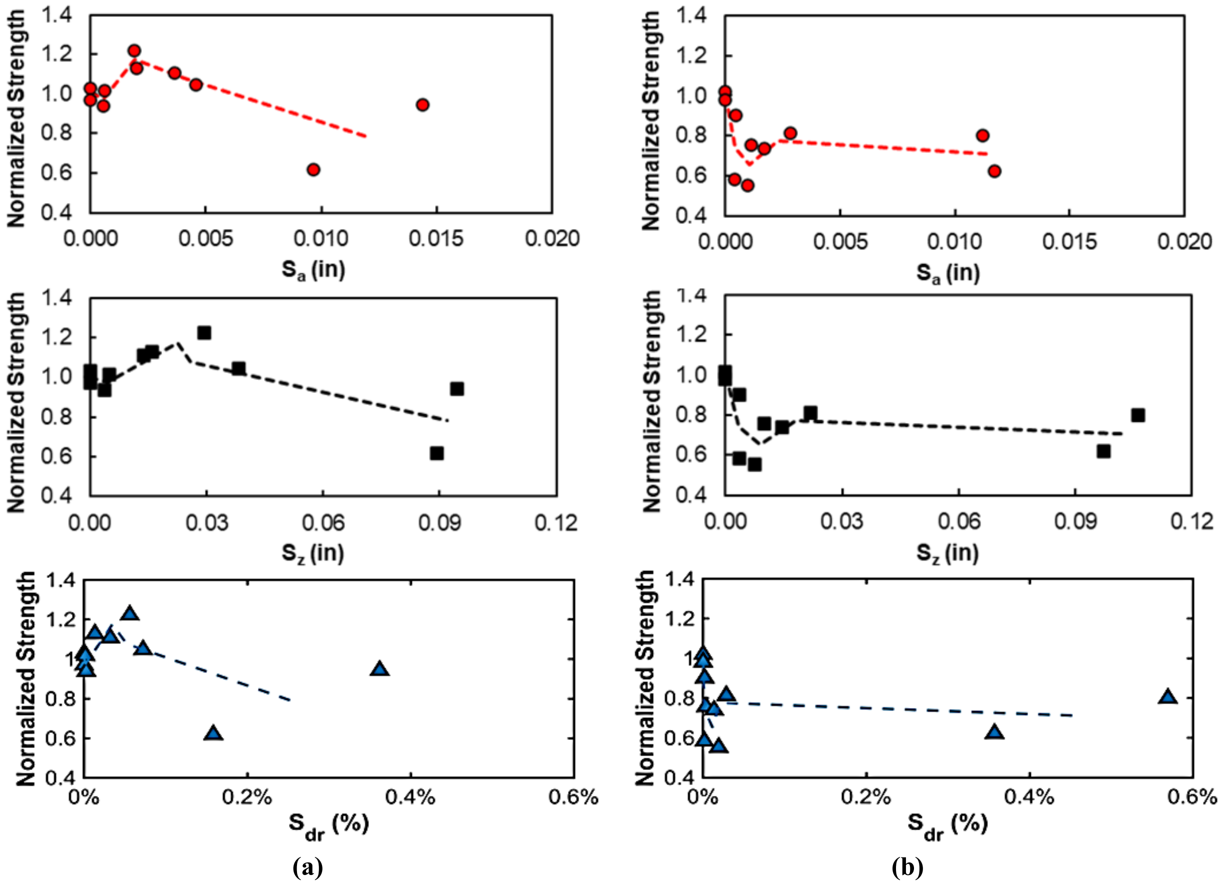

Figure 167. Influence of S_a, S_z, and S_{dr} on the Tensile Capacity of Double-Strap Joints Fabricated with Corroded Steel Bars with (a) Normal Modulus and (b) Ultra-High Modulus Strengthening Components

Effective Bond Length

The effective bond length, L_{eff}, for joints whose bond-slip model has linearly ascending and descending branches can be approximated by the following analytical expression (Yuan et al., 2004):

$$L_{eff} = \frac{\pi}{2\sqrt{\frac{\tau}{E_f t_f s_f}}} \quad \text{(Equation 20)}$$

Figure 178 presents the effects of corrosion on L_{eff} for the two composite materials. L_{eff} was greater for corroded specimens compared with uncorroded samples, which suggests corrosion-induced deterioration in the load transfer efficiency. The one exception to this observation was for UHM joints with excessive corrosion (corrosion level 4), although the reason for this outlier was unknown.

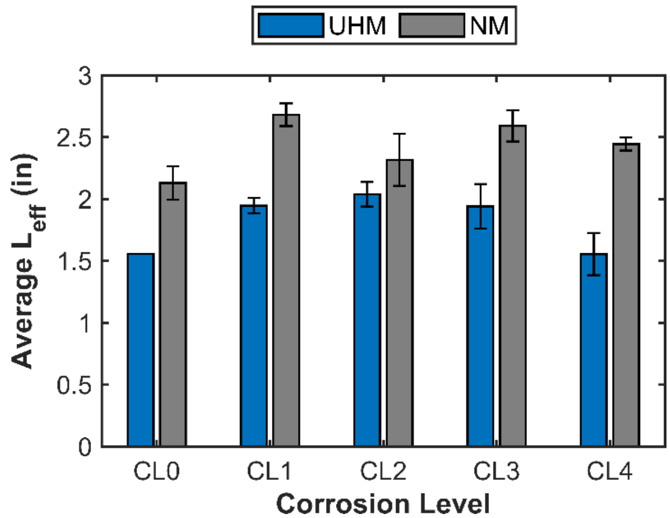

Figure 178. Effect of Corrosion on the Effective Bond Length of Double-Strap Joints Strengthened with a NM Plate and a UHM Strand Sheet. CL = corrosion level; NM = normal modulus; UHM = ultra-high modulus.

Proposed Bond-Strength Model

As discussed previously, the coefficients *A*, *B*, and *C* in Equation 18 were optimized to minimize the error between the theoretical predictions and the experimental results, yielding the following expression:

$$G_f = \frac{5.35(t_a R)^{0.35}}{K_f^{0.88}} \cdot 10^6 \left(\frac{\text{lb}}{\text{in}}\right) \qquad \text{(Equation 21)}$$

The applicability of the proposed model was validated against a database of existing studies consisting of 82 experimental results (Chotickai, 2018; Li et al., 2019; Phan et al., 2015; Xu et al., 2020), which satisfied the following criteria: (1) the steel substrate had a degree of surface roughness because of either natural or laboratory corrosion, simulated pitting, or grinding; (2) the failure mode was either cohesive or adhesive; and (3) the bond length was greater than the effective bond length.

Table A1 details the predicted results of the interfacial fracture energy from Equation 18. In Table A1, $G_{f,pred}$ and $G_{f,exp}$ are the predicted and experimental interfacial fracture energy, respectively, and $P_{u,pred}$ and $P_{u,exp}$ are the respective predicted and experimental ultimate load. The ratios between the predicted and experimental results have a mean value of 1.08 and a coefficient of variation of 0.38. Figure 19 plots these comparisons. The 0.93 coefficient of determination in Figure 19 shows that the proposed expression for the interfacial fracture energy is reasonable for the tests given in the database.

The ultimate loads of the specimens in the database can be predicted with either Equation 12 or 13, using the predicted value of G_f from Equation 18. The ratio of the predicted versus experimental capacities is listed in Table A1 and plotted in Figure 180a. To improve the predictive performance of the model, the researchers removed any outliers by calculating the standardized residuals, which equaled the value of the residual (defined as the difference between the predicted and experimental values) divided by an estimate of the standard deviation. Standardized residuals greater than 2 or less than -2 are often considered outliers. Five data points that exceeded these bounds were identified as outliers, as Figure 20b shows, and removed from the fitting in Figure 20b. The ratios between the predicted ultimate load and the experimental test results had a mean value of 1.01, a coefficient of variation of 0.17, and a coefficient of determination of 0.81. These statistics suggest that the proposed empirical model provides suitable predictions for the load capacity of CFRP-steel joints with corrosion-roughened surfaces.

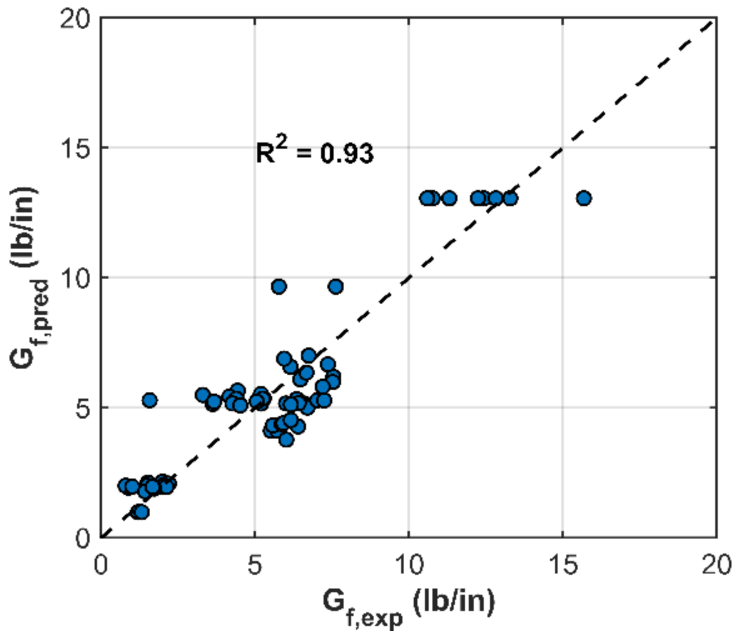

Figure 19. Comparison Between the Predicted and Experimental Interfacial Fracture Energy

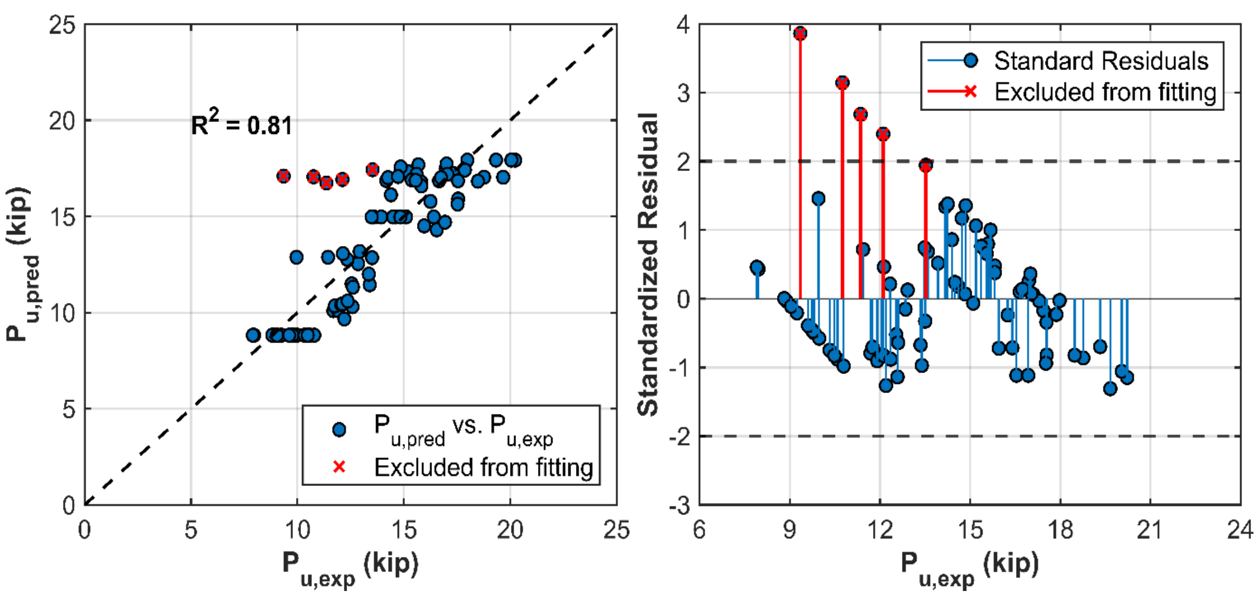

Figure 180. (a) Comparison Between the Predicted and Experimental Ultimate Load and (b) Standardized Residuals of Predicted Ultimate Load

Laboratory Environmental Aging

Hygrothermal Cycles

After cyclic exposure to different heat and moisture regimens, the two CFRP types had differences in primary failure modes and bond strength at the steel-adhesive interface relative to the control specimens.

Failure Modes

The observed failure modes for the NM specimens are presented in Figure 191 and summarized in Table A2. The predominant mode of failure for the conditioned specimens was a combination of cohesive failure and delamination. The triggering failure mode of the unconditioned specimens was also a mixture of cohesive failure and delamination, indicating the modes of failure had no significant differences. Cohesive failures are more desirable because the energy dissipation and ductility are maximal and indicate a good bond at the steel-adhesive interface (Heshmati et al., 2016). The delamination in the conditioned specimens primarily occurred at the end of the CFRP, where peel stresses were the greatest.

(a) (b) (c) (d) (e)

Figure 191. Failure Modes of Specimens Fabricated with the Normal Modulus Carbon Fiber Reinforced Polymer Plate: (a) Adhesion Failure Between Adhesive and Glass Fiber Reinforced Polymer Plate; (b) Cohesive Failure; (c) Plate Delamination; (d) Combined Adhesion and Delamination; (e) Combined Cohesive Failure and Delamination

The NM specimens subjected to condition A in Figure 5 did not exhibit any corrosion. On the other hand, joints that were exposed to either conditions B or C did exhibit minor corrosion after 8 and 4 weeks of exposure to conditions B and C, respectively. After an additional 4 weeks, the condition C specimens had more extensive corrosion on the steel near the ends of the CFRP. However, post-failure visual inspection revealed no corrosion within the bonded area. This observation suggests that the hygrothermal conditioning did not degrade the steel-adhesive interface and, consequently, the failure of the joint was cohesive in nature.

Figure 202 demonstrates the failure modes for UHM CFRP-steel joints. The mode of failure of the two unexposed specimens was CFRP rupture on one face of the joint and cohesive failure on the other. As the exposure time progressed, the failure mode transitioned to a mixture of CFRP rupture and cohesive failure on a given face or strictly CFRP rupture for both faces. These UHM joints had similar corrosion conditions as the NM specimens, regardless of conditioning scenario. Furthermore, no discoloration of the CFRP-adhesive surface was present.

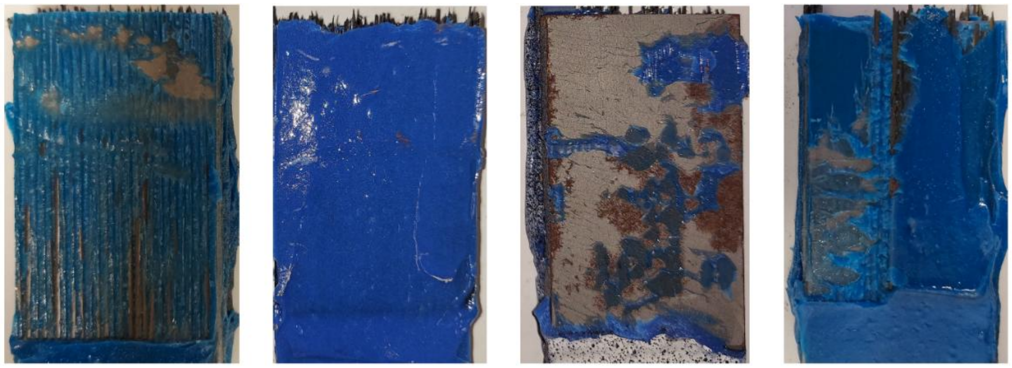

(a) (b) (c) (d)

Figure 202. Failure Modes of Specimens Strengthened with an Ultra-High Modulus Strand Sheet: (a) Cohesive Failure; (b) CFRP Rupture; (c) Combination of Adhesion Failure at the Steel-Adhesive Interface and Cohesive Failure; (d) Combined Adhesion Failure and CFRP Rupture. CFRP = carbon fiber reinforced polymer.

Only one specimen exhibited a small amount of corrosion on the steel surface within the bonded area at 7 weeks of exposure (Figure 202c), where the triggering failure mode was at the steel-adhesive interface. In general, the hygrothermal conditions in this study did not affect the bond at the steel-adhesive interface, and the failure of the joint was dictated by the failure within either the CFRP or adhesive layers.

Joint Strength

Figure 213a presents the joint strength degradation of NM specimens exposed to the hygrothermal conditions. The joint specimens exposed to 8 weeks of conditions A and B gained a negligible amount of strength (about 3%) compared with the control conditions. This result suggests that a moderate degree of relative humidity and temperatures seen across much of Virginia can potentially benefit the bond strength between steel and NM CFRP. Note that the joint strength did decrease minimally before improving beyond the baseline values.

Adhesively bonded joints have been shown to withstand exposure to relative humidity less than 50% for an extended period without significant degradation (Comyn et al., 1987). Gledhill et al. (1980) revealed that a critical moisture concentration of 1.35% in the adhesive layer caused weakening of steel-epoxy joints. Similarly, Brewis et al. (1990) determined this critical concentration to be 1.45% in aluminum-epoxy joints. Furthermore, the Brewis et al. (1990) study found that joints exposed to 122°F and relative humidity ranging from 23% to 100% did not have any deterioration after 192, 504, and 1,008 hours of exposure because the critical level of water concentration in the adhesive layer was not achieved. Even after 420 days of aging at a relative humidity below 42%, the moisture concentration was below the critical level for initiating damage. Therefore, the 8-week schedule that this portion of the study was allotted may have been insufficient to achieve the critical moisture content in the adhesive under conditions A and B.

On the other hand, the strength of specimens exposed to condition C decreased by 27.7% after 4 weeks of hygrothermal cycling. However, the joint strength recovered nearly 74% of that degradation during the next 4 weeks, resulting in only a 7% strength reduction after 8 weeks.

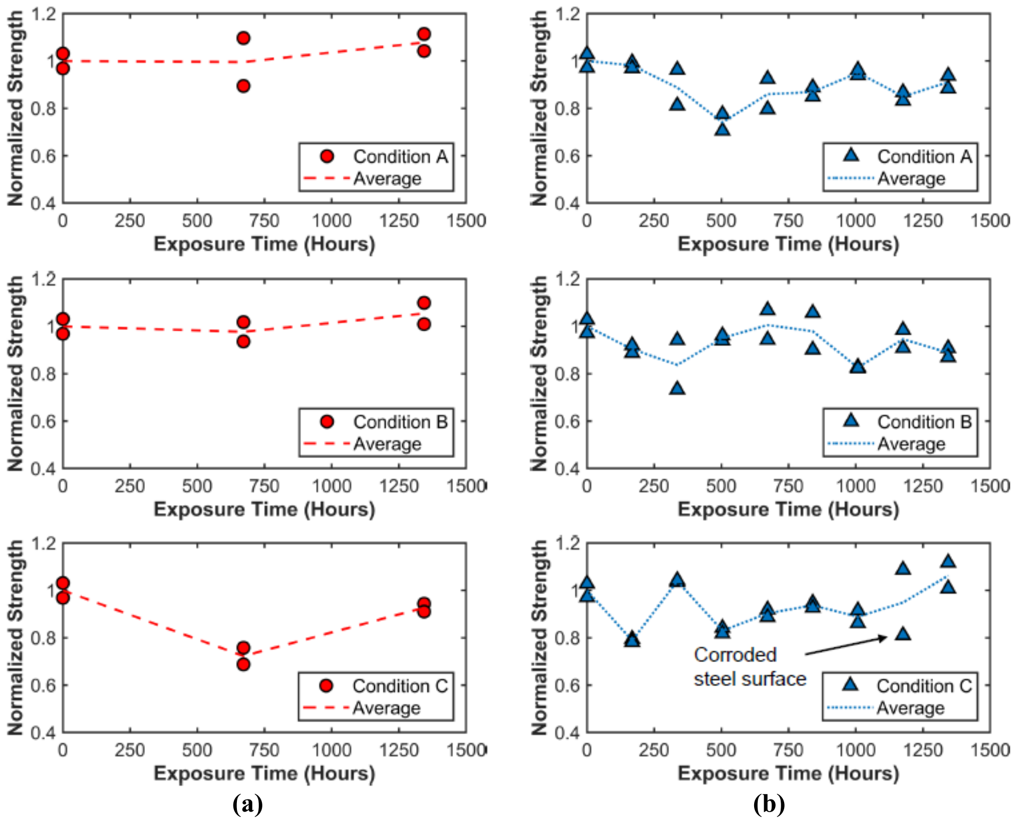

Figure 213. Influence of Hygrothermal Aging on the Average Joint Strength of Double-Strap Joints Strengthened with a: (a) Normal Modulus Plate and (b) Ultra-High Modulus Strand Sheet

This phenomenon can be explained by the counteracting effects of moisture and temperature, where elevated temperatures can slow down moisture penetration into the joint by further diffusing any moisture present (Bai et al., 2014; Yang et al., 2005). Furthermore, higher temperatures can provide post-curing benefits for the adhesive, resulting in strength improvements (Bai et al., 2014), whereas the differences in the coefficients of thermal expansion between the steel, adhesive, and CFRP may result in thermal stresses that can adversely affect the bond strength between CFRP and steel (Yang et al., 2005). Previous work on bonded aluminum joints has demonstrated that drying the joints after exposure to high humidity can lead to partial strength recovery (Comyn et al., 1987; Mubashar et al., 2009). The authors attributed the strength recovery to the reversible plasticization effect. As a result, the bond strength can decrease and increase throughout the aging process, thus limiting the damage that could occur.

Similar to the NM joints, Figure 213b demonstrates the effects of hygrothermal aging on the bond strength of UHM double-strap joints, on which all three exposure conditions had similar trends. That is, the bond strength had two cycles of decreasing and increasing values as the aging time progressed due to the opposing effects of moisture and temperature changes. An interesting observation is that the bond strength of specimens exposed to condition A was consistently less than that of the unexposed specimens, regardless of the exposure duration. The same was largely true for specimens aged under condition B, except at 4 weeks, for which the average bond strength was marginally greater than the control. The observed reduction in bond strength for conditions A and B varied from about 2% to 26% and from 2% to 17%, respectively. As previously mentioned, low relative humidity levels and limited exposure time to achieve the critical moisture content were unlikely to result in moisture-induced damage. Thus, the noted bond degradation can be a result of other factors.

Condition C resulted in up to 21% bond strength degradation but also finished with a 6% increase in capacity at the completion of the hygrothermal aging cycles, or after 8 weeks. Note that the 18% reduction in joint capacity after 7 weeks of aging was due to the presence of corrosion on the steel surface of one specimen, which shifted the mode of failure to adhesion at the steel-adhesive interface. A closer examination of Figure 213b reveals a general increase in bond strength from 3 to 8 weeks of aging. The findings imply that the thermal cyclic program from 68 to 122°F could induce more significant degradation at the early stages of exposure, after which the joint regained some of its bond strength.

Combined Effects of Surface Condition and Hygrothermal Cycles

The combined effects of surface condition and hygrothermal aging on the bond strength of UHM double-strap joints are demonstrated in

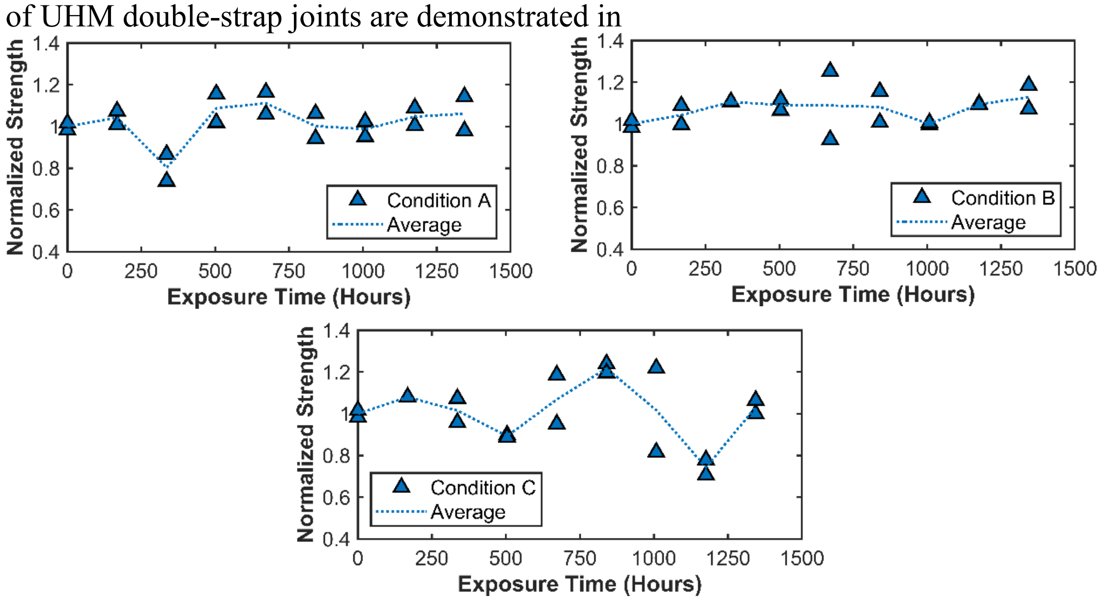

Figure 224 and tabulated in Table A4. The failure modes were the same as those noted in Figure 202a and 22b, with CFRP rupture being the prevalent mode of failure. Similarly, the strength varied widely throughout the exposure period, particularly for conditions A and C. For condition B, the strength was generally greater than the unaged conditions, but one specimen had 8% less capacity after 4 weeks of aging. The observed reduction in bond strength for conditions A and C varied from 1% to 20% and from 11% to 26%, respectively. However, significant reductions in bond strength were limited to a few specimens. In general, no substantial degradation in the bond strength due to the conditions examined was observed.

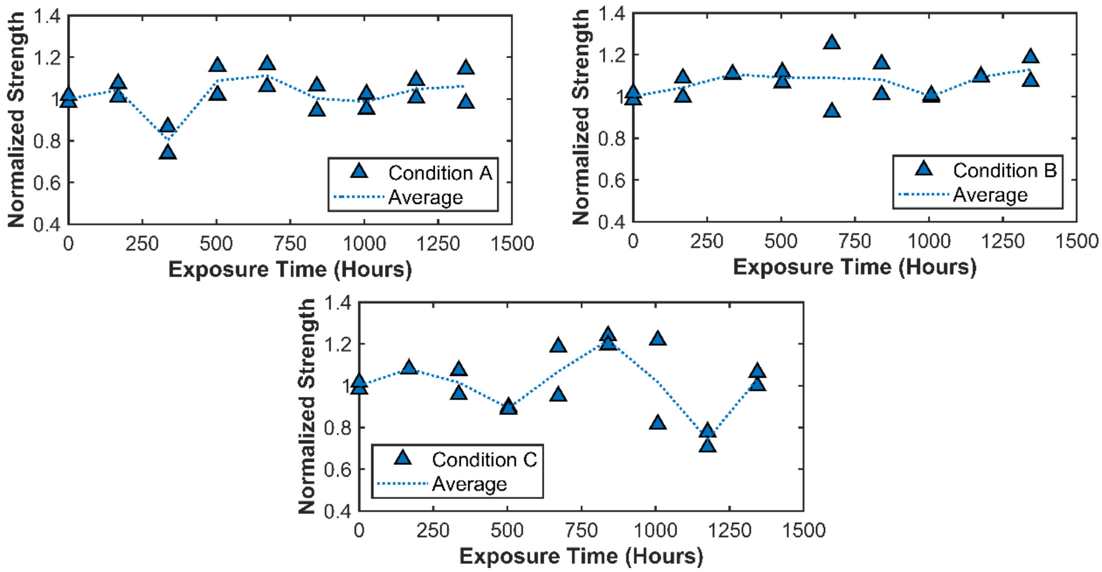

Figure 224. Influence of Surface Condition and Hygrothermal Aging on the Average Joint Strength of Double-Strap Joints Strengthened with an Ultra-High Modulus Strand Sheet

Proposed Strength Reduction Factors

The results revealed limited damage accumulation and some strength recovery or even enhancement after exposure to the hygrothermal conditions studied in this research. These contradicting facts add to the complexity of predicting the bond strength after long-term environmental conditioning. Nevertheless, a recommended strength reduction factor, α_{HT}, exists for estimating the residual strength of CFRP-steel systems after hygrothermal aging under certain conditions (Table 6). Herein, α_{HT} describes the ratio of the aged bond strength to that of the unexposed scenario. The strength reduction factor, α_{HT}, for the UHM specimens was determined by taking two standard deviations below the average ratio of the aged to unaged bond strength for each hygrothermal condition. Ideally, the same approach would have applied to the NM specimens. However, because only a limited number of NM specimens were available for each hygrothermal condition, the lower experimental α_{HT} value is a conservative result for each NM scenario in Table 6.

Table 6. Proposed Values for the Strength Reduction Factor, α_{HT}

Condition	CFRP Material		
	NM Plate	UHM Strand Sheet	UHM Strand Sheet with Pits
Reference	1.00	1.00	1.00
A (39–104°F, 30% RH)	1.00	0.74	0.82
B (23–104°F, 75% RH)	1.00	0.80	1.00
C (68–122°F, 90% RH)	0.72	0.74	0.73

CFRP = carbon fiber reinforced polymer; NM = normal modulus; RH = relative humidity; UHM = ultra-high modulus.

Hygrothermal conditions A and B required negligible strength reduction, and in fact, appeared to be beneficial to the bond strength of joints reinforced with an NM plate. Subsequently, no reduction factor is required for those two conditions. On the other hand, condition C represented a more hostile environment. Thus, a 0.72 reduction factor is warranted. Looking solely at the UHM-steel joints, a strength reduction would be prudent for all three hygrothermal conditioning scenarios, given that the bond strength of these specimens was generally less than that of the unconditioned control specimens.

Chloride Exposure Cycles

Generally, exposing the UHM CFRP specimens to different levels of chlorides did not affect the bond performance between corroded steel and CFRP.

Failure Modes

The failure modes for the chloride exposure samples were similar to those in Figures 101, 112, 156, 191, and 202, with a few additional combinations of failure modes, as Tables A5 through A7 indicate and Figures 25 and 26 show. Chloride exposure did not change the primary failure modes for the NM specimens. However, relative to the unexposed NM specimens, the exposed specimens did have more localized areas of adhesion failure between the adhesive and the GFRP layer, as well as corroded steel. This observation could mean that the steel and adhesive adjacent to the GFRP insulation layer may experience higher rates of debonding from the GFRP the longer the time in service continues. However, what is not clear is why the bond to the GFRP deteriorated more for the simulated rural and marine environments but not for the heavy deicing salt environment. One additional observation is that the failures in the conditioned specimens were slightly more prone to occur on the segment of the joint with the longer bond region. These failures in the longer bond region were not necessarily related to the installation because all four of these specimens failed, at least in part, due to CFRP delamination; one of these specimens did not even involve adhesion failure.

(a) (b) (c)

Figure 25. Additional Failure Modes for Double-Strap Joints Strengthened with Normal Modulus CFRP Plate and Subjected to Chlorides: (a) Combination of CFRP Delamination, Adhesion Between the Adhesive and Both the CFRP and GFRP Insulating Mat, and Cohesion; (b) Combination of Adhesion Between the Adhesive and Both the GFRP Insulating Layer and CFRP, and Delamination; (c) Combination of Cohesion, CFRP Delamination, and Steel Oxidation. CFRP = carbon fiber reinforced polymer; GFRP = glass fiber reinforced polymer.

Figure 26. Additional Observed Failure Modes for Double-Strap Joints Strengthened with Ultra-High Modulus Strand Sheets and Subjected to Chlorides: (a) Combination of CFRP Rupture, Adhesion at the Steel-Adhesive Interface, and Steel Oxidation; (b) Combination of CFRP Rupture, Adhesion at the Steel-Adhesive Interface and at the Adhesive-CFRP Interface, Cohesion, and Delamination; (c) Combination of Adhesion at Both the Steel-Adhesive Interface and the Adhesive-CFRP Interface, and Cohesion; (d) Combination of Adhesion at Both the Steel-Adhesive Interface and the Adhesive-CFRP Interface, Cohesion Within the Primer, and Steel Oxidation. CFRP = carbon fiber reinforced polymer.

For the UHM specimens, CFRP rupture was the overwhelming failure mode for all three chloride exposure levels. However, scattered cases in which rupture combined with other failure modes occurred, often either adhesion between the adhesive and the CFRP or cohesive failures, or both adhesive and cohesive failures. Like the NM specimens, conditioned UHM specimens did have a greater propensity for failure between the primer and the steel, as well as steel corrosion. Two UHM specimens subjected to chloride levels simulating a rural environment showed cohesive failure within the primer layer. Overall, however, the pattern was not consistent for when the dominant failure mode varied from CFRP rupture.

Joint Strength

Figure 27 compares the ultimate load and strains in the chloride exposure specimens following up to 8 weeks of conditioning under the three levels of chloride concentration. Of the six load curves in Figure 27, only the smooth specimens strengthened with the UHM CFRP and subjected to marine chloride levels had any statistically significant change in bond capacity after 8 weeks of exposure. This change in capacity is readily apparent in the drop in ultimate load at week 7 in Figure 27b. Note that adhesion failure between the primer and the smooth steel surface was the dominant mode of failure in the week 7 and 8 specimens, whereas the specimens conditioned for shorter durations failed solely or primarily by CFRP rupture. The reason may be that the researchers made these four specimens in the same batch but separate from the other specimens. If the assumption is that the week 7 and 8 UHM CFRP smooth specimens that were subjected to a simulated marine environment were outliers due to adhesive batching, then no statistically significant difference would occur between the remaining conditioned and unconditioned specimens in this scenario. In this case, the strength reduction factor due to chloride exposure, α_{Cl}, is 1.0. Future testing with additional samples may help clarify whether the data in this study suggest that outliers or a definitive trend occur as the conditioning duration progresses. With that said, these potential outliers highlight the importance of proper adhesive mixing and overall CFRP installation.

On a separate note, the corrosion observed on the week 7 and 8 specimens with initial simulated pitting and subjected to rural chloride levels did not have a statistically significant impact on the bond strength of those specimens. The same was true for the two specimens that failed in cohesion within the primer layer.

Despite the aforementioned dramatic drop in Figure 27b, analysis indicated that the bond strength between the smooth and pitted specimens conditioned in a simulated marine environment were statistically equivalent. The same was true for those specimens tested in the rural chloride environment. On the other hand, similar analysis revealed that the two types of steel surfaces bonded to the UHM material did have different levels of performance after being exposed to concentrations of heavy deicing salts in the test chamber for longer than 3 weeks, with those specimens having pitted surfaces averaging about 3.8 kips lower bond strength. Although rupture remained the principal failure mode beyond 4 weeks of conditioning, Table A4 shows that adhesion failure increased in frequency. Perhaps the high level of chlorides had some effect on the UHM adhesive, whereas the lower concentrations did not.

Regarding the ultimate strain results in Figure 28, statistical analysis indicated that no change occurred in performance over time for a given surface type subjected to a given chloride concentration. Despite the “spike” and “dip” observed in Figures 28b and 28c, respectively, no significant difference was present in the performance between the two surface types conditioned during the same chloride tests.

Figure 29 shows the load and strain curves versus time for the two different CFRP materials and steel surface conditions. Based on an analysis of variance single-factor test, no difference was found in bond performance of the pitted double-strap joints strengthened with UHM CFRP, regardless of the chloride exposure level (Figure 29b). However, the smooth specimens strengthened with the same CFRP material had less strength. This result was not surprising given that the smooth specimens in the marine environment exhibited a significant decrease in bond strength toward the end of the conditioning cycles (Figure 29a).

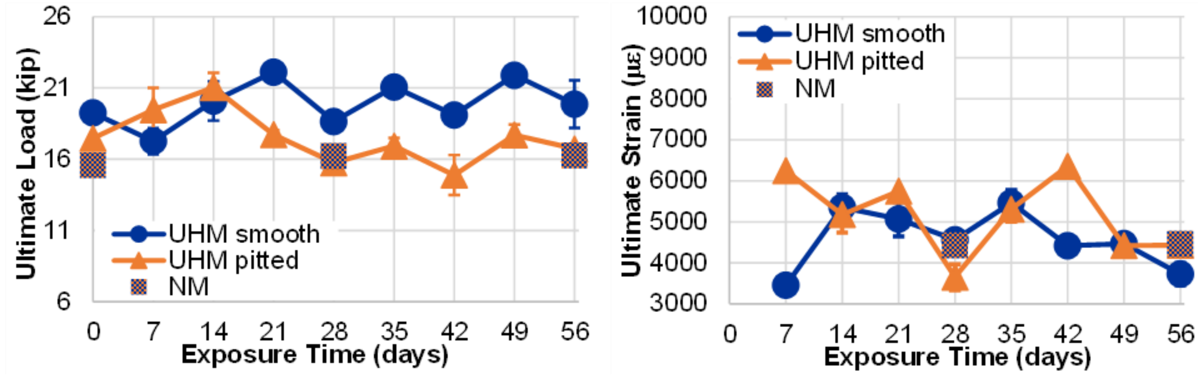

(a)

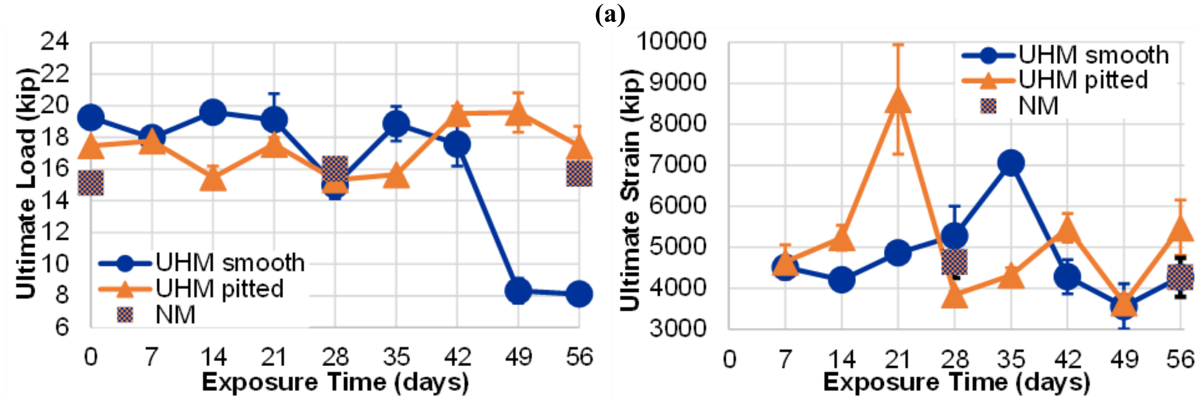

(b)

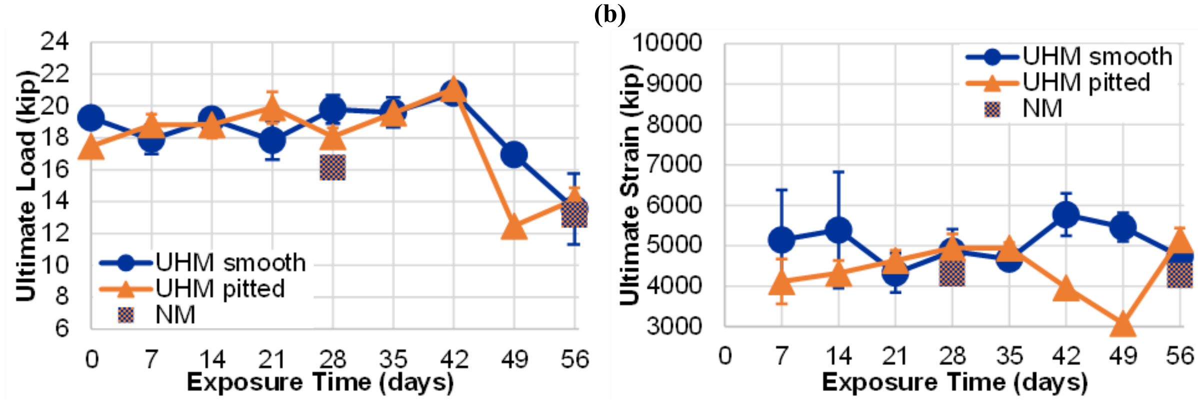

(c)

Figure 27. Ultimate Load and Strain for Laboratory Specimens Exposed to: (a) Heavy Deicing Salts; (b) Marine; (c) Rural Chloride Levels. NM = normal modulus carbon fiber reinforced polymer; UHM = ultra-high modulus carbon fiber reinforced polymer.

An additional two-factor analysis of variance analysis with replication indicated that no interaction was evident between the chloride concentration and surface condition variables. In other words, the type of chloride environment would not have a different effect on the durability of UHM CFRP bonded to deteriorated steel surfaces compared with fresh steel. Or reversely, the steel surface condition would not have a greater effect on bond durability in one region of the state versus another. Given that the focus of this research was on strengthening deteriorated steel structures, the fact that the chloride levels did not affect the bond performance of the specimens with simulated pitting helps to make the case that UHM CFRP could provide long-term strengthening of in-service bridges across Virginia.

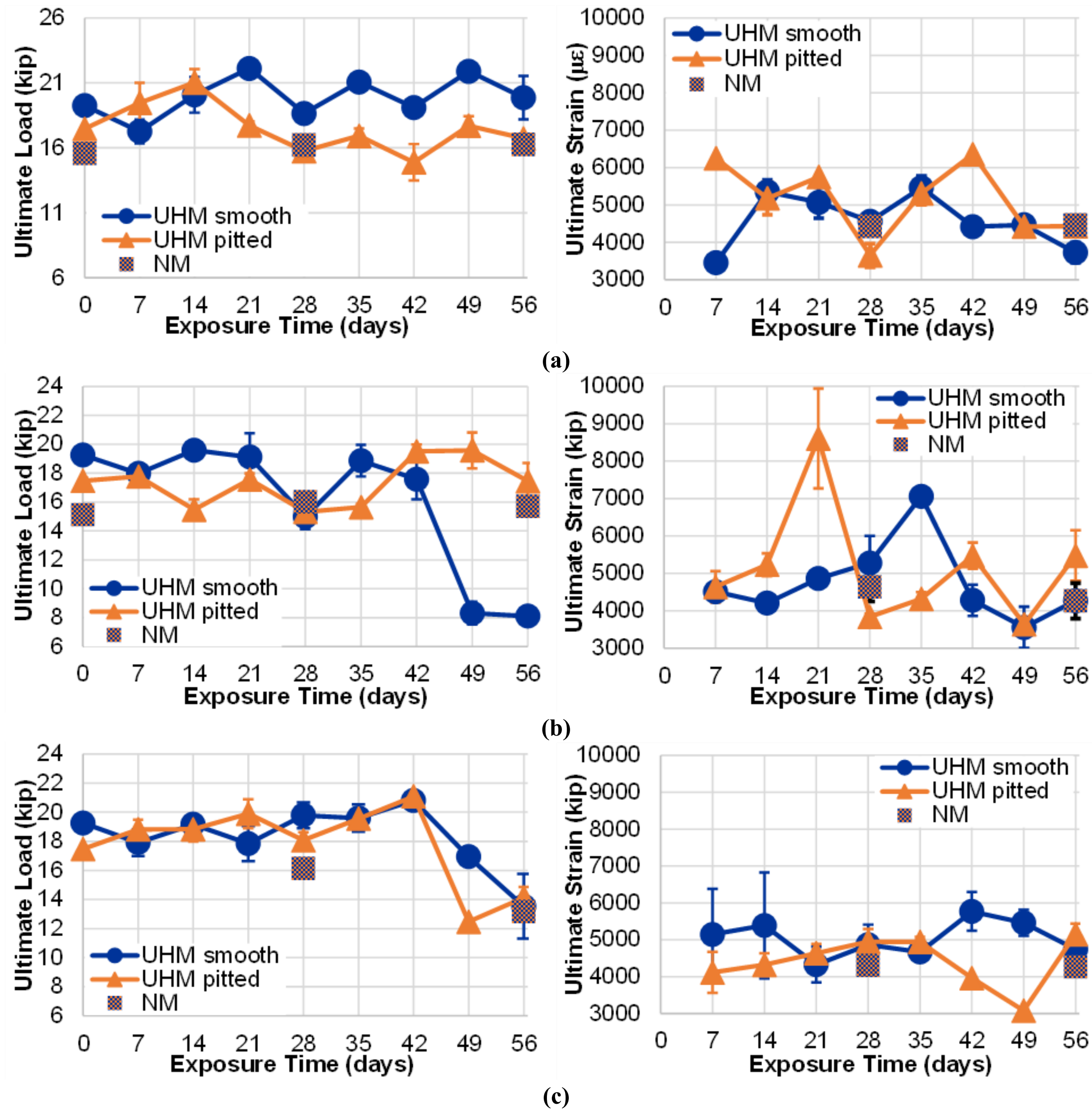

Figure 28. Ultimate Load and Strain for Laboratory Specimens Exposed to: (a) Heavy Deicing Salts; (b) Marine; (c) Rural Chloride Levels. NM = normal modulus carbon fiber reinforced polymer; UHM = ultra-high modulus carbon fiber reinforced polymer.

Similar to the analysis of ultimate strains in Figure 28, no statistical differences were observed in the strain curves when looking across the various chloride exposure levels in Figure 29.

Although Figure 29c does show the test results for the NM specimens, the testing did not include enough of these specimens to conduct any meaningful statistical analysis. Generally speaking, the bond strength and failure strain did not change substantially. Figure 29c shows that the load capacity of the double-strap joints strengthened with NM plate had improved slightly (6% to 7%) after 8 weeks of exposure to heavy and marine levels of chlorides. However, the difference may have been because of differences in testing operators or equipment.

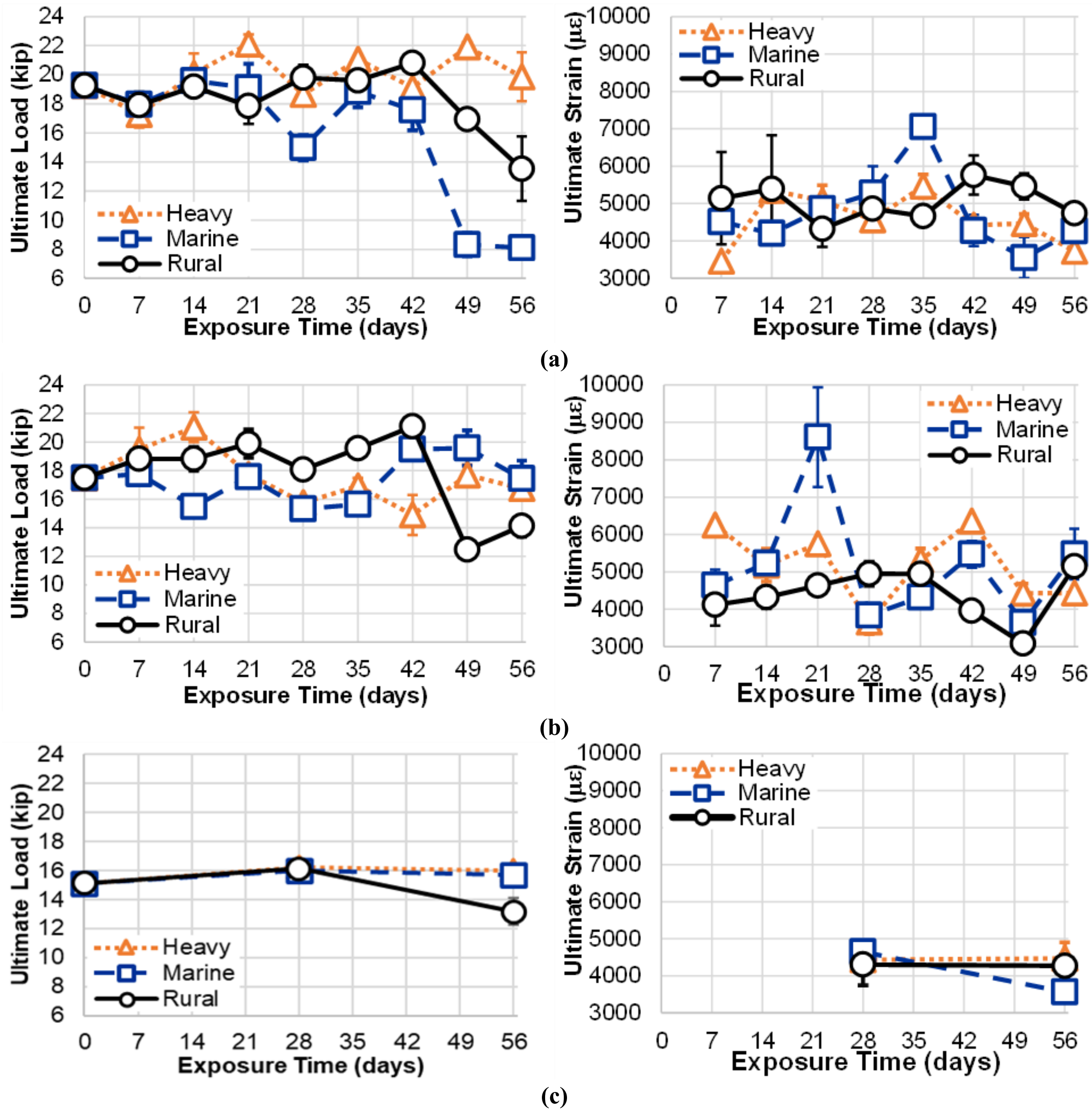

Figure 29. Comparisons of the Effects of Various Chloride Levels on the Ultimate Strength and Strain of Double-Strap Joints with (a) Smooth Steel and Ultra-High Modulus CFRP; (b) Pitted Steel with Ultra-High Modulus CFRP; (c) Smooth Steel with Normal Modulus CFRP. CFRP = carbon fiber reinforced polymer.

Of the 102 UHM specimens for which there were load test results, 6 had some amount of corrosion from within the bonded region of the double-strap joint. This count did not include the two smooth-surface specimens subjected to marine chloride levels that were part of the four specimens that had statistically weaker bond strength, as discussed previously. With that in mind, the average bond strengths for the noncorroded and partially corroded bond surfaces were 18.3 kips and 16.5 kips, respectively. However, a t-test analysis did not find that this difference was significant, although the p-value of 0.06 was close to the critical value of 0.05. Additional testing may find that a stronger association exists between oxide formation and bond strength. Such a result would reemphasize the need for proper preparation and installation of CFRP materials, including sealing the edges to prevent chloride ingress.

In Situ **Environmental Exposure**

A visual inspection of the specimens revealed corrosion of the steel bars and discoloration of the adhesive resulting from the *in situ* environmental aging process. The adhesive discoloration and corrosion progressed with increasing exposure time (Figure 30). As expected, exposure to the marine and heavy deicing salt environments led to greater corrosion of the steel substrates and adhesive discoloration compared with the rural environment, which experienced minimal weathering of the steel.

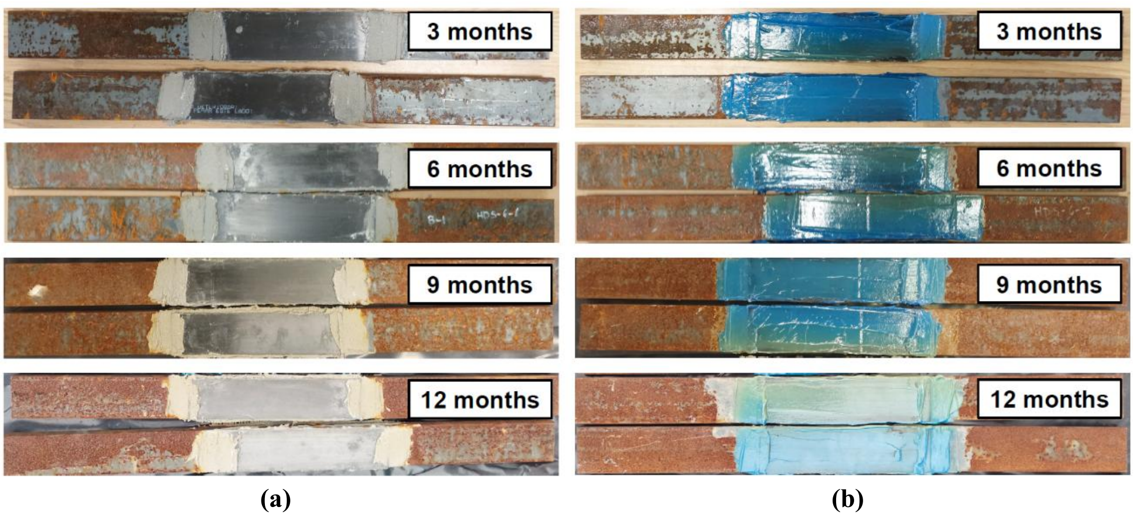

Figure 30. Photographs of (a) Normal Modulus and (b) Ultra-High Modulus Double-Strap Joints Through 12 Months of Aging in a Heavy Deicing Salts Environment

Failure Modes

Figure 31 demonstrates the failure modes of *in situ* aged NM joints. Table A8 also presents the failure modes for both sides of each specimen. The triggering failure mode for the baseline specimens was a combination of cohesive failure and CFRP delamination. This failure mode combination was also the predominant failure mode of the aged specimens. Accordingly, no substantial changes occurred to the failure mode throughout the environmental aging process, except for one specimen that was conditioned for 2 months in the marine environment. In that case, the failure mode was adhesive in nature at the GFRP-adhesive interface, and the joint strength was only 70% of the strength of the unconditioned control case.

Visual inspection of the post-failure surface revealed no corrosion of the steel within the bonded area after *in situ* exposure, regardless of the environment. The findings suggest that, for the environments and exposure duration investigated, the environmental exposure did not have a critical effect on the steel-adhesive interface, and as a result, the failure of the joint was determined by the failure of the CFRP-adhesive interface.

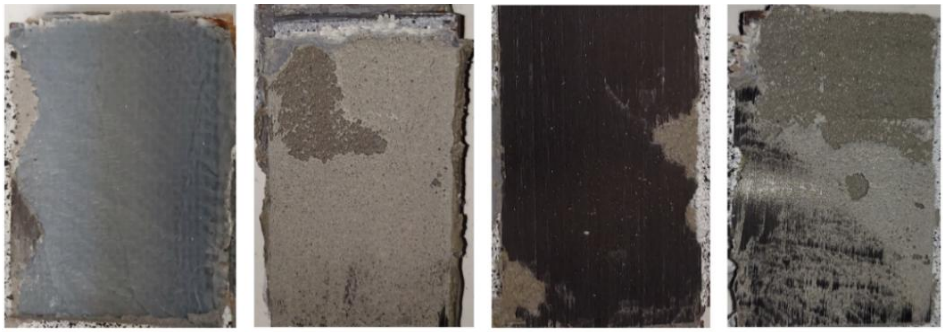

(a) (b) (c) (d)

Figure 31. Failure Modes of Aged Specimens Fabricated with the Normal Modulus Carbon Fiber Reinforced Polymer Plate: (a) Adhesion Failure Between Adhesive and Glass Fiber Reinforced Polymer; (b) Cohesive Failure; (c) Plate Delamination; (d) Combined Cohesive Failure and Delamination

Figure 32 presents the failure modes of the UHM specimens. Table A8 provides further details on the failure mode of each specimen. The main mode of failure of the unconditioned control specimens was CFRP rupture. This failure mode remained essentially unchanged after 12 months of *in situ* environmental exposure, although a few instances of solely cohesive failure and combinations of CFRP rupture and adhesion and cohesive failure occurred. Like the NM joints, the bonded area of steel plate remained uncorroded after environmental exposure.

(a) (b) (c) (d)

Figure 32. Failure Modes of Aged Specimens Strengthened with an Ultra-High Modulus Strand Sheet: (a) Combination of Adhesion Failure at the Steel-Adhesive Interface and Cohesive Failure; (b) Cohesive Failure; (c) CFRP Rupture; (d) Combined Cohesive Failure and CFRP Rupture. CFRP = carbon fiber reinforced polymer.

Joint Strength

Figure 33a shows the normalized ultimate tensile strengths of joints fabricated with an NM plate exposed to the three studied natural environments. Although the strength of the NM joints in the rural environment showed minimal degradation for the first 6 months of exposure, that strength decreased at a faster rate for the next 6 months. Thus, the joint strength retained 91% of the initial strength after 1 year of exposure. The specimens conditioned in a heavy deicing salt environment had a decreasing-increasing trend, in which the strength decreased during the first 6 months of exposure, but then regained all of that loss by 9 months and remained essentially unchanged for the remainder of the duration. Lastly, aging in a marine environment caused a 13% strength reduction after 3 months of conditioning but then increased 18% during the remaining 9 months.

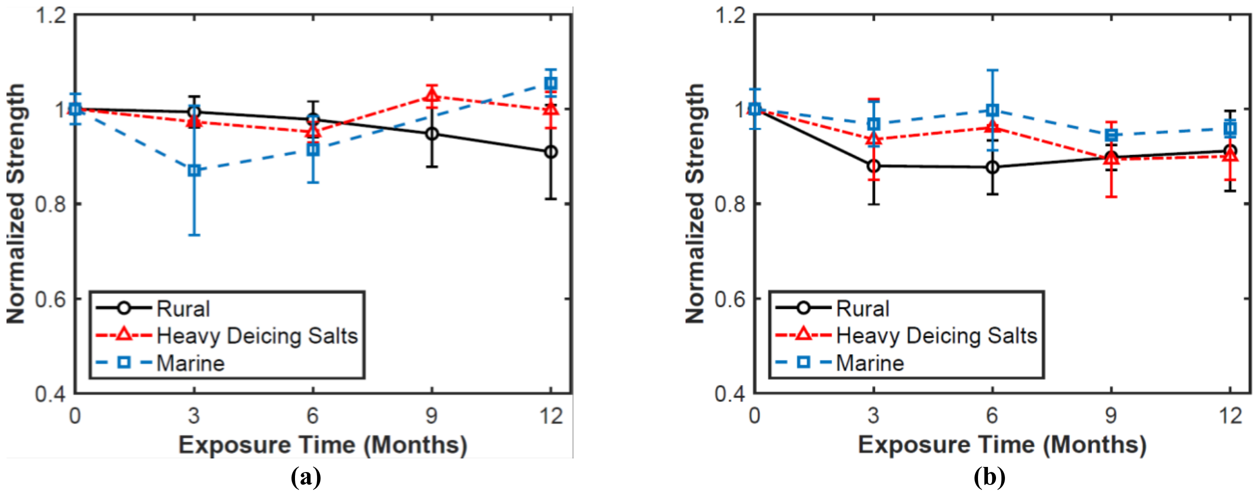

Figure 33. Influence of Environmental Aging on the Average Joint Strength of Double-Strap Joints Strengthened with (a) a Normal Modulus Plate and (b) an Ultra-High Modulus Strand Sheet

Figure 33b depicts the residual strength of aged specimens bonded with UHM strand sheets. The joint strength decreased to 88% of the initial strength after 3 months of exposure to a rural environment but then increased to 92% of the reference strength during the next 9 months. On the other hand, the UHM specimens exposed to heavy deicing salts and marine environments exhibited a more variable decreasing-increasing trend. The greatest reduction in tensile capacity occurred after 9 months of exposure, in which the joint strength was 89% and 95% of the unconditioned specimens for the heavy deicing salts and marine conditions, respectively. In summary, the findings revealed maximum strength reductions of 12%, 11%, and 5% after 12 months of aging in rural, heavy deicing salts, and marine environments, respectively. However, the specimens in rural and marine environments tended to regain a marginal amount (2–4%) of that loss after 1 year of exposure.

Combined Effects of Surface Condition and Environmental Aging

Figure 34 shows the combined effects of surface condition and environmental aging on the bond strength of UHM double-strap joints. The failure modes were the same as those in Figures 32b and 32c. Table A9 provides specific details on the failure modes of each specimen. Cohesive failure was the common failure mode of specimens in a rural environment, whereas CFRP rupture was the predominant mode of failure for specimens aged in the marine and heavy deicing salts environment. Exposure to heavy deicing salt conditions apparently had a positive effect on the bond strength, which increased 27% after 12 months of exposure. This fact contrasts with the 11% strength loss for the smooth-surfaced specimens, thus indicating that the surface pits enhanced adhesion via mechanical interlocking.

For the marine environment, the first 9 months of aging resulted in a 14% increase in the bond strength. However, the strength then decreased dramatically during the following 3 months, with the 12-month specimens having only 85% of the unconditioned control joints' strength.

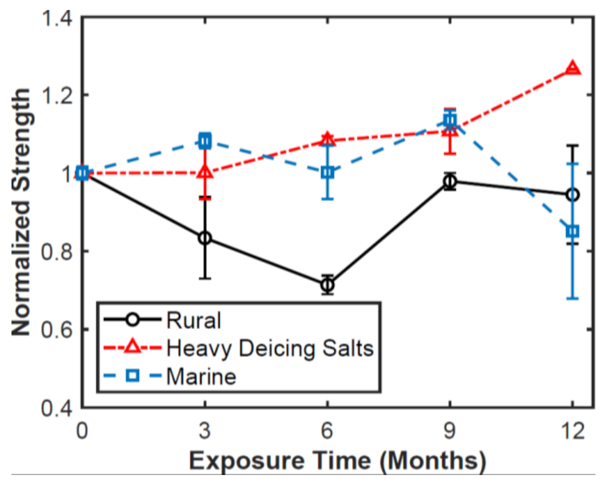

Figure 34. Influence of Environmental Aging and Surface Condition on the Joint Strength of Double-Strap Joints Strengthened with an Ultra-High Modulus Strand Sheet

Conditioning in the rural environment certainly negatively affected the bond strength, with all those specimens having lower strength than the unconditioned specimens. However, the trend for the specimens with surface pits was similar to that of the smooth specimens in Figure 33b, in which substantial degradation occurred at the early stages of exposure, followed by some strength recovery. In the case of the surface-pitted specimens in the rural environment, the bond strength decreased nearly 29% initially but then rebounded to 94% of the unaged strength after 12 months of exposure. Regression analysis showed a possible relationship between the mode of failure and the joint capacity for both the rural and heavy deicing salt environments. However, the same analysis indicated that any relationship between the two was relatively weak. Furthermore, the failure mode changed from cohesive failure on both faces of the specimen to cohesive failure on one face and CFRP rupture on the other after 9 months of exposure in rural conditions. Note the substantial 37% increase in strength when the mode of failure changed to include CFRP rupture.

Bond-Slip Behavior

To reiterate, the interfacial fracture energy, G_f, is the energy required to debond a local element and is equal to the area under the bond-slip curve. However, bond-slip models are suitable only for cases in which the failure occurs in the adhesive layer because of the equilibrium considerations in which they were derived. Therefore, because of the predominance of CFRP rupture failures in UHM specimens in this study, only the NM specimens are included in the following analysis.

The bond-slip relationships were calculated for each of the NM specimens following the methodology previously described. Figure 35a shows the average bond-slip curve derived for the unconditioned specimens, which was obtained by fitting the curves defined by the gray shaded region into a single, average curve. Figures 35b through 35d display the bond-slip curves of the NM specimens for each stage of exposure in rural, heavy deicing salts, and marine environments. An increasing and decreasing trend in τ_{max} is revealed after aging in rural conditions. As such, τ_{max} in Figure 35b increased above the reference value to a maximum (10% increase) after 3 months of exposure, followed by a decrease 16% below the interfacial shear stress in the control specimens at 6 months. The maximum interfacial shear stress then increased once again at 9 months and finished below τ_{max} of the unconditioned specimens at 12 months. A similar trend was observed for the heavy deicing salts and marine environments in Figures 35c and 35d, respectively, where τ_{max} was generally greater for the *in situ* aged conditions compared with the reference case, such that τ_{max} increased up to 28% and 39%, respectively.

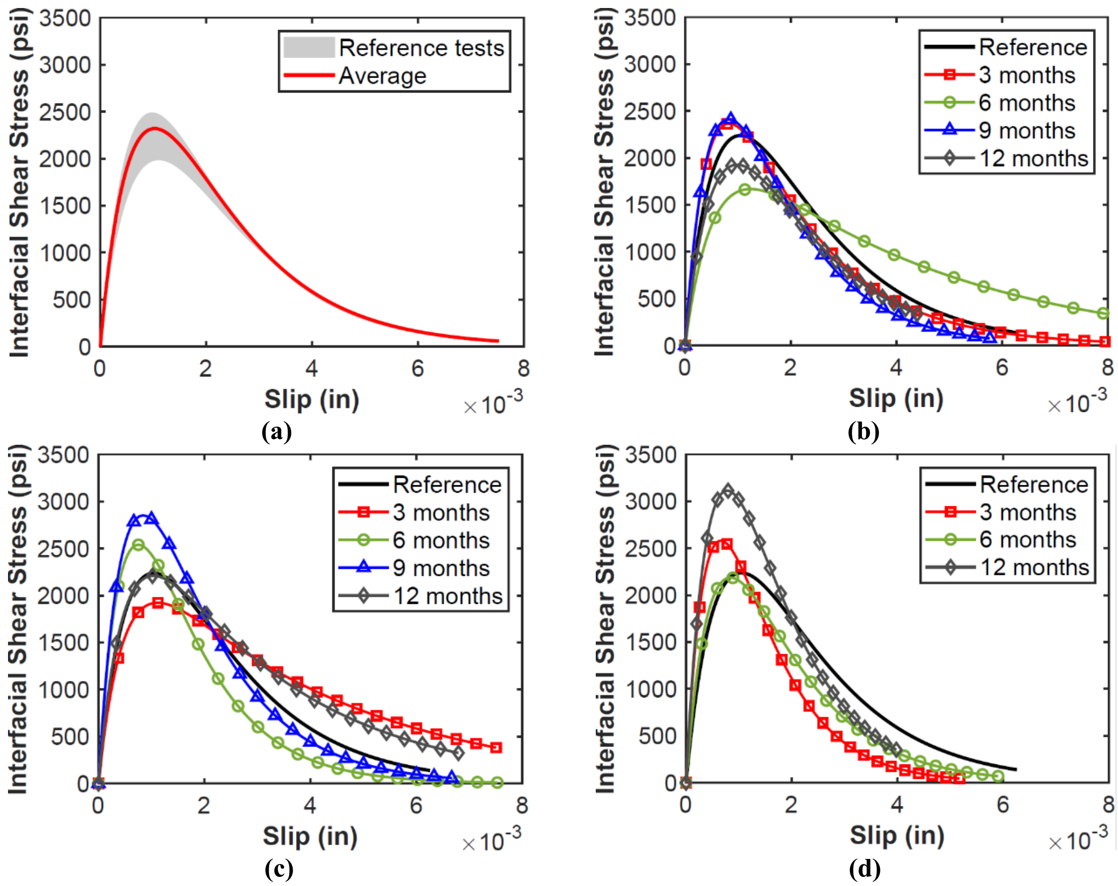

Figure 35. Bond-Slip Curves of Normal Modulus Specimens at Different Stages and Exposure Conditions: (a) Unexposed; (b) Rural; (c) Heavy Deicing Salts; (d) Marine Environments

Proposed Environmental Durability Factors

The bond-slip parameters discussed previously can be useful for establishing an environmental reduction factor, α_E, for steel strengthened with an NM plate. First, the following expressions describe the maximum interfacial shear stress in the aged condition, $\tau_{max,ENV}$:

$$\tau_{max,ENV} = \frac{\alpha_1 G_{f,ENV}}{2\alpha} \quad \text{(Equation 22)}$$

Where:

$$G_{f,ENV} = \alpha_2 G_f \quad \text{(Equation 23)}$$

$$\alpha_1 = \frac{\alpha \ln(2)}{s_{max.Env}} \quad \text{(Equation 24)}$$

$G_{f,ENV}$ and $s_{max,ENV}$ are the bond-slip parameters of the aged conditions, and α_1 and α_2 are coefficients that adjust the aged bond-slip parameters to those determined by the unaged conditions. Equations 22 through 24 are modifications of existing expressions for aged CFRP-concrete and GRFP-concrete beams adapted for CFRP-steel joints (Silva et al., 2013). $\tau_{max,ENV}$, $G_{f,ENV}$, and $s_{max,ENV}$ were directly obtained from the experimental data. Subsequently, the fitting coefficients α_1 and α_2 were calculated via Equations 23 and 24. The coefficient α_2 approximates the aged fracture energy, $G_{f,ENV}$, to the reference value, G_f.

Furthermore, the environmental reduction factor, α_E, is defined as:

$$\alpha_E = \frac{\varepsilon_{CFRP,max}^{ENV}}{\varepsilon_{CFRP,max}} \qquad \text{(Equation 25)}$$

Where:
$\varepsilon_{CFRP,max}$ = the maximum strain in the CFRP of the unaged specimens and is calculated as:

$$\varepsilon_{CFRP,max} = \sqrt{\frac{2G_f}{E_f t_f}} \qquad \text{(Equation 26)}$$

$\varepsilon_{CFRP,max}^{ENV}$ = the aged strain in the CFRP specimens and is calculated as:

$$\varepsilon_{CFRP,max}^{ENV} = \sqrt{\frac{2G_{f,ENV}}{E_f t_f}} \qquad \text{(Equation 27)}$$

Figure 36 presents the proposed aged bond-slip curve for each environment. The aged bond-slip relations were obtained by fitting the bond-slip curves of the aged conditions (shaded in gray) into a single curve that reflects the average behavior after 12 months of *in situ* aging for each environment.

Table 7 tabulates the aged bond-slip parameters and the results from the fitting procedure. The parameter α in Equation 20 refers to the fitting coefficient of the unaged conditions and is equal to 0.00148 inch for the NM material.

Like the other aging parameters, $\varepsilon_{CFRP,max}^{ENV}$ was directly determined from the aged bond-slip curves obtained from the experimental results. The maximum strain in the CFRP for the reference conditions was calculated with Equation 26. Similarly, the maximum strain in the CFRP laminate after *in situ* aging was determined using Equation 27, but substituting for $G_{f,ENV}$. Lastly, the environmental reduction factor, α_E, was computed via Equation 25 and is quantified along with α_1 and α_2 in Table 8. It should be noted that the tabulated values of α_E were rounded down to the nearest tenth to provide a more conservative estimate.

Considering the environmental effects, the bond strength of joints reinforced with an NM plate can be calculated by:

$$P_{u,ENV} = \alpha_E \cdot N \cdot b_f \sqrt{2 G_f E_f t_f \left(1+\frac{1}{\delta}\right)} \qquad \text{(Equation 28)}$$

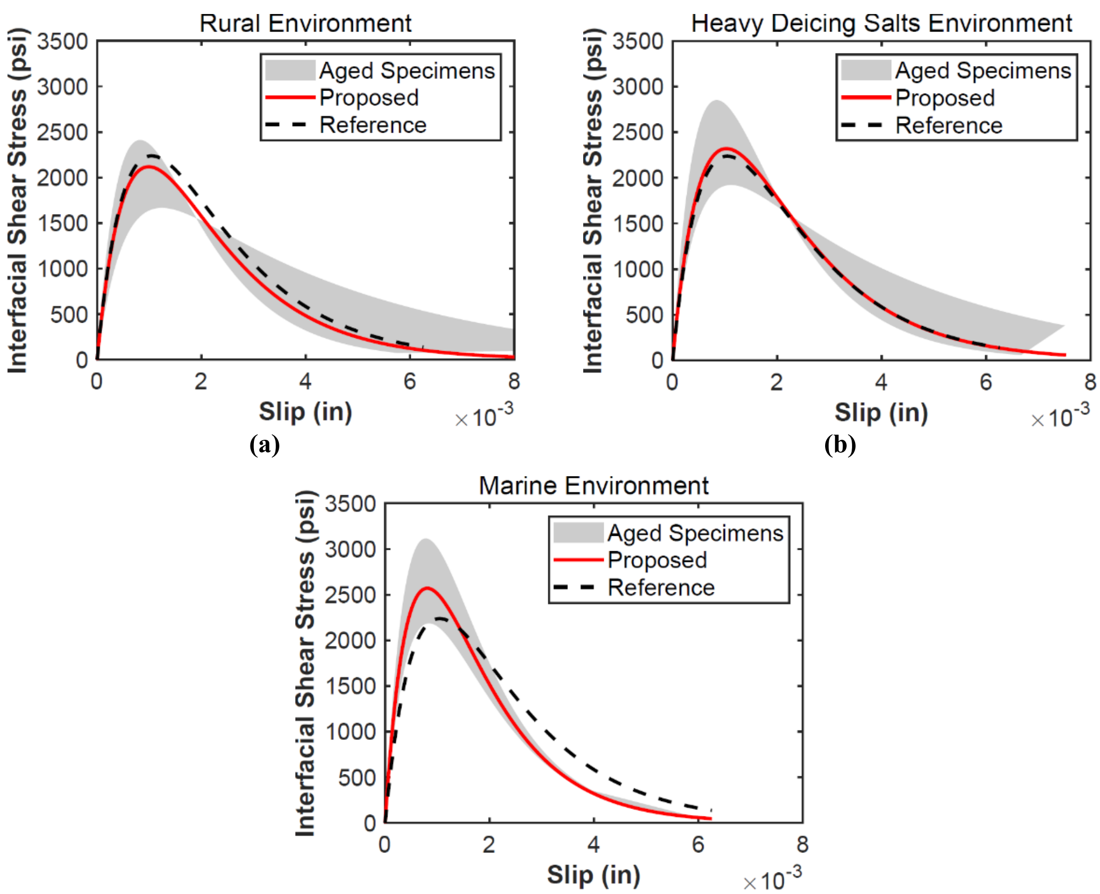

(a) (b)

(c)

Figure 36. Proposed Bond-Slip Curves of Normal Modulus Specimens Aged in (a) Rural, (b) Heavy Deicing Salts, and (c) Marine Environments

Table 7. Aged Bond-Slip Parameters

Environment	Fitting Results			$\tau_{max,ENV}$ (psi)	$s_{max,ENV}$ (in)	$G_{f,ENV}$ (lb/in)	$\varepsilon_{CFRP,max}$
	α (in)	β (in)	R^2				
Reference	0.00148	0.487	0.97	2254	0.00103	6.55	0.00302
Rural	0.00143	0.492	0.92	2118	0.00010	6.05	0.00290
Heavy deicing salts	0.00148	0.479	0.88	2320	0.00103	6.80	0.00308
Marine	0.00117	0.404	0.91	2570	0.00081	5.94	0.00287

Table 8. Values Proposed for the Coefficients α_1, α_2, and α_E

Environment	α_1	α_2	α_E
Reference	1.00	1.00	1.00
Rural	1.04	0.92	0.90
Heavy deicing salts	1.00	1.04	0.90
Marine	1.28	0.91	0.90

Comparisons between the calculated tensile capacity of the bonded joint (Equation 25) and the lowest experimental capacity for each of the three environmental conditions are in Figure 37. Figure 37 shows excellent agreement with the experimental findings, with deviations smaller than 5%.

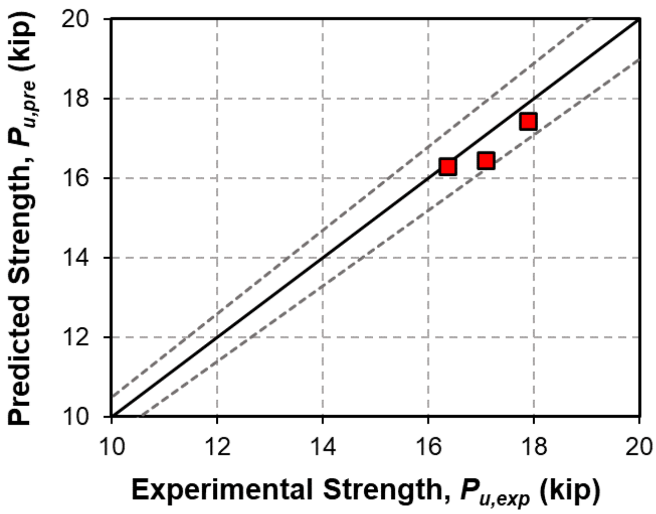

Figure 37. Comparison Between the Predicted Bond Strength Considering the Environmental Reduction Factor α_E and the Experimental Results

Fatigue Behavior

Static Tensile Tests and Constant Amplitude Fatigue Testing

The 12 static tensile tests of the UHM specimens used to determine the force amplitudes for the fatigue tests had a mean static load to failure, F_u, of 17.3 kip, with a standard deviation of 2.21 kip and a coefficient of variation of 0.13. Accordingly, Table 9 summarizes the parameters used in the fatigue loading protocol.

Table 9. Parameters for Fatigue Loading Protocol

Parameter	Force Amplitude Series		
	F_{a1}	F_{a2}	F_{a3}
F_{max} (kip)	10.40	8.66	6.93
F_{min} (kip)	1.04	0.87	0.69
F_a (kip)	4.68	3.90	3.12
Load Ratio	0.1	0.1	0.1
Area (in^2)	0.82	0.82	0.82

F_{max} = maximum force applied in the cyclic loading; F_{min} = minimum force applied in the cyclic loading; $F_a = \frac{F_{max} - F_{min}}{2}$.

The predominant failure mode for the smooth-surfaced specimens was cohesive failure, with just a few specimens showing a combination of adhesion and cohesive failures. On the other hand, most of the failures for the specimens with simulated corrosion pitting were a combination of cohesive and adhesion failures. The type of failure affected the fatigue performance of the specimens. Specimens that failed at a lower number of cycles for the same force amplitude corresponded to specimens that solely had adhesion failures. The F-N curves for both surfaces are in Figure 38. The fitted equations for smooth and pitted specimens, respectively, are:

$$F_a(N_f) = 9.75 - 0.45\ln(N_f) \quad \text{(Equation 29)}$$

$$F_a(N_f) = 8.75 - 0.37\ln(N_f) \quad \text{(Equation 30)}$$

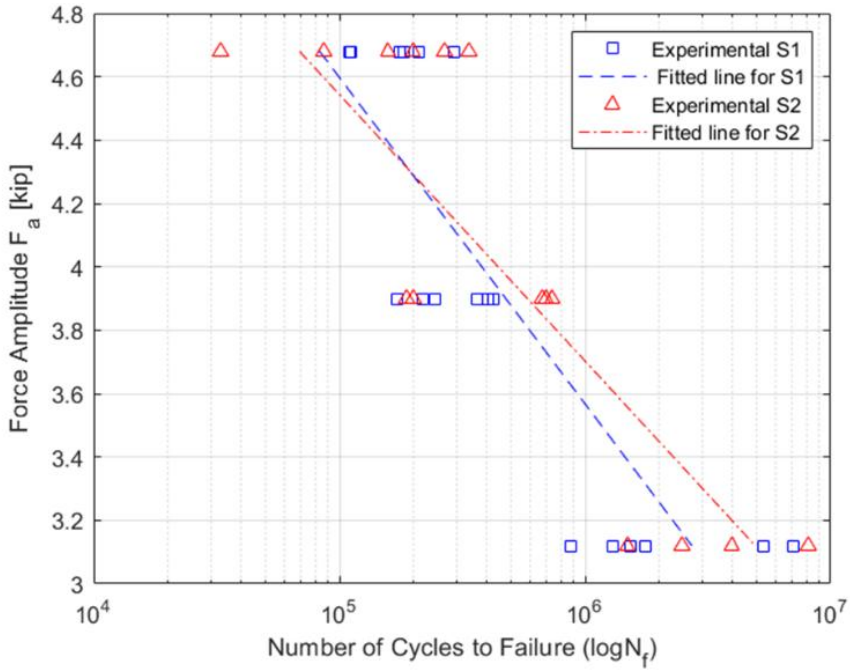

Figure 38. F-N Curves for Smoothed-Surface Specimens (S1) and Surfaces with Simulated Corrosion Pitting (S2)

The semilogarithmic equations for smooth and simulated pitting specimens are a good fit for the experimental fatigue data because their coefficients of correlation are $|r_{s1}| = 0.857$ and $|r_{s2}| = 0.846$, respectively. **Error! Not a valid bookmark self-reference.** tabulates the mean, standard deviation, and coefficient of variation for the number of cycles to failure for each force amplitude in this fatigue study.

Table 10. Summary of Fatigue Testing Results

Statistic	Smooth Surface (S1)			Simulated Pitting (S2)		
	F_{a1}	F_{a2}	F_{a3}	F_{a1}	F_{a2}	F_{a3}
Mean, $\overline{N}_f$	180,737	303,845	2,959,917	180,498	447,412	4,010,243
Standard Deviation, σ_{N_f}	68,820	105,496	2,548,694	113,289	275,924	2,914,604
Coefficient of Variation, μ_{N_f}	0.381	0.347	0.861	0.628	0.617	0.727

Partial Fatigue Testing: Nonlinear Strength Wear-Out Model

The results from the partial fatigue testing are in Figures 39a and 39b for the smooth surface and simulated pitting specimens, respectively. The intersection of the vertical lines and the fitted equations represents the point at which the residual strength equaled the maximum fatigue load at that specific force amplitude, thus ensuring failure. Clearly, Equations 29 and 30 provide a good fit for the experimental data for both types of specimens under the two greater force amplitudes. However, the predicted equation for the simulated pitting specimens subjected to force amplitude 3 may need more experimental data to produce a better model. Nevertheless, Figures 39a and 39b show a rapid decay in the residual strength for the first force amplitude, F_{a1}. Note that the American Association of State Highway and Transportation Officials (AASHTO) does not currently provide any fatigue guidance for fiber-reinforced polymer bonded to steel. The fatigue results provided herein are not sufficient for making any recommendations now but could be useful when added to a larger database in the future. For both surface types, the predominant failure mode was cohesive; however, some specimens did experience CFRP rupture.

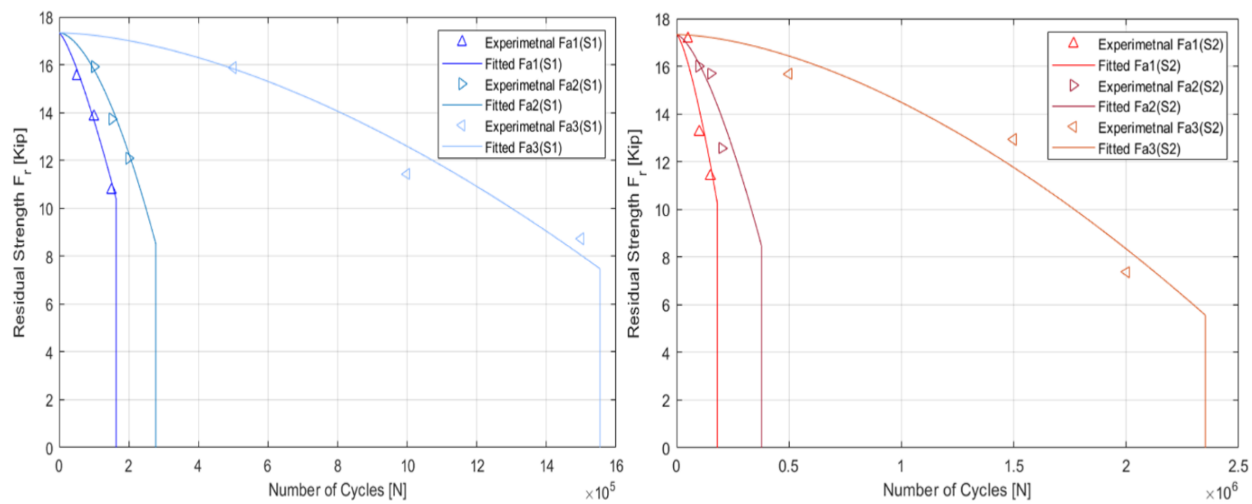

(a) **(b)**

Figure 39. Results for Partial Fatigue Testing and Fitted Strength Wear-out Models for (a) Smooth and (b) Simulated Corrosion Pitting Specimens

Economic Analysis

Recent and Current Cost Trends and Short-Term Outlooks

Compared with the relatively steady period from 2018 to 2020 at the producer price level (an approximate 6% increase during that period), fabricated steel plate prices surged about 46% starting in January of 2021 and held steady in 2022 (BLS, 2022b). The current trend for steel plates contrasts distinctly with sharp price declines for hot rolled coil in 2022, when prices were then below early 2018 prices. Notably, Nucor announced a continuing “discrete” steel plate price of $1,620/short ton for December 2022 (MetalMiner, 2022).

High plate prices would be expected to self-correct by attracting new capacity in steel production. However, an ambitious new U.S. energy policy providing billions in subsidies and grants for renewable energy infrastructure during the next decade could readily draw off some of the supply of plate desired for highway infrastructure within the next year or 2 (Richards et al., 2022; Rocky Mountain Institute, 2022), thus prolonging upward price pressures for steel plate.

On the other hand, a pivot to adequate substitutes may be the primary market force leading to lower steel plate prices in the future.

In the same economic environment, the prices of the Sika CarboDur and Nippon systems also increased sharply in the year or 2 before 2022, partly because thermosetting resins and resin adhesive components that constitute major elements of both strengthening systems (BLS, 2022c, 2022d). Producer prices for these ingredients had similar trends to those of steel plate from 2018 to 2022. A third component in CFRP strengthening systems, silica, saw about a 15% price increase during the studied period, thus seemingly having evaded extreme price surges observed in other materials, perhaps because of its abundance in nature (BLS, 2022e, 2022f).

Based on product distributor prices between July 2021 and July 2022, the 2022 Sika CarboDur repair costs for the hypothetical repairs in this analysis increased by about 10%, not accounting for general price inflation (Chad Campbell, personal communication, 2022). The hypothetical Nippon repair costs also increased by more than 150% between 2020 and 2022 (John Hepfinger, personal communication, 2022). Note that many departments of transportation experienced a similar level of cost inflation for many construction items during this period. At the time of this report, the NM, UHM, and enhanced UHM systems were estimated to cost an average of $184, $110, and $158 per square foot in materials, respectively, when applied at rates recommended by the manufacturers in 2022 prices.

VDOT has had an active interest in less costly and more durable substitutes for steel materials. Economic principles dictate, however, that interchangeable product options will tend to mirror each other's price trends, including rising prices, which can encourage more substitute products to be developed. Substitutes can also show "sticky" price resistance to declining demand, yet quick price hikes when demand increases. In any case, apart from noting the potential, it is not a simple matter to determine how much of a product's price increase is due to mirroring the behavior of other products.

Rules Affecting Federally Funded Transportation Construction Projects

In October 2022, a U.S. distributor of the Nippon CFRP system stated that the vast majority of the Nippon products were sourced and manufactured in the United States and would meet Buy America requirements. However, the Nippon CFRP included some materials that were sourced from Japan because it was the only source available for the base component (John Hepfinger, personal communication, 2022). Likewise, in November 2022, a U.S. distributor of the Sika CarboDur system stated that all SikaWrap system components were manufactured in the United States. Thus, the supply source was not an issue with regard to the Buy America provisions (Chad Campbell, personal communication, 2022).

Hypothetical *In Situ* Cost Comparison

Table 11 provides relative cost results of the alternative repair systems for the aforementioned Regular Advertisement and Award Process project, including materials and installation. The one-to-one replacement ratio shown in Table 11 fits the CFRP material to the steel strengthening plate as nearly as possible. Some repairs varied from this base case for the

NM material because of the need to fit the various-width NM plates to the requisite repair dimensions in the plans. In these cases, some CFRP cutting waste was built into the costs.

Also in Table 11, the analysis increased the square foot of the NM and UHM CFRP materials by 70% compared with the base case for the purpose of having sufficient CFRP to connect deteriorated webs and flanges with sound steel. These particular results are shown because, at this level, the four-layer UHM system was still cost-effective compared with steel plate, but the other two CFRP systems were not. In fact, at a 50% increase in CFRP material, five of the 12 NM repairs were less cost effective than steel plate, and only one seven-layer UHM repair remained cost effective.

Table 11. Cost Comparison Between Steel and CFRP Strengthening Systems, Based on Material Quantities and Installation[a]

Structure No.	Repair Type	Area of Material Used (ft^2)			Cost Ratio for Given Steel-to-CFRP Replacement Ratio					
					1:1 Steel-CFRP			1:1.7 Steel-CFRP		
		Steel	NM	UHM	$\frac{Steel}{NM}$	$\frac{Steel}{UHM_4}$	$\frac{Steel}{UHM_7}$	$\frac{Steel}{NM}$	$\frac{Steel}{UHM_4}$	$\frac{Steel}{UHM_7}$
1008	WF	56.1	56.1	56.2	1.27	1.63	1.11	0.75	0.96	0.65
1008	W	36.0	35.8	36.0	1.52	1.94	1.32	0.90	1.14	0.78
1051	WF_A	27.2	23.2	27.2	1.67	1.85	1.26	0.98	1.09	0.74
1051	WF_B	174.3	173.5	174.3	1.32	1.70	1.16	0.78	1.00	0.68
1900	WF	372.6	366.5	372.6	1.38	1.76	1.20	0.81	1.04	0.70
1900	W	35.3	34.8	35.3	1.61	2.04	1.39	0.95	1.20	0.82
1941	WF	281.5	279.3	281.5	1.38	1.76	1.20	0.81	1.04	0.70
1941	W	52.5	51.7	52.5	1.60	2.03	1.38	0.94	1.20	0.81
1941	F	10.8	11.0	10.8	1.83	2.39	1.62	1.08	1.41	0.95
6008	WF_A	290.8	294.5	295.5	1.55	1.96	1.33	0.91	1.15	0.78
6008	WF_B	282.6	322.6	322.7	1.36	1.73	1.17	0.80	1.02	0.69
6008	W	38.3	39.0	39.7	1.60	2.03	1.38	0.94	1.20	0.81

4 = four-layer system; 7 = seven-layer system; CFRP = carbon fiber reinforced polymer; F = flange repair; NM = normal modulus CFRP; UHM = ultra-high modulus CFRP; W= web repair; WF = web-flange repair.
[a] 1:1.7 Steel-CFRP ratio indicates the scenario in which every unit area of steel plate used for a given repair type was substituted with 70% more unit area of CFRP to account for extra area that might have been necessary to ensure adequate bond to the existing steel.

To this point, installation costs for CFRP products were estimated at about $146 per square foot for the NM and four-layer UHM systems and were assumed 50% higher for the seven-layer UHM system.

Table **12** shows the results of sensitivity testing of installation costs on cost-effectiveness, assuming a 1:1.5 installation cost ratio for steel plate versus CFRP.

In summary, the four-layer UHM system remained cost effective relative to steel, even if 70% more CFRP than steel plate was required. In this hypothetical CFRP scenario, the seven-layer UHM system is never preferable on the basis of cost to either the NM or the four-layer UHM systems, but the seven-layer system is cost effective relative to steel plate when less than 40% additional CFRP material is required to anchor repairs to in-service steel.

Table 12. Cost-Effectiveness of CFRP Systems Assuming Higher Unit Installation Costs Compared with Calculations in Table 11 for 1:1 Steel-to-CFRP Replacement Ratio

Structure No.	Repair Type	Cost Ratio for Given Increase in CFRP Installation Cost: 25%			50%		
		Steel/NM	Steel/UHM_4	Steel/UHM_7	Steel/NM	Steel/UHM_4	Steel/UHM_7
1008	WF	0.76	0.95	0.65	0.69	0.85	0.57
1008	W	0.91	1.13	0.77	0.83	1.01	0.68
1051	WF_A	1.00	1.08	0.73	0.91	0.96	0.65
1051	WF_B	0.79	0.99	0.67	0.72	0.88	0.60
1900	WF	0.83	1.03	0.70	0.76	0.91	0.62
1900	W	0.97	1.19	0.81	0.88	1.06	0.72
1941	WF	0.83	1.03	0.70	0.75	0.91	0.62
1941	W	0.96	1.19	0.80	0.87	1.05	0.71
1941	F	1.10	1.39	0.94	1.00	1.24	0.84
6008	WF_A	0.93	1.14	0.77	0.84	1.02	0.69
6008	WF_B	0.81	1.01	0.68	0.74	0.90	0.61
6008	W	0.96	1.19	0.80	0.88	1.06	0.71

4 = four-layer system; 7 = seven-layer system; CFRP = carbon fiber reinforced polymer; F = flange repair; NM = normal modulus CFRP; UHM = ultra-high modulus CFRP; W= web repair; WF = web-flange repair.

CONCLUSIONS

- *CFRP is an appropriate, cost-effective method for strengthening corrosion-damaged steel members with moderate levels of surface pitting and located anywhere in Virginia*. Based on the pitted specimens in this study, "moderate" surface pitting is defined as surfaces with pits that are not more than ¼ inch in diameter and ⅛ inch deep.

- *Steel surfaces with uniform corrosion can negatively affect the bond strength with CFRP, and by extension, the effective bond length*. Corrosion negatively affects the load transfer efficiency between corroded steel and the CFRP used to strengthen that same steel. For the case of NM joints, significant corrosion (S_a > 0.3 in, S_{dr} > 0.2%, and S_z > 2 in) reduces the strength. As for the case of UHM joints, the presence of corrosion reduces the bond strength regardless of corrosion severity.

- *Unlike uniform surface corrosion, surface roughness due to pitting does* not *negatively affect the bond strength between CFRP and steel*. Although an NM plate would probably have little deterioration in the bond, UHM systems could actually see a small benefit due to the surface roughness. Although the mode of failure may change compared with a smooth surface, that change should not affect the overall load capacity of the structure.

- *The joint strength increases and decreases after exposure to hygrothermal cycles and environmental aging*. Consequently, limited damage accumulation occurs, and the strength recovers throughout the exposure period. Note that this conclusion follows only 56 24-hour cycles between low-to-moderate and high temperatures in a laboratory controlled setting. The proposed strength reduction factor, α_{HT}, accounts for the minimum anticipated strength for that cyclic behavior.

- *Varying concentrations of chlorides do not affect the bond strength between UHM CFRP and steel*. Although the smooth specimens bonded with UHM CFRP and subjected to marine chloride concentrations in this study did have a statistically significant change in strength after 7 weeks of conditioning, those results are somewhat dubious because this subset of specimens was fabricated using a single batch of epoxy made solely for these two specimens. An error in the epoxy batching may have occurred, resulting in a substantially lower bond strength compared with other specimens, regardless of the degree and duration of simulated exposure.

- *The factors such as* $\alpha_E = 0.9$, $\alpha_{Cl} = 1.0$, *and* α_{HT} *given in Table 6 account for the reduction in the CFRP-steel bond strength for bridge elements exposed to* in situ *conditions*.

RECOMMENDATIONS

1. *A sufficiently long bond length greater than the effective bond length should be provided when strengthening deteriorated steel with CFRP to avoid premature failure, particularly when the surface is not smooth.*

2. *The proposed hygrothermal aging strength reduction factor,* α_{HT}, *should be used to provide a conservative estimate of the bond strength after exposure to conditions similar to those studied.*

3. *The proposed environmental durability factor,* α_E, *should be implemented to predict the bond strength after environmental aging.*

4. *The proposed value for the chloride exposure strength reduction factor,* α_{Cl}, *is 1.0, meaning chloride exposure essentially does not reduce the bond strength between UHM CFRP and steel.*

IMPLEMENTATION AND BENEFITS

The researcher and the technical review panel (listed in the Acknowledgments) for the project collaborate to craft a plan to implement the study recommendations and determine the benefits of doing so. This process is to ensure that the implementation plan is developed and approved with the participation and support of those involved with VDOT operations. The implementation plan and the accompanying benefits are provided here.

Implementation

Regarding *Recommendations 1 through 4*, VDOT's Structure and Bridge Division will incorporate the proposed reduction factors in the next Chapter 32 update of the *Manual of the Structure and Bridge Division* (VDOT, 2026) or in the publication of the Bridge Maintenance Manual, which is planned as the replacement for Chapter 32, by December 31, 2027.

Benefits

Successful implementation of the recommendations in this report will lead to certain economic benefits for VDOT. Solely looking at the material and installation cost analysis conducted in this report, VDOT could have saved $49,000 (or about 6%) on strengthening beam elements using a four-layered UHM FRP system in a group of five steel bridges, or approximately $10,000 per repaired bridge. Using CFRP to strengthen steel flexural members also provides other financial benefits, primarily that this rehabilitation technique has proven to be durable, and because CFRP is noncorrosive, the approach can extend the service life of deteriorated structures while mitigating future maintenance costs. Service life extension avoids interruptions to traffic across that bridge and allows for redistribution of funds to other structures that have a greater need for replacement. However, attempting to quantify those benefits is a complex task beyond the scope of this project.

Notwithstanding, implementing the recommendations from this report does have its drawbacks. For one, the technology for inspecting CFRP and its bond to the substrate is still not available. The industry is aware that this shortcoming can hinder wide adoption in the field. More directly tied to this report, the inclusion of strength reduction factors accounting for hygrothermal and chloride exposures will increase the amount of CFRP material beyond what would be required under current AASHTO specifications. This additional material requirement could reduce the cost advantages that were calculated in the economic analysis of this report. However, the inclusion of these factors does help to enhance the safety of the design.

ACKNOWLEDGMENTS

The authors of this report thank the following people who served on the technical review panel for this study: Adam Matteo, Project Champion, Assistant State Bridge Engineer for Maintenance, Structure and Bridge Division; Marc Stecker, Special Structures Manager, Structure and Bridge Division; Glenn McAninch, State Bridge Maintenance Specialist, Structure and Bridge Division; and Soundar Balakumaran, Associate Director for Structures, Virginia Transportation Research Council.

The research team acknowledge Dr. David Mokarem, Brett Farmer, and Garret Blankenship for their assistance at the Thomas M. Murray Structures Lab, as well as Debbie Cooper for her support throughout the project. Also, special appreciation goes to Bill Ordel, Nathan Maupin, David Starr, Tony Crupi, and Trip Poston for all of their assistance in conditioning and testing the chloride exposure specimens.

REFERENCES

Adams, R.D., and Peppiatt, N.A. Stress Analysis of Adhesive-Bonded Lap Joints. *Journal of Strain Analysis*, Vol. 9, No. 3, 1974, pp: 185–196. https://doi.org/10.1243/03093247V093185.

Agarwal, A., Foster, S.J., and Hamed, E. Wet Thermo-Mechanical Behavior of Steel-CFRP Joints—An Experimental Study. *Composites Part B: Engineering*, Vol. 83, 2015, pp. 284–296. https://doi.org/10.1016/j.compositesb.2015.08.025.

Bai, Y., Nguyen, T.C., Zhao, X.L., and Al-Mahaidi, R. Environment-Assisted Degradation of the Bond Between Steel and Carbon-Fiber-Reinforced Polymer. *Journal of Materials in Civil Engineering*, Vol. 26, No. 9, 2014. https://doi.org/10.1061/(ASCE)MT.1943-5533.0000951.

Balakumaran, S.S.G., and Weyers, R.E. *Performance of Bridge Deck Overlays in Virginia: Phase II: Service Life Performance*. FHWA/VTRC 20-R6. Virginia Transportation Research Council, Charlottesville, VA, 2019.

Baldan, A. Adhesively-Bonded Joints and Repairs in Metallic Alloys, Polymers and Composite Materials: Adhesives, Adhesion Theories and Surface Pretreatment. *Journal of Materials Science*, Vol. 39, No. 1, 2004, pp. 1–49. https://doi.org/10.1023/B:JMSC.0000007726.58758.e4.

Bocciarelli, M., Colombi, P., Fava, G., and Poggi, C. Interaction of Interface Delamination and Plasticity in Tensile Steel Members Reinforced by CFRP Plates. *International Journal of Fracture*, Vol. 146, No. 1–2, 2007, pp. 79–92. https://doi.org/10.1007/s10704-007-9144-8.

Brewis, D.M., Comyn, J., and Raval, A K. The Effect of Humidity on the Durability of Aluminium-Epoxide Joints. *International Journal of Adhesion and Adhesives*, Vol. 10, No. 4, 1990, pp. 247–253. https://doi.org/10.1016/0143-7496(90)90042-V.

Chotickai, P. Effect of Pre-Installed Corrosion on Steel Plate-CFRP Bond Characteristics. *International Journal of Adhesion and Adhesives*, Vol. 84, 2018, pp. 431–437. https://doi.org/10.1016/j.ijadhadh.2018.05.010.

Colombi, P., and Fava, G. Fatigue Behaviour of Tensile Steel/CFRP Joints. *Composite Structures*, Vol. 94, No. 8, 2012, pp. 2407–2417. https://doi.org/10.1016/j.compstruct.2012.03.001.

Comyn, J., Brewis, D.M., and Tredwell, S.T. Bonding of Aluminium Alloy with Some Phenolic Adhesives and a Modified Epoxide Adhesive, and Strength Changes on Exposure to Moist Air at 50°C. *The Journal of Adhesion*, Vol. 21, No. 1, 1987, pp. 59–78. https://doi.org/10.1080/00218468708074959.

Congressional Research Service. Congress Expands Buy America Requirements in the Infrastructure Investment and Jobs Act (P.L. 117-58). December 7, 2021. https://crsreports.congress.gov/product/pdf/IF/IF11989. Accessed November 30, 2022.

Dawood, M., and Rizkalla, S. Environmental Durability of a CFRP System for Strengthening Steel Structures. *Construction and Building Materials*, Vol. 24, No. 9, 2010, pp. 1682–1689. https://doi.org/10.1016/j.conbuildmat.2010.02.023.

Fawzia, S., Zhao, X.-L., and Al-Mahaidi, R. Bond-Slip Models for Double Strap Joints Strengthened by CFRP. *Composite Structures*, Vol. 92, No. 9, 2010, pp. 2137–2145. https://doi.org/10.1016/j.compstruct.2009.09.042.

Federal Highway Administration. National Bridge Inventory, 2022a. https://infobridge.fhwa.dot.gov/Data.

Federal Highway Administration. National Highway Construction Cost Index (NHCCI), 2022b. https://explore.dot.gov/views/NHIInflationDashboard/NHCCI_1?%3Aiid=1&%3Aembed=y&%3AisGuestRedirectFromVizportal=y&%3Adisplay_count=n&%3AshowVizHome=n&%3Aorigin=viz_share_link. Accessed November 28, 2022.

Fernando, N.D. *Bond Behaviour and Debonding Failures in CFRP-Strengthened Steel Members*. Ph.D. dissertation. Hong Kong Polytechnic University, Kowloon, Hong Kong, 2010. https://theses.lib.polyu.edu.hk/handle/200/5885.

Gledhill, R.A., Kinloch, A.J., and Shaw, S.J. A Model for Predicting Joint Durability. *The Journal of Adhesion*, Vol. 11, No. 1, 1980, pp. 3–15. https://doi.org/10.1080/00218468008078901.

Groshek, I.G. *Corrosion Behavior of ASTM A1010 Stainless Steel for Applications in Bridge Components.* Master's thesis. Virginia Polytechnic Institute and State University, Blacksburg, VA, 2017. https://vtechworks.lib.vt.edu/items/ec259267-eea9-47d1-8a82-38a7a91dbec8.

Hartanto, D., Hamed, E., Agarwal, A., and Foster, S.J. Behaviour of Steel-CFRP Lap Joints Under Hygrothermal Cycles and Sustained Loadings. *Composite Structures*, Vol. 203, 2018, pp. 740–749. https://doi.org/10.1016/j.compstruct.2018.07.032.

Hart-Smith, L.J. *Adhesive-Bonded Double-Lap Joints*. NASA CR 112235. National Aeronautics and Space Administration, Hampton, VA, 1973.

Hart-Smith, L.J. Further Developments in the Design and Analysis of Adhesive-Bonded Structural Joints. In *Joining of Composite Materials*, K.T. Kedward (Ed.). ASTM International, Conshohocken, PA, 1981, pp. 3-3–29). https://doi.org/10.1520/STP33472S.

Heshmati, M., Haghani, R., and Al-Emrani, M. Effects of Moisture on the Long-Term Performance of Adhesively Bonded FRP/Steel Joints Used in Bridges. *Composites Part B: Engineering*, Vol. 92, 2016, pp. 447–462. https://doi.org/10.1016/j.compositesb.2016.02.021.

Heshmati, M., Haghani, R., and Al-Emrani, M. Durability of Bonded FRP-to-Steel Joints: Effects of Moisture, De-icing Salt Solution, Temperature and FRP Type. *Composites Part B: Engineering*, Vol. 119, 2017a, pp. 153–167. https://doi.org/10.1016/j.compositesb.2017.03.049.

Heshmati, M., Haghani, R., and Al-Emrani, M. Durability of CFRP/Steel Joints Under Cyclic Wet-Dry and Freeze-Thaw Conditions. *Composites Part B: Engineering*, Vol. 126, 2017b, pp. 211–226. https://doi.org/10.1016/j.compositesb.2017.06.011.

Hollaway, L.C., and Cadei, J. Progress in the Technique of Upgrading Metallic Structures with Advanced Polymer Composites. *Progress in Structural Engineering and Materials*, Vol. 4, No. 2, 2002, pp. 131–148. https://doi.org/10.1002/pse.112.

International Standards Organization. *ISO 21920-2:2021: Geometrical Product Specifications (GPS)-Surface Texture: Profile-Part 2: Terms, Definitions and Surface Texture Parameters*. Geneva, Switzerland, 2021a.

International Standards Organization. *ISO 25178-2:2021: Geometrical Product Specifications (GPS)-Surface Texture: Areal-Part 2: Terms, Definitions and Surface Texture Parameters*. Geneva, Switzerland, 2021b.

Kamruzzaman, M., Jumaat, M.Z., Ramli Sulong, N.H., and Islam, A.B.M.S. A Review on Strengthening Steel Beams Using FRP Under Fatigue. *The Scientific World Journal*, 2014, pp. 1–21. https://doi.org/10.1155/2014/702537.

Li, A., Xu, S., Wang, H., Zhang, H., and Wang, Y. Bond Behaviour Between CFRP Plates and Corroded Steel Plates. *Composite Structures*, Vol. 220, 2019, pp. 221–235. https://doi.org/10.1016/j.compstruct.2019.03.068.

Liu, S., Cheng, X., Zhang, Q., Zhang, J., Bao, J., and Guo, X. An Investigation of Hygrothermal Effects on Adhesive Materials and Double Lap Shear Joints of CFRP Composite Laminates. *Composites Part B: Engineering*, Vol. 91, 2016, pp. 431–440. https://doi.org/10.1016/j.compositesb.2016.01.051.

Lottes, S.A., and Bojanowski, C. *Computer Modeling and Analysis of Truck Generated Salt-Spray Transport Near Bridges*. ANL/ESD/13-1. Argonne National Laboratory, Oak Ridge, TN, 2013. https://doi.org/10.2172/1087817.

MetalMiner. Raw Steels MMI: Steel Price Downtrend Resumes While Plate Prices Hold Flat, 2022. https://agmetalminer.com/2022/11/17/raw-steels-mmi-steel-price-november-2022/?utm_campaign=Weekly%20Newsletter%20Campaign&utm_medium=email&_hsmi=236007524&_hsenc=p2ANqtz-83IrrdFviWAa0KCfmD9FQLmcw5zn4avY8KWW1G8aoL4wvfGPduSglDXzymBXki3wBgWkppSg6Z2ZwM8ifnsg5l_6-hoCQzpgILOJvZu3gZfbBKJYQ&utm_content=236007524&utm_source=hs_email. Accessed November 30, 2022.

Mubashar A., Ashcroft, I.A., Critchlow, G.W., Crocombe, A.D. Moisture Absorption-Desorption Effects in Adhesive Joints. *International Journal of Adhesion and Adhesives*, Vol. 29, No. 8, 2009. http://dx.doi.org/10.1016/j.ijadhadh.2009.05.001.

National Climatic Data Center. Climate Data Online, March 2021. https://www.ncdc.noaa.gov/cdo-web/.

Nguyen, T.-C., Bai, Y., Zhao, X.-L., and Al-Mahaidi, R. Durability of Steel/CFRP Double Strap Joints Exposed to Sea Water, Cyclic Temperature and Humidity. *Composite Structures*, Vol. 94, No. 5, 2012, pp. 1834–1845. https://doi.org/10.1016/j.compstruct.2012.01.004.

Nippon Steel Chemical and Material Co., Ltd. Product Data Sheet, 2020. Accessed April 11, 2022.

Pang, Y., Wu, G., Wang, H.-T., Gao, D., and Zhang, P. Bond-Slip Model of the CFRP-Steel Interface with the CFRP Delamination Failure. *Composite Structures*, Vol. 13, 2021.

Pang, Y.-Y., Wu, G., Wang, H.-T., Su, Z.-L., and He, X.-Y. Experimental Study on the Bond Behavior of the CFRP-Steel Interface Under the Freeze-Thaw Cycles. *Journal of Composite Materials*, Vol. 54, No. 1, 2020, pp. 13–29. https://doi.org/10.1177/0021998319851191.

Peiris, A., and Harik, I. Steel Bridge Girder Strengthening Using Postinstalled Shear Connectors and UHM CFRP Laminates. *Journal of Performance of Constructed Facilities*, Vol. 29, No. 5, 2015. https://doi.org/10.1061/(ASCE)CF.1943-5509.0000625.

Phan, H.B., Holloway, D.S., and Jiao, H. An Investigation into the Effect of Roughness Conditions and Materials on Bond Strength of CFRP/Steel Double Strap Joints. *Australian Journal of Structural Engineering*, Vol. 16, No. 4, November 2015, pp. 292–301.

Richards, H., Anchondo, C., and Behr, P. How Manchin-Schumer Would Change Energy, From Oil to Solar. *E&E News*, July 29, 2022. https://www.eenews.net/articles/how-manchin-schumer-would-change-energy-from-oil-to-solar/. Accessed December 1, 2022.

Rocky Mountain Institute. Congress's Climate Triple Whammy: Innovation, Investment, and Industrial Policy. August 22, 2022. https://rmi.org/climate-innovation-investment-and-industrial-policy. Accessed November 30, 2022.

SAE International. *Surface Vehicle Standard J2334: Laboratory Cyclic Corrosion Test*. Society of Automotive Engineers International, Warrendale, PA, 2016.

Shenoy, V., Ashcroft, I.A., Critchlow, G.W., Crocombe, A.D., and Abdel Wahab, M.M. An Evaluation of Strength Wearout Models for the Lifetime Prediction of Adhesive Joints

Subjected to Variable Amplitude Fatigue. *International Journal of Adhesion and Adhesives*, Vol. 29, No. 6, 2009, pp. 639–649. https://doi.org/10.1016/j.ijadhadh.2009.02.008.

Sherry, S. *Carbon Fiber Reinforced Polymer Retrofits to Increase the Flexural Capacity of Deteriorated Steel Members*. Ph.D. dissertation. Virginia Polytechnic Institute and State University, Blacksburg, VA, 2021.

Shi, J., Zhu, H., Wu, Z., Seracino, R., and Wu, G. Bond Behavior between Basalt Fiber-Reinforced Polymer Sheet and Concrete Substrate under the Coupled Effects of Freeze-Thaw Cycling and Sustained Load. *Journal of Composites for Construction*, Vol. 17, No. 4, 2013, pp. 530–542. https://doi.org/10.1061/(ASCE)CC.1943-5614.0000349.

Sika. SikaWrap Hex-106G, 2018. Accessed April 11, 2022.

Sika. Sikadur 330, 2022. Accessed April 11, 2022.

Silva, M.A.G., Biscaia, H.C., and Marreiros, R. Bond-Slip on CFRP/GFRP-to-Concrete Joints Subjected to Moisture, Salt Fog and Temperature Cycles. *Composites Part B: Engineering*, Vol. 55, 2013, pp. 374–385. https://doi.org/10.1016/j.compositesb.2013.06.015.

Teng, J.G., Yu, T., and Fernando, D. Strengthening of Steel Structures with Fiber-Reinforced Polymer Composites. *Journal of Constructional Steel Research*, Vol. 78, 2012, pp. 131–143. https://doi.org/10.1016/j.jcsr.2012.06.011.

U.S. Bureau of Labor Statistics. Producer Price Indexes, 2022a. https://www.bls.gov/ppi/. Accessed November 29, 2022.

U.S. Bureau of Labor Statistics. Producer Price Index by Commodity: Metals and Metal Products: Fabricated Steel Plate (WPU10760102), 2022b. https://fred.stlouisfed.org/series/WPU10760102. Accessed November 29, 2022.

U.S. Bureau of Labor Statistics. Producer Price Index by Industry: Plastics Material and Resins Manufacturing: Thermosetting Resins and Plastics Materials (PCU3252113252114), 2022c. https://fred.stlouisfed.org/series/PCU3252113252114. Accessed November 30, 2022.

U.S. Bureau of Labor Statistics. Producer Price Index by Industry: Adhesive Manufacturing: Synthetic Resin and Rubber Adhesives, Including All Types of Bonding and Laminating Adhesives (PCU3255203255204), 2022d. https://fred.stlouisfed.org/series/PCU3255203255204. Accessed November 30, 2022.

U.S. Bureau of Labor Statistics. Producer Price Index by Commodity: Nonmetallic Mineral Products: Ground or Treated Minerals and Earths (WPU13990209), 2022e. https://fred.stlouisfed.org/series/WPU13990209. Accessed November 30, 2022.

U.S. Bureau of Labor Statistics. Producer Price Index by Commodity: Nonmetallic Mineral Products: Nonmetallic Minerals and Products, Not Elsewhere Classified (WPU1399), 2022f. https://fred.stlouisfed.org/series/WPU1399. Accessed November 29, 2022.

Vassilopoulo, A.P. *Fatigue Life Prediction of Composites and Composite Structures*. Second Edition. Woodhead Publishing, Cambridge, England, 2020.

Virginia Department of Transportation. Chapter 32—Preservation, Maintenance, Repair, Widening and Rehabilitation. In *Manual of the Structure and Bridge Division, Part II: Design Guidelines*. Richmond, VA, April 2026.

Virginia Employment Commission. Virginia Career and Workforce Labor Market Information: Structural Metal Fabricators and Fitters, 2022a. https://svc.mt.gov/dli/careersearch/virginia/Details?occupation=51-2041.00. Accessed November 28, 2022.

Virginia Employment Commission. Virginia Career and Workforce Labor Market Information: Carpenters, 2022b. https://svc.mt.gov/dli/careersearch/virginia/Details?occupation=47-2031.00. Accessed November 28, 2022.

Virginia Employment Commission. Virginia Career and Workforce Labor Market Information: First-Line Supervisors of Construction Trades and Extraction Workers, 2022c. https://svc.mt.gov/dli/careersearch/virginia/Details?occupation=47-1011.00. Accessed November 28, 2022.

Wang, H.-T., Wu, G., Dai, Y.-T., and He, X.-Y. Determination of the Bond-Slip Behavior of CFRP-to-Steel Bonded Interfaces Using Digital Image Correlation. *Journal of Reinforced Plastics and Composites*, Vol. 35, No. 18, 2016a, pp. 1353–1367. https://doi.org/10.1177/0731684416651342.

Wang, H.-T., Wu, G., Dai, Y.-T., and He, X.-Y. Experimental Study on Bond Behavior between CFRP Plates and Steel Substrates Using Digital Image Correlation. *Journal of Composites for Construction*, Vol. 20, No. 6, 2016b. https://doi.org/10.1061/(ASCE)CC.1943-5614.0000701.

Williams, A.L., and Stensland, G.J. *Atmospheric Dispersion Study of Deicing Salt Applied to Roads.* FHWA/IL/HRC.2006-1. Illinois Department of Transportation, Springfield, IL, 2006.

Wu, C., Zhao, X., Duan, W.H., and Al-Mahaidi, R. Bond Characteristics Between Ultra High Modulus CFRP Laminates and Steel. *Thin-Walled Structures*, Vol. 51, 2012, pp. 147–157.

Wu, Z., Yuan, H., and Niu, H. Stress Transfer and Fracture Propagation in Different Kinds of Adhesive Joints. *Journal of Engineering Mechanics*, Vol. 128, No. 5, 2002, pp. 562–573. https://doi.org/10.1061/(ASCE)0733-9399(2002)128:5(562).

Xia, S.H., and Teng, J.G. Behaviour of FRP-to-Steel Bonded Joints. *Proceedings of the International Symposium on Bond Behaviour of FRP in Structures*, Vol. 8, 2005.

Xu, S., Li, H., Wang, Y., Wang, Y., and Wang, Y. Influence of Corrosion on the Bond Behavior in CFRP-Steel Single Lap Joints. *Construction and Building Materials*, Vol. 236, 2020. https://doi.org/10.1016/j.conbuildmat.2019.117607.

Yang, Y., Silva, M.A.G., Biscaia, H., and Chastre, C. Bond Durability of CFRP Laminates-to-Steel Joints Subjected to Freeze-Thaw. *Composite Structures*, Vol. 212, 2019a, pp. 243–258. https://doi.org/10.1016/j.compstruct.2019.01.016.

Yang, Y., Silva, M.A.G., and Silva, R.J.C. Material Degradation of CFRP-to-Steel Joints Subjected to Salt Fog. *Composites Part B: Engineering*, Vol. 173, 2019b. https://doi.org/10.1016/j.compositesb.2019.05.095.

Yang, Y., Yue, Q., and Peng, F. Experimental Research on Bond Behavior of CFRP to Steel. *Proceedings of the International Symposium on Bond Behaviour of FRP in Structures*, Vol. 6, 2005.

Yu, Q.-Q., Gao, R.-X., Gu, X.-L., Zhao, X.-L., and Chen, T. Bond Behavior of CFRP-Steel Double-Lap Joints Exposed to Marine Atmosphere and Fatigue Loading. *Engineering Structures*, Vol. 175, 2018, pp. 76–85. https://doi.org/10.1016/j.engstruct.2018.08.012.

Yuan, H., Teng, J.G., Seracino, R., Wu, Z.S., and Yao, J. Full-Range Behavior of FRP-to-Concrete Bonded Joints. *Engineering Structures*, Vol. 26, No. 5, 2004, pp. 553–565. https://doi.org/10.1016/j.engstruct.2003.11.006.

Zhao, X.-L., and Zhang, L. State-of-the-Art Review on FRP Strengthened Steel Structures. *Engineering Structures*, Vol. 29, No. 8, 2007, pp. 1808–1823. https://doi.org/10.1016/j.engstruct.2006.10.006.

APPENDIX

Table A1. Database of Experimental and Predicted Results

Specimen	$G_{f,exp}$ (lb/in)	$G_{f,pred}$ (lb/in)	$\frac{G_{f,pred}}{G_{f,exp}}$	$P_{u,exp}$ (kip)	$P_{u,pred}$ (kip)	$\frac{P_{u,pred}}{P_{u,exp}}$
Phan et al. (2015)						
MCW3-1	10.77	13.06	1.21	13.60	14.97	1.10
MCW3-2	13.29	13.06	0.98	15.10	14.97	0.99
MCW3-3	11.31	13.06	1.15	13.93	14.97	1.07
MCW3-4	12.43	13.06	1.05	14.61	14.97	1.02
MCW3-5	15.68	13.06	0.83	16.40	14.97	0.91
MCW3-6	12.24	13.06	1.07	14.49	14.97	1.03
MCW3-7	10.59	13.06	1.23	13.48	14.97	1.11
MCW3-8	12.82	13.06	1.02	14.83	14.97	1.01
MCP1-1	6.58	5.17	0.79	20.22	17.93	0.89
MCP1-2	6.01	5.17	0.86	19.33	17.93	0.93
MCP1-3	6.46	5.17	0.80	20.04	17.93	0.89
MCP1-4	5.20	5.17	0.99	17.98	17.93	1.00
MNS2-1	1.20	0.99	0.82	18.76	17.04	0.91
MNS2-2	1.32	0.99	0.75	19.66	17.04	0.87
MSW3-1	5.77	9.66	1.67	9.96	12.88	1.29
MSW3-2	7.62	9.66	1.27	11.44	12.88	1.13
Chotickai (2018)						
ESK 0.1-D1	6.24	5.16	0.83	15.95	14.51	0.91
ESK 0.1-D2	6.70	5.01	0.75	16.54	14.31	0.86
ESK 0.1-D3	7.02	5.29	0.75	16.93	14.70	0.87
ESK 0.2-D1	6.47	6.10	0.94	16.25	15.78	0.97
ESK 0.2-D2	7.54	6.20	0.82	17.55	15.90	0.91
ESK 0.2-D3	7.52	5.99	0.80	17.52	15.64	0.89
Li et al. (2019)						
C3-B5-T1	5.51	4.12	0.75	11.69	10.10	0.86
C3-B5-T2	7.24	5.29	0.73	13.39	11.45	0.85
C3-B5-T3	6.67	6.36	0.95	12.85	12.55	0.98
C3-B5-T4	6.15	6.58	1.07	12.34	12.77	1.03
C4-B4-T1	5.73	4.12	0.72	11.91	10.10	0.85
C4-B5-T1	5.58	4.32	0.77	11.75	10.34	0.88
C6-B5-T1	6.01	3.78	0.63	12.20	9.67	0.79
C6-B5-T2	6.35	5.33	0.84	12.54	11.49	0.92
C6-B5-T3	7.37	6.67	0.91	13.51	12.85	0.95
C6-B5-T4	6.74	7.01	1.04	12.92	13.18	1.02
C8-B4-T1	5.87	4.38	0.75	12.05	10.42	0.86
C8-B5-T1	5.93	4.41	0.74	12.11	10.45	0.86
C8-B5-T2	6.42	5.18	0.81	12.61	11.32	0.90
C8-B5-T3	7.20	5.81	0.81	13.35	12.00	0.90
C8-B5-T4	5.95	6.89	1.16	12.13	13.06	1.08
C12-B1-T1	6.40	4.29	0.67	12.58	10.30	0.82
C12-B2-T1	6.16	4.53	0.74	12.36	10.60	0.86
C12-B3-T1	4.44	5.66	1.28	15.68	17.68	1.13
C12-B4-T1	4.17	5.43	1.30	15.19	17.32	1.14
C12-B5-T1	4.39	5.35	1.22	15.59	17.20	1.10
Present Study						
S-SP2-2	5.28	5.37	1.02	17.11	17.23	1.01
S-SP3-1	3.30	5.50	1.66	13.53	17.43	1.29
S-SP6-1	5.19	5.54	1.07	16.96	17.49	1.03
S-SP13-1	2.10	2.01	0.96	17.44	17.09	0.98

Table A1 (continued). Database of Experimental and Predicted Results

Specimen	$G_{f,exp}$ (lb/in)	$G_{f,pred}$ (lb/in)	$\frac{G_{f,pred}}{G_{f,exp}}$	$P_{u,exp}$ (kip)	$P_{u,pred}$ (kip)	$\frac{P_{u,pred}}{P_{u,exp}}$
Present Study						
S-SP13-2	1.91	1.96	1.02	16.65	16.86	1.01
N-SP3-1	2.00	2.17	1.08	17.00	17.73	1.04
N-SP3-2	1.52	2.13	1.40	14.85	17.57	1.18
N-SP6-1	2.07	2.05	0.99	17.30	17.24	1.00
N-SP6-2	2.20	2.09	0.95	17.87	17.41	0.97
N-SP13-2	14.37	20.79	1.45	7.96	8.83	1.11
Xu et al. (2020)						
CL1-1	17.92	20.79	1.16	8.89	8.83	0.99
CL1-2	25.44	20.79	0.82	10.59	8.83	0.83
CL1-3	14.18	20.79	1.47	7.90	8.83	1.12
CL2-1	17.65	20.79	1.18	8.82	8.83	1.00
CL2-2	21.90	20.79	0.95	9.82	8.83	0.90
CL2-3	22.59	20.79	0.92	9.98	8.83	0.88
CL3-1	19.37	20.79	1.07	9.24	8.83	0.96
CL3-2	18.57	20.79	1.12	9.04	8.83	0.98
CL3-3	21.49	20.79	0.97	9.73	8.83	0.91
CL4-1	21.69	20.79	0.96	9.78	8.83	0.90
CL4-2	26.43	20.79	0.79	10.79	8.83	0.82
CL4-3	24.20	20.79	0.86	10.33	8.83	0.85
CL5-1	20.95	20.79	0.99	9.61	8.83	0.92
CL5-2	24.94	20.79	0.83	10.48	8.83	0.84
CL5-3	4.26	5.17	1.21	15.37	16.90	1.10
Present Study						
S-CL1-2	3.63	5.15	1.42	14.18	16.86	1.19
S-CL2-1	5.24	5.35	1.02	17.04	17.20	1.01
S-CL2-2	6.16	5.13	0.83	18.48	16.83	0.91
S-CL3-1	5.06	5.24	1.04	16.74	17.02	1.02
S-CL3-2	4.52	5.10	1.13	15.82	16.78	1.06
S-CL4-1	1.58	5.29	3.35	9.35	17.10	1.83
S-CL4-2	3.67	5.24	1.43	14.25	17.02	1.19
N-CL1-1	0.89	1.93	2.17	11.36	16.74	1.47
N-CL1-2	2.12	1.96	0.92	17.54	16.86	0.96
N-CL2-1	1.50	2.01	1.34	14.72	17.07	1.16
N-CL2-2	0.80	2.01	2.51	10.75	17.06	1.59
N-CL3-1	1.73	1.90	1.10	15.82	16.59	1.05
N-CL3-2	1.43	1.79	1.25	14.39	16.12	1.12
N-CL4-1	1.67	1.96	1.17	15.55	16.87	1.08
N-CL4-2	1.01	1.97	1.95	12.11	16.92	1.40

Table A2. Results of Laboratory-Aged Smooth Specimens Fabricated with a Normal Modulus Carbon Fiber Reinforced Polymer System

Specimen	P_u (kip)	Average (kip)	Coefficient of Variation	Failure Mode	
				Side A	Side B
S-0-1	18.2	18.8	4.50%	C/D	C/D
S-0-2	19.4			C/D	C
S-A-4-1	20.6	18.7	14.40%	D	C/D
S-A-4-2	16.8			C/D	C/D
S-A-8-1	20.9	20.2	4.70%	C/D	C/D
S-A-8-2	19.6			C/D	C/D
S-B-4-1	19.1	18.3	5.90%	C/D	C/D
S-B-4-2	17.6			C/D	D
S-B-8-1	18.9	19.8	6.00%	C/D	D
S-B-8-2	20.7			C	D
S-C-4-1	14.2	13.6	6.80%	C	D
S-C-4-2	12.9			C/D	A
S-C-8-1	17.7	17.4	2.50%	D	C/D
S-C-8-2	17.1			A/D	C/D

Table A3. Results of Laboratory-Aged Smooth Specimens Fabricated with an Ultra-High Modulus Carbon Fiber Reinforced Polymer System

Specimen	P_u (kip)	Average (kip)	Coefficient of Variation	Failure Mode	
				Side A	Side B
N-0-1	20.8	20.2	4.10%	R	C
N-0-2	19.6			R	C
N-A-S1-1-1	20.1	19.8	1.80%	R	C/R
N-A-S1-1-2	19.6			R	R
N-A-S1-2-1	19.5	17.9	12.00%	R	R
N-A-S1-2-2	16.4			C/R	R
N-A-S1-3-1	14.2	15.0	6.70%	C	R
N-A-S1-3-2	15.7			R	R
N-A-S1-4-1	16.1	17.4	10.50%	R	R
N-A-S1-4-2	18.7			R	R
N-A-S1-5-1	17.2	17.6	3.20%	R	R
N-A-S1-5-2	18.0			R	R
N-A-S1-6-1	19.0	19.2	1.70%	R	R
N-A-S1-6-2	19.4			R	R
N-A-S1-7-1	16.8	17.2	3.00%	R	R
N-A-S1-7-2	17.5			R	R
N-A-S1-8-1	17.9	18.4	4.20%	R	R
N-A-S1-8-2	18.9			R	R
N-B-S1-1-1	18.1	18.5	2.50%	R	C/R
N-B-S1-1-2	18.8			R	R
N-B-S1-2-1	19.2	17.1	17.60%	R	R
N-B-S1-2-2	15.0			R	C
N-B-S1-3-1	19.2	19.4	1.70%	C	R
N-B-S1-3-2	19.6			R	R
N-B-S1-4-1	19.1	20.3	8.80%	C/R	R
N-B-S1-4-2	21.6			C	R
N-B-S1-5-1	18.4	20.0	11.20%	R	C
N-B-S1-5-2	21.6			R	R
N-B-S1-6-1	16.9	16.9	0.50%	R	C
N-B-S1-6-2	16.8			R	C
N-B-S1-7-1	18.6	19.3	5.70%	R	C
N-B-S1-7-2	20.1			R	R
N-B-S1-8-1	18.3	18.0	3.00%	R	R
N-B-S1-8-2	17.6			R	C/R
N-C-S1-1-1	16.1	15.9	1.20%	R	R
N-C-S1-1-2	15.8			R	R
N-C-S1-2-1	20.9	21.0	0.60%	R	R
N-C-S1-2-2	21.1			R	R
N-C-S1-3-1	17.0	16.8	2.00%	R	R
N-C-S1-3-2	16.5			R	R
N-C-S1-4-1	18.6	18.2	2.50%	R	R
N-C-S1-4-2	17.9			R	R
N-C-S1-5-1	19.1	18.9	1.60%	R	C
N-C-S1-5-2	18.7			R	C/R
N-C-S1-6-1	18.5	18.0	4.30%	R	R
N-C-S1-6-2	17.4			R	C/R
N-C-S1-7-1	16.4	19.2	20.60%	A/C	R
N-C-S1-7-2	22.0			R	R
N-C-S1-8-1	20.4	21.5	7.30%	R	R
N-C-S1-8-2	22.6			R	R

Table A4. Results of Laboratory-Aged Specimens with Simulated Corrosion Pitting and Fabricated with an Ultra-High Modulus Carbon Fiber Reinforced Polymer System

Specimen	P_u (kip)	Average (kip)	Coefficient of Variation	Failure Mode	
				Side A	Side B
N-0-1	20.8	20.2	2.89%	R	C
N-0-2	19.6			R	C
N-A-S2-1-1	18.8	18.2	3.12%	R	A/C
N-A-S2-1-2	17.6			R	R
N-A-S2-2-1	12.9	14.0	8.01%	C	R
N-A-S2-2-2	15.1			C	R
N-A-S2-3-1	17.8	19.0	6.32%	C	R
N-A-S2-3-2	20.2			R	R
N-A-S2-4-1	18.5	19.4	4.73%	R	R
N-A-S2-4-2	20.3			R	R
N-A-S2-5-1	18.6	17.5	5.94%	R	R
N-A-S2-5-2	16.5			C/R	C
N-A-S2-6-1	16.6	17.3	3.64%	R	R
N-A-S2-6-2	17.9			R	R
N-A-S2-7-1	19.0	18.3	4.04%	R	R
N-A-S2-7-2	17.6			R	R
N-A-S2-8-1	20.0	18.5	7.70%	R	R
N-A-S2-8-2	17.1			R	R
N-B-S2-1-1	19.0	18.2	4.33%	R	R
N-B-S2-1-2	17.4			R	C/R
N-B-S2-2-1	19.3	19.3	0.11%	R	R
N-B-S2-2-1	19.3			R	R
N-B-S2-3-1	18.6	19.1	2.36%	C	R
N-B-S2-3-2	19.5			R	C
N-B-S2-4-1	21.9	19.0	15.00%	R	R
N-B-S2-4-2	16.2			R	R
N-B-S2-5-1	20.2	18.9	6.85%	R	R
N-B-S2-5-2	17.6			R	R
N-B-S2-6-1	17.4	17.5	0.53%	R	R
N-B-S2-6-2	17.6			C	R
N-B-S2-7-1	19.2	19.1	0.20%	R	R
N-B-S2-7-2	19.1			R	R
N-B-S2-8-1	20.7	19.7	4.98%	R	R
N-B-S2-8-2	18.7			R	R
N-C-S2-1-1	18.9	18.9	—	R	R
N-C-S2-1-2	—			—	—
N-C-S2-2-1	18.7	17.7	5.67%	R	R
N-C-S2-2-2	16.7			R	R
N-C-S2-3-1	15.7	15.6	0.58%	C	R
N-C-S2-3-2	15.5			C	C
N-C-S2-4-1	16.6	18.7	10.99%	R	R
N-C-S2-4-2	20.7			R	R
N-C-S2-5-1	21.7	21.3	1.79%	R	R
N-C-S2-5-2	20.9			R	R
N-C-S2-6-1	21.3	17.8	19.78%	R	R
N-C-S2-6-2	14.3			R	C
N-C-S2-7-1	12.3	13.0	4.88%	C	R
N-C-S2-7-2	13.6			C	C/R
N-C-S2-8-1	17.5	18.0	3.16%	R	C
N-C-S2-8-2	18.6			R	C

Table A5. Results of Laboratory Specimens Subjected to Simulated Heavy Deicing Salts

Specimen ID	Load (kip)	ε_{ult} (με)	Failure Mode	
			Face A	Face B
S-S1-SF1-0-1	15.6	—	A	A
S-S1-SF1-0-2	14.7	—	C/D	C/D
S-S1-SF1-4-1	16.2	4450	A/C	A/C
S-S1-SF1-4-2	16.2	4410	A/C	A/C
S-S1-SF1-8-1	15.6	4720	C/A	C
S-S1-SF1-8-2	16.3	4210	A/C	C
N-S1-SF1-0-1	19.8	—	—	—
N-S1-SF1-0-2	18.8	—	—	—
N-S1-SF1-1-1	18.5	3450	R	R
N-S1-SF1-1-2	16.0	3470	R	R
N-S1-SF1-2-1	18.1	4910	R	R
N-S1-SF1-2-2	22.0	5800	R	R
N-S1-SF1-3-1	23.0	5660	R	R
N-S1-SF1-3-2	21.2	4480	R	R
N-S1-SF1-4-1	18.5	4570	R	R
N-S1-SF1-4-2	18.8	4560	R	R
N-S1-SF1-5-1	20.8	5910	R	R
N-S1-SF1-5-2	21.3	5020	R	R
N-S1-SF1-6-1	19.5	4530	R	R
N-S1-SF1-6-2	18.8	4310	R	R
N-S1-SF1-7-1	21.4	4120	R/A/P	R/S
N-S1-SF1-7-2	22.4	4820	R	R
N-S1-SF1-8-1	17.5	3350	R	R/S
N-S1-SF1-8-2	22.2	4110	R	R
N-S2-SF1-0-1	17.2	—	R	R
N-S2-SF1-0-2	17.8	—	R	R
N-S2-SF1-1-1	17.3	—	R	R
N-S2-SF1-1-2	21.7	6250	R	R
N-S2-SF1-2-1	22.5	4560	R	R
N-S2-SF1-2-2	19.6	5800	R	R
N-S2-SF1-3-1	18.2	5750	R	R
N-S2-SF1-3-2	17.3	—	R	R
N-S2-SF1-4-1	15.3	4100	R	R
N-S2-SF1-4-2	16.2	3210	R	R
N-S2-SF1-5-1	17.7	5750	R/A	R
N-S2-SF1-5-2	16.1	4880	R/A	R
N-S2-SF1-6-1	16.9	6360	R	R
N-S2-SF1-6-2	12.9	—	P/A	P/A
N-S2-SF1-7-1	18.7	4060	R/A	R
N-S2-SF1-7-2	16.7	4790	R/A/P	R
N-S2-SF1-8-1	17.1	4450	R	R
N-S2-SF1-8-2	16.3	4420	P/A	R/S

Table A6. Results of Laboratory Specimens Subjected to Simulated Marine-Level Chlorides

Specimen ID	Load (kip)	ε_{ult} (με)	Failure Mode	
			Face A	Face B
S-S1-SF2-0-1	15.6	—	A	A
S-S1-SF2-0-2	14.7	—	C/D	C/D
S-S1-SF2-4-1	16.6	4090	D/C/A [a]	C/D/A
S-S1-SF2-4-2	15.4	5190	A/D	C/D/A [a]
S-S1-SF2-8-1	16.1	4740	A/D	A/D/S
S-S1-SF2-8-2	15.3	6080	D/A	P/D/A
N-S1-SF2-0-1	19.8	—	—	—
N-S1-SF2-0-2	18.8	—	—	—
N-S1-SF2-1-1	18.2	4560	R	R
N-S1-SF2-1-2	17.7	4460	R	R
N-S1-SF2-2-1	20.4	4530	R	A/R
N-S1-SF2-2-2	18.7	3880	R	R
N-S1-SF2-3-1	21.4	4570	R	R
N-S1-SF2-3-2	16.8	5150	R	R
N-S1-SF2-4-1	16.2	6300	R	R
N-S1-SF2-4-2	13.8	4260	P/C/A	R
N-S1-SF2-5-1	20.4	7080	R	R
N-S1-SF2-5-2	17.3	7040	R/P/C	R
N-S1-SF2-6-1	19.5	3690	R	R/A/S
N-S1-SF2-6-2	15.6	4870	P/C/A/R/S	R
N-S1-SF2-7-1	9.4	4340	P	P
N-S1-SF2-7-2	7.2	2770	P	P/A
N-S1-SF2-8-1	—	—	—	—
N-S1-SF2-8-2	8.1	4270	P/A/S	[b]
N-S2-SF2-0-1	17.2	0	R	R
N-S2-SF2-0-2	17.8	0	R	R
N-S2-SF2-1-1	17.8	5230	R/A	R
N-S2-SF2-1-2	17.7	4050	R/A	R
N-S2-SF2-2-1	14.5	4800	P/A	R/A
N-S2-SF2-2-2	16.5	5660	R	A/R
N-S2-SF2-3-1	18.2	10490	R	R
N-S2-SF2-3-2	16.9	6720	R/P/D	P/C
N-S2-SF2-4-1	15.7	3730	R	R
N-S2-SF2-4-2	15.0	3950	R	R
N-S2-SF2-5-1	16.0	4060	R	R
N-S2-SF2-5-2	15.3	4580	R/C/A/P	P/A/D/C/S
N-S2-SF2-6-1	18.8	5970	R	R
N-S2-SF2-6-2	20.2	4970	R	R
N-S2-SF2-7-1	17.8	3360	R	R
N-S2-SF2-7-2	21.3	3920	R	R
N-S2-SF2-8-1	15.6	4520	R	R
N-S2-SF2-8-2	19.2	6430	R	R

[a] Failure on side of joint with longer bond length.
[b] No failure on given face.

Table A7. Results of Laboratory Specimens Subjected to Simulated Rural Deicing Salts

Specimen ID	Load (kip)	ε_{ult} ($\mu\varepsilon$)	Failure Mode	
			Face A	Face B
S-S1-SF3-0-1	15.6	—	A	A
S-S1-SF3-0-2	14.7	—	C/D	C/D
S-S1-SF3-4-1	16.5	4340	D [a]	A/C
S-S1-SF3-4-2	15.8	4260	D	D/C/A/P
S-S1-SF3-8-1	11.9	4320	C/D [a]	[b]
S-S1-SF3-8-2	14.4	4210	[b]	P/D
N-S1-SF3-0-1	19.8	—	—	—
N-S1-SF3-0-2	18.8	—	—	—
N-S1-SF3-1-1	16.6	3400	R	R
N-S1-SF3-1-2	19.2	6890	R	R
N-S1-SF3-2-1	19.3	7420	R	R
N-S1-SF3-2-2	19.0	3360	R	R
N-S1-SF3-3-1	16.1	5010	R	R
N-S1-SF3-3-2	19.6	3640	R	R
N-S1-SF3-4-1	18.5	4090	R	R
N-S1-SF3-4-2	21.0	5640	R	R
N-S1-SF3-5-1	18.3	4500	R	R
N-S1-SF3-5-2	20.9	4830	R	R
N-S1-SF3-6-1	21.3	5020	R	R
N-S1-SF3-6-2	20.3	6510	R	R
N-S1-SF3-7-1	16.8	4960	R	R/S
N-S1-SF3-7-2	17.1	5960	R/P	R/A
N-S1-SF3-8-1	10.4	—	NF	P
N-S1-SF3-8-2	16.7	4740	R	R
N-S2-SF3-0-1	17.2	—	R	R
N-S2-SF3-0-2	17.8	—	R	R
N-S2-SF3-1-1	19.8	4900	R	R
N-S2-SF3-1-2	17.9	3330	R/C	R
N-S2-SF3-2-1	20.0	4760	R	R
N-S2-SF3-2-2	17.6	3880	R	R
N-S2-SF3-3-1	21.3	4290	R	R
N-S2-SF3-3-2	18.5	4980	R	R
N-S2-SF3-4-1	18.9	5430	R	R
N-S2-SF3-4-2	17.3	4470	R	R
N-S2-SF3-5-1	19.1	4750	R	R
N-S2-SF3-5-2	20.0	5130	R	R
N-S2-SF3-6-1	21.4	3990	R	R
N-S2-SF3-6-2	20.8	3930	R	R
N-S2-SF3-7-1	12.5	3080	P/A	P/C/A
N-S2-SF3-7-2	—	—	—	—
N-S2-SF3-8-1	13.1	5560	P/A/S	A/S/P
N-S2-SF3-8-2	15.2	4740	A	P/C/A

[a] Failure on side of joint with longer bond length.
[b] No failure on given face.

Table A8. Results of *In Situ* Aged Specimens Fabricated with a Normal Modulus and an Ultra-High Modulus Carbon Fiber Reinforced Polymer System

Specimen	P_u (kip)	Average (kip)	Coefficient of Variation	Failure Mode	
				Side A	Side B
S-0-1	18.2	18.8	4.48%	C/D	C/D
S-0-2	19.4			C/D	A/C
S-R-3-1	18.1	18.7	4.59%	C/D	C/D
S-R-3-2	19.3			C/D	C/D
S-R-6-1	17.7	18.4	5.53%	C/D	C/D
S-R-6-2	19.1			C/D	D
S-R-9-1	19.1	17.8	10.34%	C	C
S-R-9-2	16.5			D	C/D
S-R-12-1	15.2	17.1	15.42%	D	C/D
S-R-12-2	19.0			C/D	C/D
S-HDS-3-1	18.2	18.3	0.35%	C/D	D
S-HDS-3-2	18.3			D	C/D
S-HDS-6-1	17.5	17.9	3.20%	C/D	C/D
S-HDS-6-2	18.3			—	—
S-HDS-9-1	18.9	19.3	3.21%	C/D	D
S-HDS-9-2	19.7			D	C/D
S-HDS-12-1	18.9	19.3	3.21%	C/D	D
S-HDS-12-2	19.7			D	C/D
S-M-3-1	18.9	16.4	22.03%	C/D	C
S-M-3-2	13.8			A	D
S-M-6-1	15.9	17.2	10.91%	C/D	D
S-M-6-2	18.5			C/D	D
S-M-12-1	19.3	19.8	3.85%	C/D	D
S-M-12-2	20.4			C/D	C/D
N-0-1	20.8	19.9	5.98%	R	C
N-0-2	19.1			R	R
N-R-3-1	15.9	17.6	13.04%	C/R	C/R
N-R-3-2	19.2			C	R
N-R-6-1	16.4	17.5	9.17%	C	R
N-R-6-2	18.6			R	R
N-R-9-1	17.4	17.9	4.17%	R	C/R
N-R-9-2	18.4			R	R
N-R-12-1	16.5	18.2	13.11%	R	C
N-R-12-2	19.9			A	R
N-HDS-3-1	20.4	18.7	12.86%	R	R
N-HDS-3-2	17.0			C/R	C/R
N-HDS-6-1	19.3	19.2	0.66%	R	R
N-HDS-6-2	19.1			R	R
N-HDS-9-1	19.4	17.8	12.48%	R	R
N-HDS-9-2	16.2			R	R
N-HDS-12-1	18.9	17.9	7.70%	R	R
N-HDS-12-2	17.0			R	R
N-M-3-1	20.2	19.3	6.91%	R	R
N-M-3-2	18.4			R	R
N-M-6-1	18.2	19.9	11.98%	R	R
N-M-6-2	21.6			R	R
N-M-9-1	18.9	18.8	0.25%	R	R
N-M-9-2	18.8			R	R
N-M-12-1	21.7	20.2	10.36%	R	R
N-M-12-2	18.8			R	R

Table A9. Results of *In Situ* Aged Specimens with Simulated Corrosion Pitting and Fabricated with an Ultra-High Modulus Carbon Fiber Reinforced Polymer System

Specimen	P_u (kip)	Average (kip)	Coefficient of Variation	Failure Mode	
				Side A	Side B
N-0-1	20.8	19.9	5.98%	R	C
N-0-2	19.1			R	R
N-S2-R-3-1	16.4	14.6	17.63%	C	R
N-S2-R-3-2	12.8			C	R
N-S2-R-6-1	12.9	12.5	4.68%	C	C
N-S2-R-6-2	12.1			C	C
N-S2-R-9-1	16.7	17.1	3.04%	C	C
N-S2-R-9-2	17.5			R	C
N-S2-R-12-1	14.3	16.5	18.78%	C	R
N-S2-R-12-2	18.7			R	R
N-S2-HDS-3-1	20.4	18.7	12.90%	R	C
N-S2-HDS-3-2	17.0			R	R
N-S2-HDS-6-1	19.1	18.9	1.65%	R	R
N-S2-HDS-6-2	18.7			R	R
N-S2-HDS-9-1	20.4	19.3	7.35%	R	R
N-S2-HDS-9-2	18.3			R	R
N-S2-HDS-12-1	22.1	22.1	0.10%	R	R
N-S2-HDS-12-2	22.1			R	R
N-S2-M-3-1	18.6	18.9	2.50%	R	R
N-S2-M-3-2	19.2			R	R
N-S2-M-6-1	16.3	17.5	9.71%	R	R
N-S2-M-6-2	18.7			R	R
N-S2-M-9-1	19.4	19.8	3.06%	R	C
N-S2-M-9-2	20.3			R	R
N-S2-M-12-1	17.9	14.9	28.66%	R	R
N-S2-M-12-2	11.9			C	C